12-15-2014

Applications of Advanced Imaging Methods: Macro-Scale Studies of Woven Composites and Micro-Scale Measurements on Heated IC Packages

Siming Guo
University of South Carolina - Columbia

APPLICATIONS OF ADVANCED IMAGING METHODS: MACRO-SCALE STUDIES OF WOVEN COMPOSITES AND MICRO-SCALE MEASUREMENTS ON HEATED IC PACKAGES

by

Siming Guo

Bachelor of Science
Shanghai JiaoTong University, 2007

Submitted in Partial Fulfillment of the Requirements

For the Degree of Doctor of Philosophy in

Mechanical Engineering

College of Engineering and Computing

University of South Carolina

2014

Accepted by:

Michael Sutton, Major Professor

Kenneth Reifsnider, Committee Member

Xiaodong Li, Committee Member

Lingyu Yu, Committee Member

Ziehl, Paul H., Committee Member

Lacy Ford, Vice Provost and Dean of Graduate Studies

ACKNOWLEDGEMENTS

I would never have been able to finish my dissertation without the guidance of my committee members, help from friends, and support from my family. I would like to express my deepest gratitude to my advisor, Dr. Sutton, for his excellent guidance, caring, patience, and providing me with an excellent atmosphere for doing research. I would like to acknowledge my committee members Dr. Reifsnider, Dr. Li, Dr. Yu, and Dr. Ziehl for guiding my research in the past several years. I also want to appreciate Dr. Deng, Dr. Gresil, Dr. Majumdar, and Mr. Patrick Pollock for their support throughout my research developments and analyses. Many thanks are also given to Dr. Ning Li, Dr. Zhao, Dr. Chen and Dr. Zhu in our research group for their support. I would like to thank Dr. Ghoshory and Dr. Yang in EM center for their support when I used the SEM facilities at USC. Special thanks go to Dr. Webb and his student Mr. Zhong, who allowed me unlimited use of their equipment and were always willing to help and give their best suggestions for E-beam lithography and PVD. The financial support of Dr. David Stargel in the Air Force Office of Scientific Research and Dr. Liwei Wang at Intel are also gratefully acknowledged. My research would not have been possible without their help. The support of Correlation Solutions, Incorporated and especially Dr. Hubert Schreier and Mr. Mica Simonsen through technical interactions regarding the optical measurements is gratefully acknowledged. Finally, I would like to thank my family. They supported and encouraged me throughout my PhD studies, giving me their best wishes for success on innumerable occasions.

ABSTRACT

As a representative advanced imaging technique, the digital image correlation (DIC) method has been well established and widely used for deformation measurements in experimental mechanics. This methodology, both 2D and 3D, provides qualitative and quantitative information regarding the specimen's non-uniform deformation response. Its full-field capabilities and non-contacting approach are especially advantageous when applied to heterogeneous material systems such as fiber-reinforced composites and integrated chip (IC) packages.

To increase understanding of damage evolution in advanced composite material systems, a series of large deflection bending-compression experiments and model predictions have been performed for a woven glass-epoxy composite material system. Stereo digital image correlation has been integrated with a compression-bending mechanical loading system to simultaneously quantify full-field deformations along the length of the specimen. Specifically, the integrated system is employed to experimentally study the highly non-uniform full-field strain fields on both compression and tension surfaces of the heterogeneous specimen undergoing compression-bending loading. Theoretical developments employing both small and large deformation models are performed. Results show (a) that the Euler–Bernoulli beam theory for small deformations is adequate to describe the shape and deformations when the axial and transverse displacement are quite small, (b) that a modified Drucker's equation effectively extends the theoretical predictions to the large deformation region, providing an accurate estimate

for the buckling load, the post-buckling axial load-axial displacement response of the specimen and the axial strain along the beam centerline, even in the presence of observed anticlastic (double) specimen curvature near mid-length for all fiber angles (that is not modeled), (c) for the first time show that the quantities σ_{eff} - ε_{eff} are linearly related on both the compression and tension surfaces of a beam-compression specimen in the range $0 \leq \varepsilon_{eff} < 0.005$ as the specimen undergoes combined bending-compression loading. In addition, computational studies also show the consistency with the experimental σ_{eff} - ε_{eff} results on both surfaces.

In a separate set of studies, SEM-based imaging at high magnification is used with 2D-DIC to measure thermal deformations at the nano-scale on cross-sections of IC package to improve understanding of the highly heterogeneous nature of the deformations in IC chips. Full-field thermal deformation experiments on different materials within an IC chip cross-section have been successfully obtained for areas from 50x50 μm^2 to 10x10 μm^2 and at temperatures from RT to $\approx 200^oC$ using images obtained with a Zeiss Ultraplus Thermal Field Emission SEM. Initially, polishing methods for heterogeneous electronic packages containing silicon, Cu bump, WPR layer, substrate and FLI (First level interconnect) were evaluated with the goal of achieving sub-micron surface flatness. Studies have shown that surface flatness of 700nm is achievable, though this level is unacceptable when using e-beam photolithography for nanoscale patterning. Fortunately, a novel self-assembly technique was identified and used to obtain a dense, randomly isotropic, high contrast pattern over the surface of the entire heterogeneous region on an IC package for SEM imaging and DIC. Experiments performed on baseline materials for temperatures in the range 25°C to 200°C demonstrates that the complete

process is effective for quantifying the thermal coefficient of expansion for nickel, aluminum and brass. The experiments on IC cross-sections were performed when viewing 25μm x 25μm areas and correcting image distortions using software developed at USC. The results clearly show the heterogeneous nature of the specimen surface and non-uniform strain field across the complex material constituents for temperatures ranging from RT to 200°C. Experimental results confirm that the method is capable of measuring local thermal expansion in selected regions, improving our understanding of these heterogeneous material systems under controlled thermal-environmental conditions.

TABLE OF CONTENTS

LIST OF TABLES

LIST OF FIGURES

CHAPTER 1

Damage Evolution Studies for Large Deformation of Woven Composite Specimen under Combined Bending-Compression Loading

1.1 Introduction

Fiber-reinforced composite materials have been used over the past few decades in a variety of structures, and are increasingly being used in woven form in a variety of industrial applications, such as aerospace and automotive systems. The growth of applications employing woven composite materials is due to desirable characteristics, such as high ratio of stiffness and strength to weight, long fatigue life, electromechanical corrosion resistance and magnetic transparency. Although woven composite materials have many advantages, they oftentimes exhibit strong anisotropic mechanical behavior due to their fiber orientations, inducing non-uniformity in the strain distribution and activation of a variety of local damage mechanisms. Understanding the relationship between fiber orientation, progressive damage and the corresponding deformation fields is essential when employing such materials in safety critical applications. This is especially true for situations where woven composites exhibit highly nonlinear behavior under certain loading modes, especially large amplitude deformation. In such cases, the evolution of damage and the relationship of damage to the macroscopic strain field are of interest, requiring that full-field deformations be quantified so that the presence of non-uniformity in the strain distribution can be identified and used to develop appropriate failure criteria.

Unfortunately, a large number of practical problems that employ composite structures require nonlinear formulations to describe their response (e.g., post-buckling behavior, load carrying capacity of structures, deformation response). There are two common sources of nonlinearity: geometric nonlinearity and material nonlinearity. Geometric nonlinearity arises purely from geometric considerations (e.g. nonlinear strain-displacement relations), whereas the material nonlinearity is due to nonlinear constitutive behavior of the material system. A third type of nonlinearity may arise due to changing initial conditions or boundary conditions.

Given the complexity of advance composite material systems, there have been a number of experimental and theoretical studies of composite materials to describe the nonlinear stress-strain relationship. Hahn and Tsai [1] employed a complementary elastic energy density function which contained a biquadratic term for in-plane shear stress. The nonlinear stress–strain relation in simple longitudinal and transverse extensions under off-axis loading was predicted. Assuming that fibers are linearly elastic, Sun [2] modeled the composite by employing nonlinear matrix layers alternating with effective linearly elastic fibrous layers. A number of plasticity models also have been used to describe the non-linear behavior of fiber-reinforced composite materials. Some researchers have used micromechanics approaches to establish stress/strain relationships [3-4], while others have studied non-linearity at the structural level [5-12]. Among the structural approaches, the work by Sun and Chen [7, 11] is particularly impressive because of the simplicity and accuracy of their model. They developed a one-parameter plasticity model to describe the nonlinear behavior of unidirectional composites [11, 12], based on a quadratic plastic potential and the assumption that there is no plastic deformation in the fiber direction,

and then generalized it for laminates [13, 14]. Then, Tamuzes extended the study to describe the response of a symmetrical cross-ply composites with nonlinearity in on-axis loading caused by intralaminar matrix cracking [15] and orthotropic woven glass-epoxy composite laminates reinforced by satin woven glass fiber cloth and having different tensile properties in the 0◦ and 90◦ directions [16]. Varizi et al. [17] also suggested a plasticity model for bidirectional composite laminates. However, it requires knowledge of the axial and shear yield strengths, which can be difficult to define and to obtain experimentally for composite materials. Odegard et al. [18] suggested a very simple plasticity model only for woven graphite/PMR-15 composite. Recently, Reifsnider and his group [19-21] developed a theoretical framework resulting in a single equation for predicting the nonlinear behavior of thin woven composites. Pollock et al [22] then used the theoretical construct and demonstrated that it was effective in predicting the response of a thin woven composite specimen subjected to tensile loading.

Though compression and tension experiments have been used in the study of composite material systems, bending and/or bending-compression experiments have been investigated by only a few authors. Wisnom [23, 24] reported that very high strains of about 2.5% were measured on the compression surface with no significant damage on unidirectional carbon-fiber/epoxy, with a consequence of non-linear stress-strain behavior in the fiber direction. Whitney [25] showed that engineering bending theory can give rise to errors if there is any non-linearity in the stress-strain response of the material, or if large displacements occur. Yang [26] reported results from a series of bending experiments and indicated that the through-the-thickness stitching increased the delamination resistance and lowered the bending strength of the composites. Paepegem

[27] showed that composite bending tests yield important additional information that cannot be recovered from the conventional tension tests, noting that uniaxial tension experiments mainly focuses on in-plane characteristics, while laminate composites are actually more sensitive to out-of-plane loading in real applications and are oftentimes weaker in the through-the-thickness direction than in the plane of lamination. Thus, results from bending-compression experiments provide quantitative information regarding both tension and compression effects on damage in composites. Furthermore, such experiments offer investigators the ability to subject thin specimens to large, out-of-plane displacements so that the failure process caused by large local deformation can be investigated.

Although most bending experiments on woven composites have used strain gages to monitor local strain as a function of end load [28, 29], the size of the strain gauge has several disadvantages; (a) only a few gauges can be placed on the specimen, (b) it is not always easy to determine the right position since the highest strain is not necessarily at the center of the woven composite strip because large shear deformations may cause asymmetry [30], (c) with only a few points available for assessing local strain gradients it is difficult to quantify how strains vary across the width and along the length of a specimen and (d) for bending studies with large displacement gradients or high curvature in deformations, strain gages oftentimes will de-bond from the surface. For example, while previous work shows increasing compressive strain with increasing strain gradient [30], the ability to quantify this observation using point-data is uncertain. Because of these issues, there is a paucity of systematic investigations of the nonlinear stress–strain behavior in woven glass/epoxy laminates under bending compression load, resulting in

relatively little experimental data regarding the response of woven glass/epoxy composites undergoing bending load for comparison to the predictions of various analytical models.

An approach that overcomes the difficulties noted above for compression-bending studies of composite (or metallic) specimens is stereo digital image correlation, a relatively well established methodology in modern experimental studies [31-39]. Digital image correlation (DIC), both 2D and 3D, provide both qualitative and quantitative information regarding the heterogeneity of the specimen's deformation response. Its full-field capabilities and non-contacting approach are especially advantageous when applied to heterogeneous material systems such as fiber-reinforced composites, where the effects of fiber orientation and local damage are clearly evident in the measured response. Specifically, 2D DIC has been shown to be effective in both tension and in-plane shear experiments for fiber reinforced composites [40, 41]. In our bending-compression test, 3D DIC was used to monitor the large out-of-plane displacement fields and the full-field surface strain distributions on both the tension and compression surfaces since it has been shown that 2D DIC measurements will be ineffective in the presence of large out of plane motion [42].

With regard to simulation studies, relevant previous work includes the numerical model for layered composite structures based on a geometrical nonlinear shell theory developed by Guttmann, et al, [43]. Of particular note is the work of Lomov et al [44] where the authors used digital image correlation to quantify surface deformations in woven composites as part of a broader effort to develop validated software capable of identifying both the meso-scale (fiber bundle scale) as well as the macroscale response

of the woven composite system. All experiments were tensile loading with relatively small strains (<2%). The orthogonal weave was oriented either along load direction or at 45^{o} to the loading axis, with good agreement demonstrated between FE simulations and experimental evidence for the tensile loading application. In thin-walled open-sections beams made of fiber-reinforced laminates, at which the bending and torsion are coupled, a nonlinear finite element analysis based on the updated Lagrangian formulation was developed by Omidvar and Ghorbanpoor [45] to solve the problem numerically. Krawczyk, et al [46] developed a layer-wise beam model for geometric nonlinear finite element analysis of laminated beams with partial layer interaction. The model was built assuming first order shear deformation theory at the layer level and moderate interlayer slips [46]. Jun, et.al [47] developed the exact dynamic stiffness matrix for a uniform laminated composite beam based on trigonometric shear deformation theory. Reddy [48] deduced a nonlinear formulation of straight isotropic beam using Euler Bernoulli beam theory and Timoshenko beam theory to formulate the kinematic behavior of the beam. The principle of virtual displacement was used to formulate the equilibrium equations.

Most stability studies for composite laminated plates have focused on geometrically nonlinear analysis while research on the effect of nonlinear effective constitutive material properties on composite behavior has been very limited. For example, previous studies indicate that nonlinearity in the in-plane shear is significant for composite materials [49]. Regarding non-linear composite constitutive properties, a few attempts have been made to study buckling of thin composite laminate panels and post-buckling of thick section composite laminate plate. Hu [50] investigated the influence of in-plane shear nonlinearity on buckling and post-buckling responses on composite plates under uniaxial

compression and bi-axial compression and of shells under compression. The effect of material nonlinearity on buckling and post-buckling of fiber composite laminate plates and shells subjected to general mechanical loading, together with the interaction between the material and geometric nonlinearity also was investigated by Hu et al [50]. It was concluded that composite material nonlinearity has a significant effect on geometric nonlinearity, structural buckling load, post-buckling structural stiffness, and structural failure mode shape of composite laminate plates and shells.

Since studies employing combined bending-compressive loading conditions have been very limited in the literature, one objective of the current work is to develop a controlled compression-out-of-plane bending experimentation and full-field deformation measurement method and apply the approach using small plate specimens undergoing large axial displacements and out-of-plane deformation. The results from bending-compression experiments have been shown to provide additional quantitative information regarding both tension and compression effects on the behavior of thin woven composites. Details regarding the experimental system and the woven composite specimens used in this study are presented, along with a discussion of the key aspects in the system in Section II. Section III presents the experimental results and an extended discussion of the results. Meanwhile, since both small and large elastic deflection conditions are of interest, corresponding to classical beam theory and a slightly modified formulation based on Drucker's [51] large deflection theory (which accounts for the shortening of the moment arm as the loaded end of the beam deflects), respectively, modeling results are reported for both cases. The non-linear equations obtained from Drucker's modified formulation are solved using elliptical integrals to evaluate the relationship between the end

compression load and specimen deformation. The predicted response using this model is compared to experimental data obtained in Section IV. Finally, the author extend the concepts proposed by Reifsnider and his collaborators [19-21] to describe the behavior of thin composite materials subjected to other loading conditions (e.g., compression and/or bending). In Section V, using results from the various models, effective stress and effective strain have been introduced to determine whether they are appropriate parameters for correlation of woven composite specimen response at all fiber angles. Section VI provides concluding remarks.

1.2 Specimen and Experimental Consideration

1.2.1 Composite Specimens and Preliminary Studies

The present work employs Norplex Mylar NP 130[1], a composite material composed of an orthogonal 0/90° plane weave glass fabric embedded in a halogenated epoxy resin. As shown in Figure 1.1, the glass fibers are configured in six laminas. The weave length

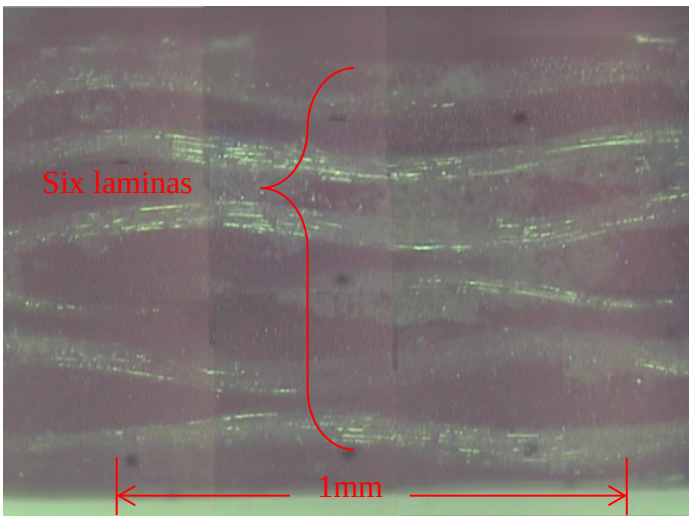

Figure 1.1: Edge view of specimen

[1] Commonly used as a structural material in computer chips.

(from peak to peak) is 1mm, which approaches the total thickness in size. All specimens were extracted from a 600mm by 600mm by 1 mm sheet (see Figure 1.2). Each specimen size was 12.7 mm wide and 101.6 mm long. Specimen orientation was along one of seven different directions, $\theta = 0^o$, 15^o, 30^o, 45^o, 60^o, 75^o and 90^o, which corresponds to fiber angles ($0^o/90^o$), ($15^o/-75^o$), ($30^o/-60^o$), ($45^o/-45^o$), ($60^o/-30^o$), ($75^o/-15^o$) and ($90^o/0^o$), respectively.

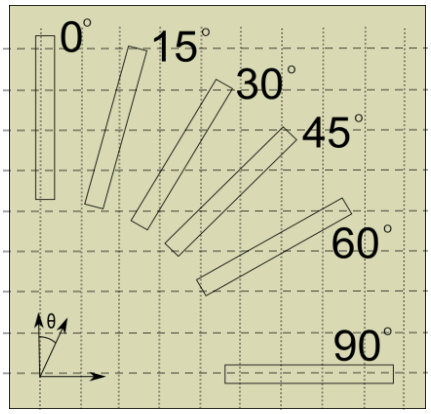

Figure 1.2: Composite plate

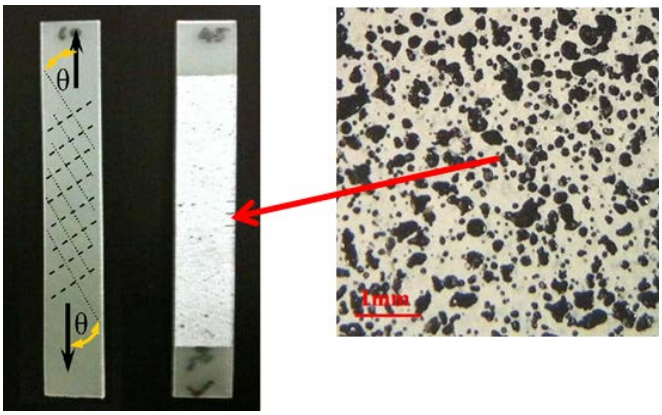

Figure 1.3: Specimen with applied random pattern for 3D digital image correlation.

Figure 1.3 shows a composite specimen and also a patterned specimen surface prepared for digital image correlation. High contrast speckle patterns were applied using a thin coat of white enamel paint and a diffuse overspray of black enamel so that the appropriately patterned specimen surface can be used effectively in 3D-DIC to obtain out-of-plane deformations and surface strains throughout the region of interest.

Preliminary monotonic tensile tests to failure were performed to obtain basic material property data using an MTS 810 50kip hydraulic test frame with hydraulic platen grips. Stereo digital image correlation [52] was used to measure the surface strain during each experiment. For each fiber orientation, the results were averaged from three experiments. The final stress-strain curves are shown in Figure 1.4.

Table 1.1: Longitudinal Young's Modulus, E_θ, determined by linear regression using $\sigma_{xx} - \varepsilon_{xx}$ data for individual specimen

θ (^{o})	0^o	15^o	30^o	45^o	60^o	90^o
E_θ(GPa)	25.9	23.5	16.8	14.6	16.5	23.2

Table 1.2: Primary Elastic Properties for Orthotropic Composite

E_1 (GPa)	E_2 (GPa)	G_{12}(GPa)	ν_{12}	ν_{21}
26.2	23.2	5.1	0.15	0.13

Table 1.1 presents the as-measured elastic moduli for fiber orientations $\theta = 0^o$, 15^o, 30^o, 45^o, 60^o and 90^o. The data in Figure 1.4 is consistent with previous work from Dr. K. Reifsnider's group [19-21].

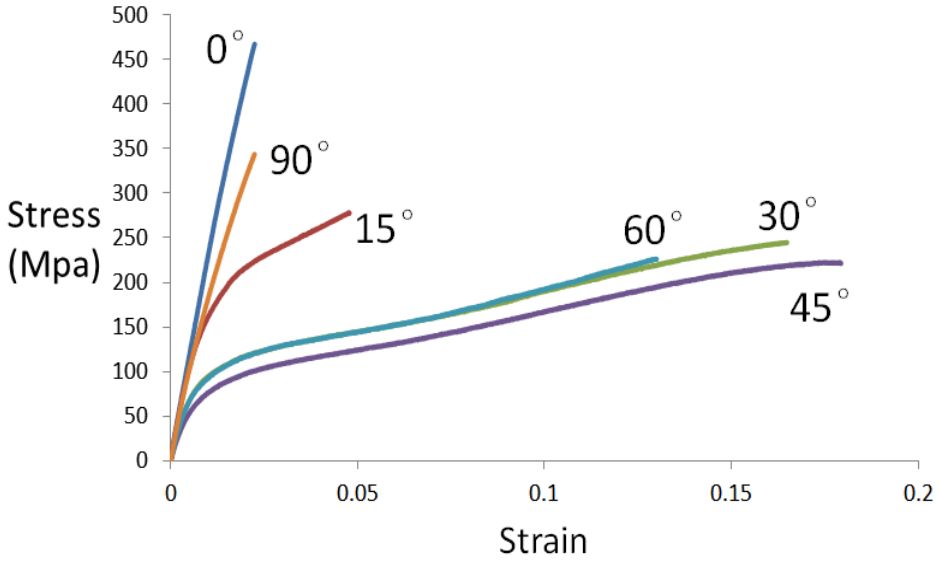

Figure 1.4: The stress–strain curves for specimens cut in six directions.

To determine the orthotropic elastic engineering constants, only the linear parts of the stress-strain relationship are used. Details regarding the optimization procedures used to obtain the composite properties were recently reported in the literature [22]. The

orthotropic composite elastic properties obtained using a non-linear least squares approach are shown in Table 1.2.

1.2.2 Compression-Bending Loading Systems

A schematic of the compression-bending specimen and the loading process is shown in Figure 1.5. All specimens were initially placed in a Tinius Olsen TI-5000 electro-mechanical load frame in a nominally straight configuration. Compressive load, P, axial displacement, Δ, out-of-plane offset from axial centerline, δ, are the primary parameters for our studies.

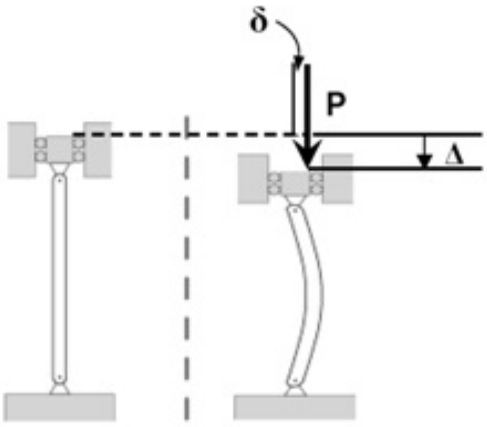

Figure 1.5: Schematic of compression bending specimen, with load, P, offset, δ, and axial displacement Δ.

To perform combined bending-compression loading of specimens such as those shown in Figure 1.3 while simultaneously acquiring stereo images of both sides of the specimen, an integrated experimental set-up was designed that includes the loading fixture, loading machine and two independent stereovision system. Figure 1.6 shows the complete experimental system, including stereovision systems and loading grips.

The Tinius Olsen 5000 (TI-5000) electromechanical test frame (item 6 in Figure 1.6) was modified for use in our studies. The grip speed of TI-5000 is 0.25~500mm/min with different displacement resolution, depending on the required displacement resolution.

Figure 1.6: Integrated compression-bending loading frame with dual stereo-vision systems. 0 and 1: Stereo system viewing compression (tension) surface; 2 and 3: Stereo system viewing tension (compression) surface; 4 and 5; Stiffened stereo-camera holding device; 6: Tinius Olsen 5000 loading frame; 7 Light sources; 8: Stiffened platens connecting TI-5000 to specimen grips; upper-left: Precision load cell; bottom-left: End grips with free out-of-plane rotation and arbitrary load offset.

The accuracy of the displacement sensor is 0.0063mm for grip speeds < 12.5mm/min, which is the range used in our experiments. The maximum force capacity is 22.25kN with resolution 0.67N. This accuracy is unacceptable for our experiments, where the maximum load is typically less than 35N. To overcome this limitation, a high accuracy load cell (Honeywell Model 102, S-shaped design) was integrated into the loading frame. The load range is +/-196N with 0.04N resolution. The load cell is shown as an inset in the top left corner of Figure 1.6.

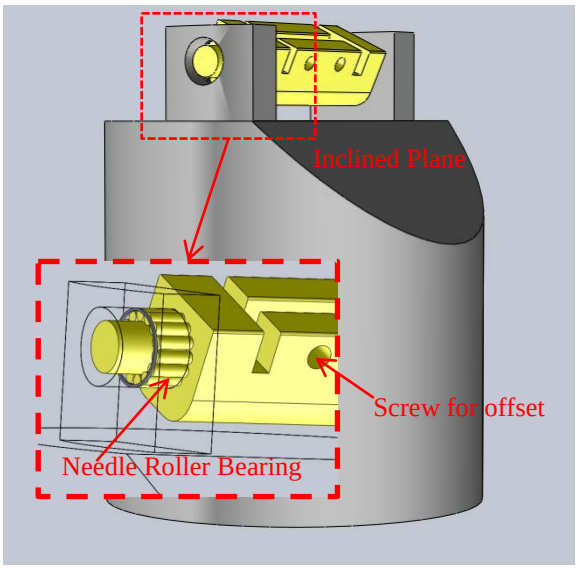

Figure 1.7: Specimen Grip Design

Given the relatively small mechanical loading that will be applied to the specimens during either monotonic loading to failure or during cyclic loading to a pre-specified maximum axial displacement, an end grip was designed to provide well defined end conditions (see Figure 1.7) First, a needle roller bearing was integrated into the grip to allow free out-of-plane rotation of the specimen during bending to simplify analysis of the specimen and ensure the central location along the length corresponds to the maximum moment location (e.g. approximates the critical location) during both monotonic and cyclic loading. Second, the specimen was positioned in the grip using two small screws and various shim thickness to provide an offset that resulted in a small applied bending moment to minimize specimen buckling effects. Third, the grip was machined to include an inclined plane so that the large bending deflections incurred under monotonic loading would not be restricted by the grip shape; out-of-plane end rotations larger than 90º were obtained for some fiber orientations. Finally, the small gripping section of the fixture was manufactured from brass with minimum mass to

reduce the moment of inertia and limit its effect during planned future higher frequency fatigue experiments.

Results from preliminary compression-bending experiments confirmed that the compressive load reaches a relatively constant, low value for $\Delta > 0.25$mm, resulting in instability when performing experiments in load control (which is preferred for use in future modeling studies). To deal with this issue, an external, software-hardware system was developed and interfaced with the TI-5000 for performing low load, large displacement bending/compression experiments. Specifically, the investigators developed the control system so that control can be readily shifted from displacement to load during the experiment, providing a stable platform for experimental studies while also ensuring that load control is possible in those regions (e.g., nominally elastic) where possible.

To perform the loading process in a manner that allows control of (a) axial displacement, Δ, of the specimen and/or (b) axial load, P, of the specimen and (c) acquisition of simultaneous images from all four cameras at a pre-specified combination of Δ and P. the entire TI5000 control system was analyzed, modified to meet our requirements and then controlled using a National Instruments (NI) LabView software (Version 8.2) program. The program was written to automate the mechanical loading and data storage procedures. Figure 1.8 provides a flow chart for the automation process. In this work, NI device BNC adapter 2110 was used for analog input, analog output and trigger/counter functions. The NI data acquisition (DAQ) device PCI-6023E was used for high-performance multifunction analog, digital, and timing I/O. The investigators

manufactured custom-made serial cable (a 9 pin to 25 pin cable for output/input of data from various channels) and used the cable for all communication with the TI-5000.[2]

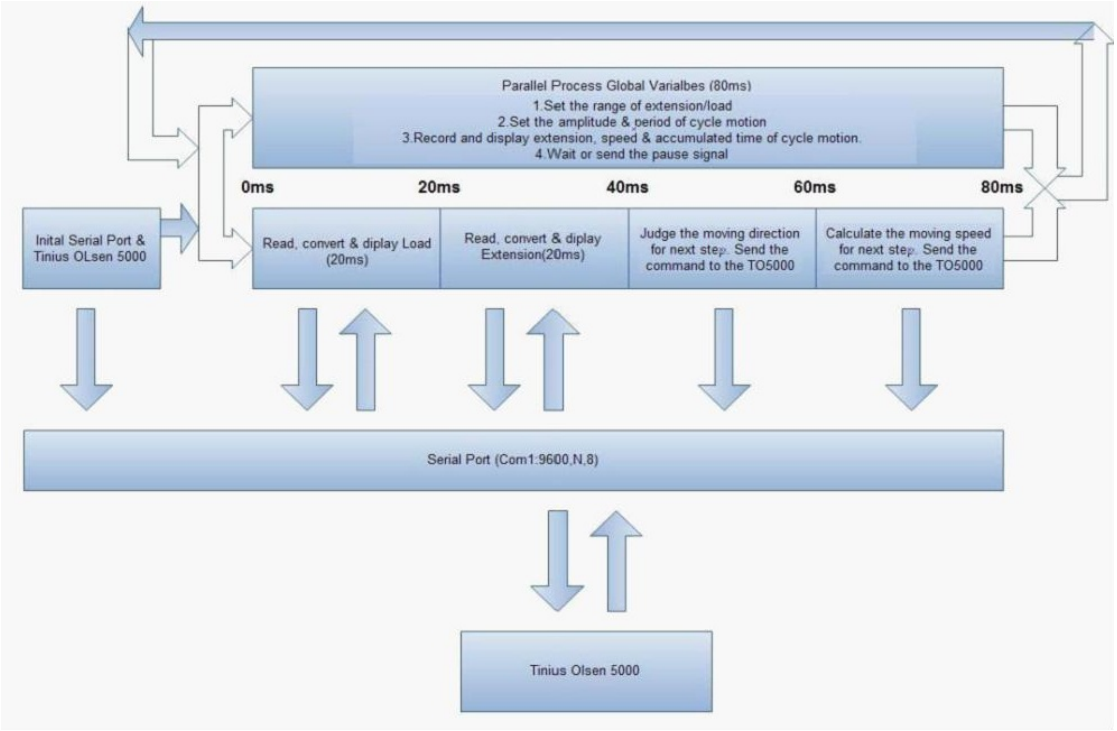

Figure 1.8: Flow chart for Labview program controlling all I/O functions for TI-5000

1.2.3 Four-camera Stereo-vision System

Since the combined compression-bending studies will result in large out-of-plane motion and substantial in-plane strains, a dual stereo-imaging system with 3D Digital Image Correlation (3D-DIC) is employed to accurately and simultaneously measure surface deformations on both surfaces during the loading process. Figure 1.6 shows the two complete stereo vision systems in the configuration used for our studies. Table 1.3 summarizes the specifications for the system.

[2] A Q-basic program was used to evaluate the input/output process. The configuration of the handshake signal was determined to be "COM1:9600,N,8", with a maximum refresh rate for each signal of 20 milliseconds.

Table 1.3: Specifications for Stereovision Systems

Camera Types	Point Grey (compression side)	Q-Imaging (tensile side)
Pixel resolution	2448x2048	1360x1036
Lens focal length	55mm	55mm
Nominal optical F#	22	22
Object resolution (square pixels)	32.3 pixels/mm	18.2 pixels/mm
Distance to specimen	0.4m	0.4m
Synchronization[3]	1μs	1μs

Since the two stereo-vision systems are viewing separate surfaces of the specimen, there are several issues that require discussion including (a) lighting, (b) depth of field and field of view, (c) mounting system and camera positioning (d) specimen patterning for large out-of-plane displacement, (e) calibration, and (f) measurements.

Lighting

First, lighting for each stereovision system is provided by at least two halogen lamps. As shown in Figure 1.6, the halogen lights are located at least 1m from the specimen. To minimize heating of the specimens, a robust IR filter is used for each halogen light[4]. Each set of cameras is mounted firmly to a cross-beam to minimize vibration throughout the experiment.

Depth of field and field of view

Since preliminary experiments indicated that out-of-plane displacements up to 40mm will occur during the bending/compression experiment for the $45^o/45^o$ fiber orientation, the combination of (a) required depth of field (DOF) and (b) the relatively

[3] Synchronization was performed using VICSnap software (2009) and splitter hardware[27]
[4] Modern LED light systems or fiber optic light sources are recommended as a replacement for halogen lights, since the IR filters can overheat and fail during extended operation.

close camera positioning required to obtain high resolution images for strain field determination across the width of the specimen necessitated an analysis of both the depth of field (DOF) and field of view (FOV) prior to performing experiments. Using the procedure outlined in [39], with the tabulated specifications in Table 1.3 and an assumed 10μm spot size, DOF ≈ 24mm. For an object distance of 0.40m, focal length of 0.055m and a CCD sensor size of 0.0127m, the angle of view is ≈ 13.2^{o} and FOV ≈ 90mm by 90mm. Based on this information, and the geometry of the specimen it is clear that (a) approximately one-half of the specimen length can be imaged by both stereo-vision systems and (b) there may be slight blurring of the specimen at maximum displacement in the central region where displacements are largest during bending.

Camera Positioning and Orientation

To optimize the positions of the two stereo-vision systems, a modified version of the procedure outlined by Sutton et al [53] is employed. In the bending-compression experiment, the compression side of specimen moves away from cameras and the tension side moves toward cameras, So the investigators performed a preliminary experiment where (a) the compression side camera system is placed as close to the undeformed specimen as possible while maintaining reasonable focus and (b) the tensile side camera system is placed as far from the undeformed specimen as possible while maintaining adequate focus. Results from a series of out-of-plane translation experiments ranging from 0mm to 40mm confirmed that the images on both sides of the specimen were sufficiently focused throughout the experiment and image correlation was performed successfully, with strain variability consistent with previous, well-focused experiments. As a result, this procedure was used to set up the stereo-vision systems for all

experiments. The as-constructed imaging configuration deviated slightly from previous theoretical estimation, resulting in a FOV of 75mm by 60mm, which extends beyond the specimen mid-span and hence is adequate for our studies.

With regard to the specimen region being viewed, it is noted that the axial displacement, Δ, on one end of the specimen ranges up to 90mm during monotonic compression-bending loading. To eliminate this issue, stereo-imaging on both the compression and tension sides of the specimen was performed on the lower one-half of the specimen where the grip is stationary.

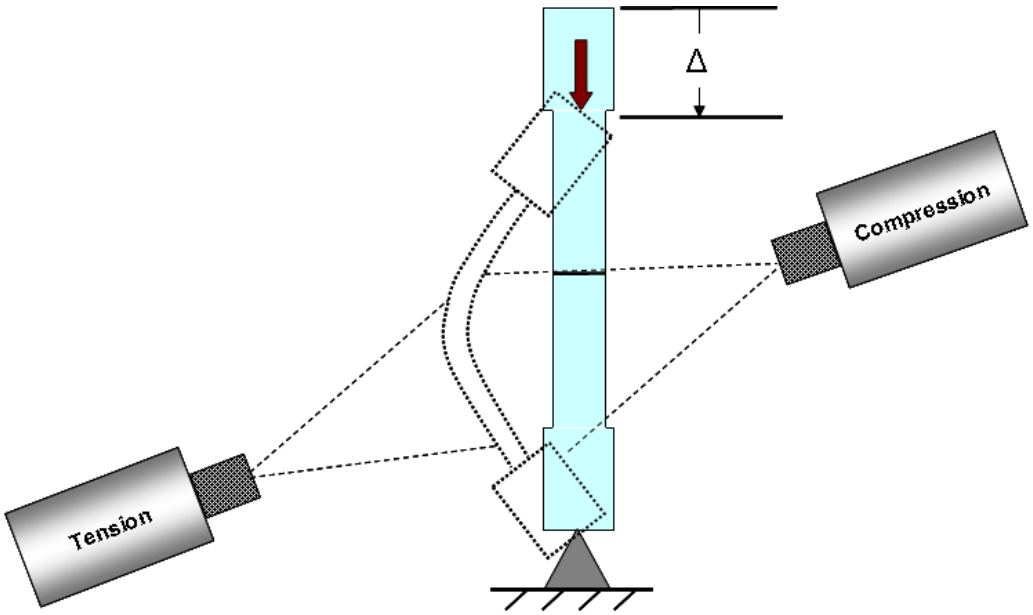

Figure 1.9: Schematic of positioning and orientation of stereovision systems for compression-bending composite specimen experiments. Compression (tension) side vision system rotated counterclockwise by ≈20^{o}, moved closer (further) from specimen and translated vertically upward (downward) by ≈ 20mm.

Finally, preliminary experiments confirmed that the compression-bending process resulted in out-of-plane specimen rotations that approached 90^{o} at the stationary end. To ensure that image correlation could be performed along most of the specimen length, both

stereo-vision systems were initially configured as shown in Figure 1.9. By orienting and positioning the systems as shown, the deleterious effects of subset foreshortening due to rotation were minimized and image correlation could be performed successfully for the entire FOV on the specimen.

Speckle Patterning

Regarding speckle patterning, as noted in a recent publication [39] oversampling requires that each speckle be sampled by at least 3x3 pixels for optimal accuracy. Thus, the minimum speckle sizes would be ≈ 0.2mm on the tension side and ≈ 0.11mm on the compression side. However, due to the presence of large out-of-plane displacements, images of the speckles will decrease (increase) substantially on the compression (tension) sides. In our studies, a slightly larger speckle size was used to ensure oversampling of each speckle throughout the experiment. To apply the speckle pattern, an airbrush with 0.5mm needle is used to spray a relatively homogeneous spot pattern spot. By moving the specimen closer (further) from the nozzle, a larger (smaller) pattern is generated on the compression (tension) surfaces of the specimen. Here, the as-produced average speckle sizes are 0.4mm (0.3mm) on the compression (tension) surfaces. Figure 1.3 shows a typical speckle pattern produced on the compression side of the specimen.

Calibration

Stereo-vision calibration was performed simultaneously for both systems using the procedures described in previous publications [39, Chapter 7.2; 29]. Briefly, a specially-designed planar target is manufactured with through-thickness circular white cylindrical markers embedded in an orthogonal array within a nominally black plate having a constant thickness, t +/- 10μm. After positioning both systems as shown in Figure 1.9,

images of the translated and rotated target are acquired simultaneously by both stereovision systems. Each system is then calibrated using images from separate sides of the target. Finally, the calibrated imaging systems are then converted to a common orthogonal coordinate system by relating "specimen coordinate systems" defined for each stereovision system and the known target thickness. The common orthogonal coordinate system used for all measurements is shown in Figure 1.10.

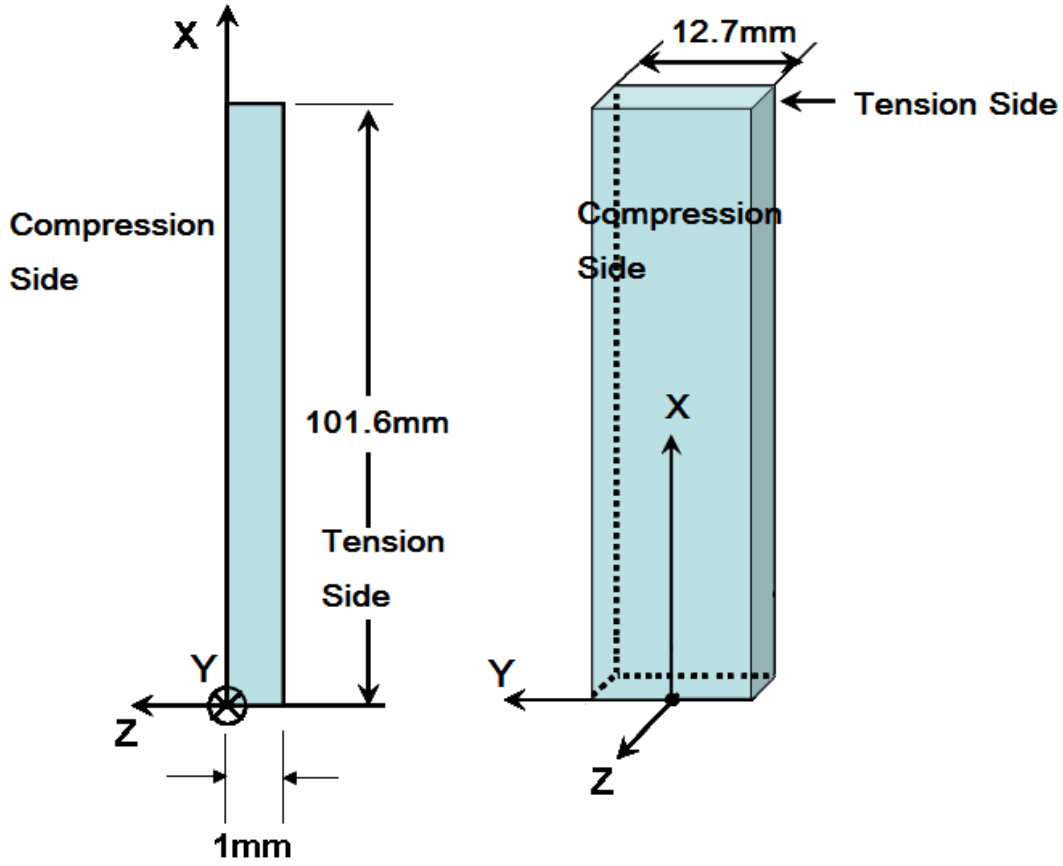

Figure 1.10: Side view and perspective view of composite specimen with common Cartesian coordinate system. The X coordinate is along specimen length; Y coordinate is measured from specimen centerline in the width direction. The Z coordinate is in the thickness direction.

Measurements

During the experiments, stereo imaging was used to obtain the following full-field data at selected loads and axial displacements (a) 3D object displacement components, (u, v, w) in the X, Y and Z directions, respectively, and (b) in-plane strain data ($\varepsilon_{xx,}$ $\varepsilon_{yy,}$ ε_{xy}). Unless otherwise noted, a 31x31 pixel subset size with a subset spacing of 10 pixels is used in all analyses. According to object resolution in Table 1.3, the physical subset size is about 1mm and 1.5mm corresponding to the compression side and tension side, respectively, which is similar to the weave length (see Figure 1.1). Strain data was extracted from the displacement measurements using procedures described previously [39, 52, 53]. Briefly, all displacement components (u, v, w), are converted to a global coordinates system located at the original position in the reference configuration (see Figure 1.10) to obtain 3D displacement fields. Partial derivatives of the displacement field are computed from a quadratic polynomial least square fit to the computed displacement field in a local neighborhood; in this study a 5x5 set of displacement data is used to determine the quadratic best fit for each displacement component. The Lagrangian strain tensor is defined at the center of the polynomial fit in terms of the gradients of the displacement vector components [39]. The preliminary results show that, after calibration, the range of strain values is less than $\pm$200 microstrain.

1.3 Experimental Results

1.3.1 Axial Load and Centerline Moments vs. Axial Displacement

A series of monotonic bending-compression experiments were performed on composite specimens with various fiber orientations. All experiments were performed

with sinusoidal actuation controlled automatically by the Labview program, which keeps the overall average speed constant at 0.21mm/sec (0.5in/min); the maximum displacement rate does not exceed 0.33mm/sec.

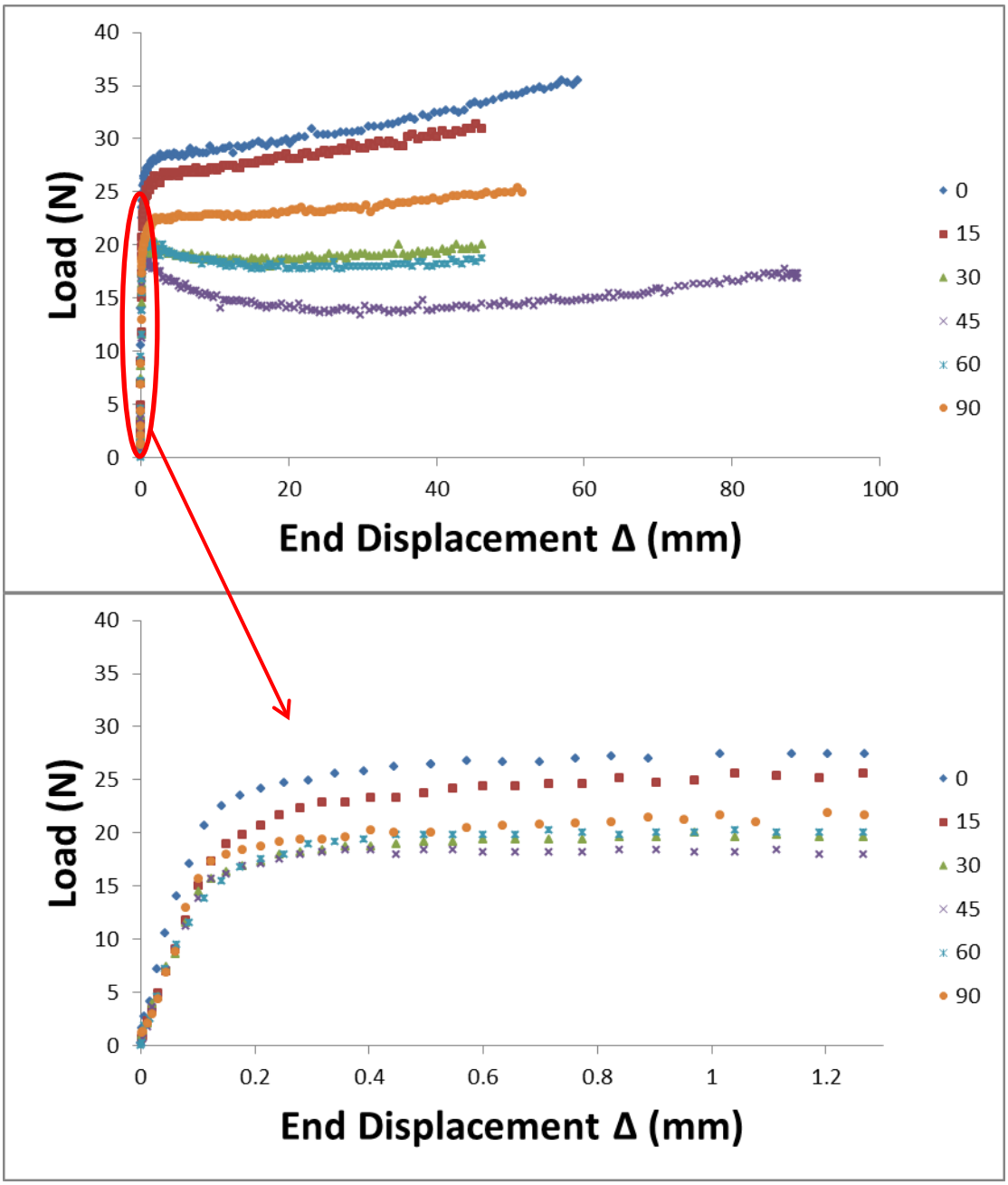

Figure 1.11: Load versus axial displacement; (Top) up to 80 mm; (Bottom) magnified data set for $0 < \Delta < 1.2$mm.

Figure 1.11 presents the measured axial load, P, versus measured axial displacement, Δ, up to final failure for all fiber angles[5]. As shown in the expanded view of the early stages, in the range 0.05mm ≤ Δ ≤ 0.10mm the load reaches a constant value that is a function of fiber angle for axial displacements. For low fiber angles relative to the loading direction, the orthogonal weave specimen has a rising load-displacement behavior up to maximum load. For fiber angles $\geq 30^{o}$, the initial linear region transitions to a falling load regime that eventually leads to a rising load prior to final failure. These results, which include a post-buckling regime, are consistent with predictions using Euler buckling load formulations and the elastic moduli reported in Table 1.1 for various fiber orientations.[6]

Using the measured out-of-plane displacement field, w(x,y,z), which is obtained in a full-field manner by our stereo-vision systems using 3D-DIC at various load levels, the maximum moment in the specimen was determined using the formula Mmax(x=50.8mm, y=0, z = 0.50mm) = P●(δ + ½ (w(50.8mm, 0, 0) + w(50.8mm, 0, 1mm). Figure 1.12 shows the maximum bending moment at mid-length versus the axial compressive displacement, Δ. As shown in Figure 1.12, even for large deformation conditions where the applied axial loading is relatively constant, the measured bending moment is a monotonic function of end-point displacement throughout the loading process for all fiber angles. Furthermore, even though the axial loading is relatively constant for various

[5] For +/- 45^{o} fiber orientation, the specimen did not fracture even when end displacement exceeded 90% of its length, even though significant damage was visually evident (fiber buckling on compression side, massive matrix cracking) at maximum displacement.

[6] In this work, post-buckling refers to the response after elastic buckling of the specimen has occurred. Here, elastic buckling is predicted quite well by classical Euler buckling theory. The concept of post-buckling response for composites is discussed in a recent book [54]

angles, the maximum moment results are ordered in the same manner as both the elastic moduli of the specimens (see Table 1.1) and the P-Δ data shown in Figure 1.10.

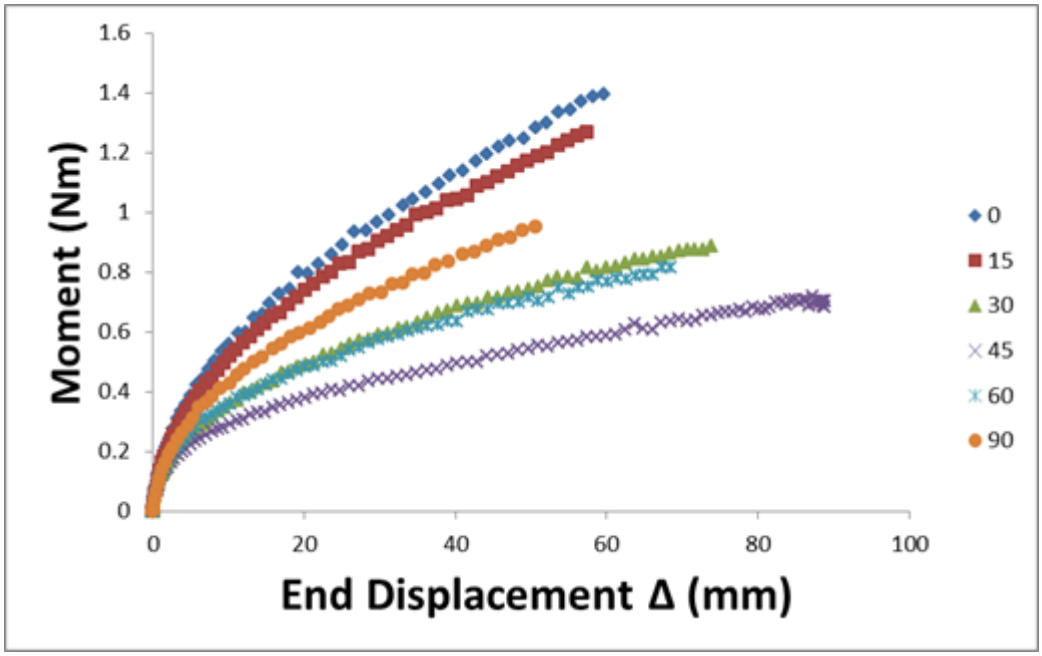

Figure 1.12: Typical local M_{max} Versus Δ data at mid-length of specimen

1.3.2 Surface Strain Measurements

In addition to the global parameter results shown in Figure 1.11 and 1.12, stereo-vision with 3D-DIC provides full-field measurement capability for the surface strains along the length and width of the specimen within the FOV. For the same axial displacement (Δ=40mm), Figure 1.13 shows typical axial strain fields, ε_{xx}, on both the tension and compression surfaces of the specimen for (a) $\theta = 0^o$ and (b) $\theta=45^o$; the black mark on each surface denotes the approximate mid-length location.

As shown in Figure 1.13, for $\theta = 0^o$ strain localization occurs across the entire specimen width for both the tension and compression surfaces near the mid-length (maximum moment) location. At this location, $\varepsilon_{xx}^{max} \approx +0.025$ on the tensile surface and $\varepsilon_{xx}^{min} \approx - 0.03$ on the compression surface. In addition, curvature measurements along the

length clearly show distinctly higher curvature (lower radius of curvature) in the central region where strain localization is most evident.

	Tension Surface (z= -1mm)	Compression Surface (z= 0mm)
$\Theta=0^o$	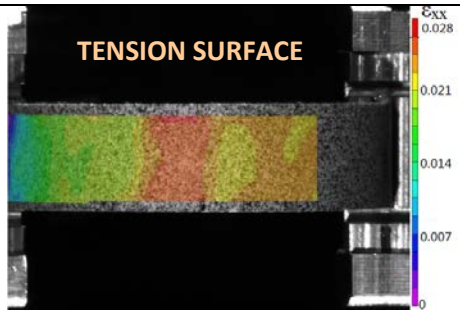	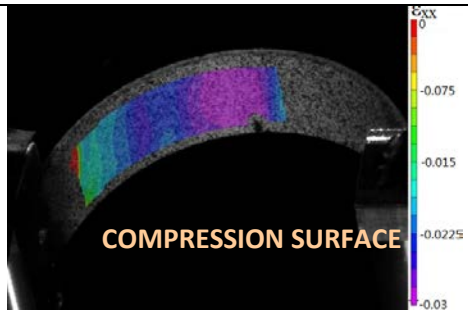
$\Theta=45^o$	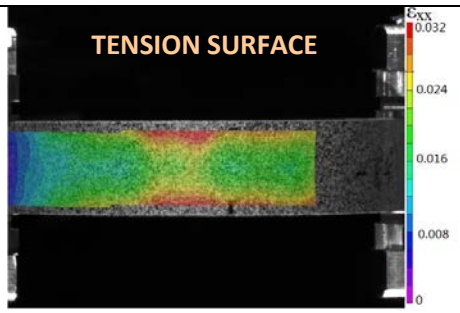	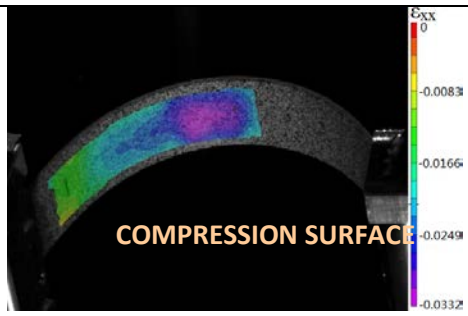

Figure 1.13: Measured axial strain field, ε_{xx}, on tension and compression sides for both $\theta=0^o$ and $\theta=45^o$.

The difference in maximum strains between the tensile and compressive surfaces is physically-relevant and requires additional discussion. For $\theta = 0^o$, the fibers are oriented along the maximum (minimum) strain direction. As indicated in Figure 1.14, for lower fiber angles ($\theta = 0^o$ and $\theta = 30^o$), macroscopic visual evidence clearly shows the presence of local fiber buckling; broken fibers protruding from the specimen surface and complete loss of speckle pattern are clearly visible as the loading proceeds and the curvature increases locally. In fact, micro buckling can be observed by eye on the compressive side of the specimen for all $\theta \neq 45^o$. The onset of visible micro-buckles is a pre-cursor to final failure of each specimen, indicating that the ultimate collapse is primarily due to local

geometric instability and local fiber buckling on the compression surface of the specimen. Conversely, on the tensile side there was no clear evidence of fiber failure, though there was some evidence of matrix micro-cracking.

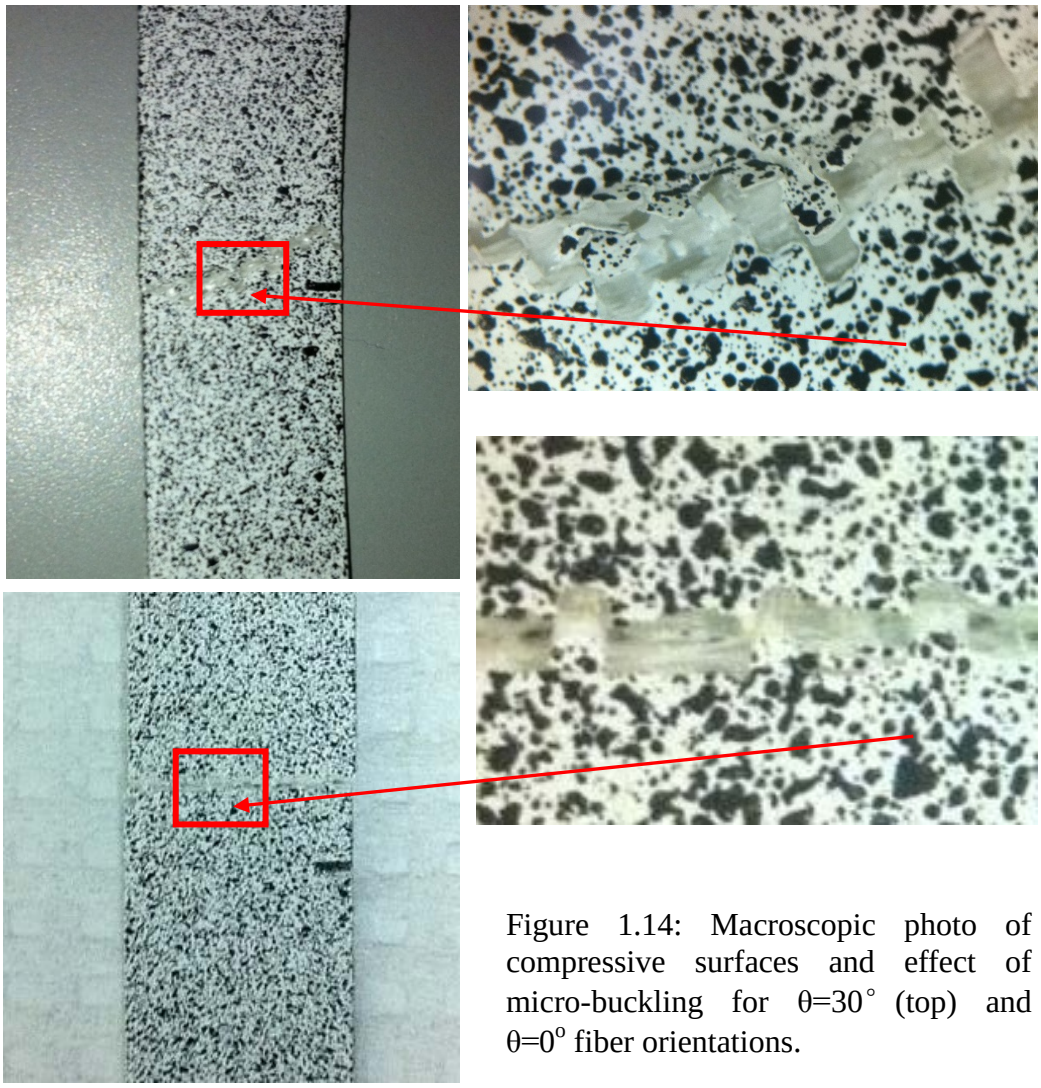

Figure 1.14: Macroscopic photo of compressive surfaces and effect of micro-buckling for $\theta=30^{\circ}$ (top) and $\theta=0^{o}$ fiber orientations.

Thus, the localized region of higher compressive strains is a direct consequence of local damage mechanisms that are well-known to be distinctly different between the tensile and compressive regions in the specimen.

For $\theta = 45^{o}$, again there are distinctly different strain localization fields on the tension and compression surfaces. On the tensile surface, an hour-glass shaped region is

observed where the maximum axial strains occur at the specimen edges. The region is bounded by lines at +/-45^{o}, which correspond to the fiber angles of the orthogonal weave. Thus, the higher axial strains near the unrestrained specimen edges are consistent with matrix deformation in low constraint regions due to the effect of the free edges. Conversely, lower strains in the central portion of the hour-glass region are consistent with increased constraint on the fiber structure imposed by the surrounding orthogonal fiber weave. On the compression side of the specimen, the highly localized strain field shows the reverse trend; significantly higher strains in the central region and lower strains on the edges of the specimen. The increased strains in the central region are consistent with matrix-dominated response for this higher fiber-angle specimen. The lower compressive strains near the specimen edges again appear to be related to “free-edge” effects.

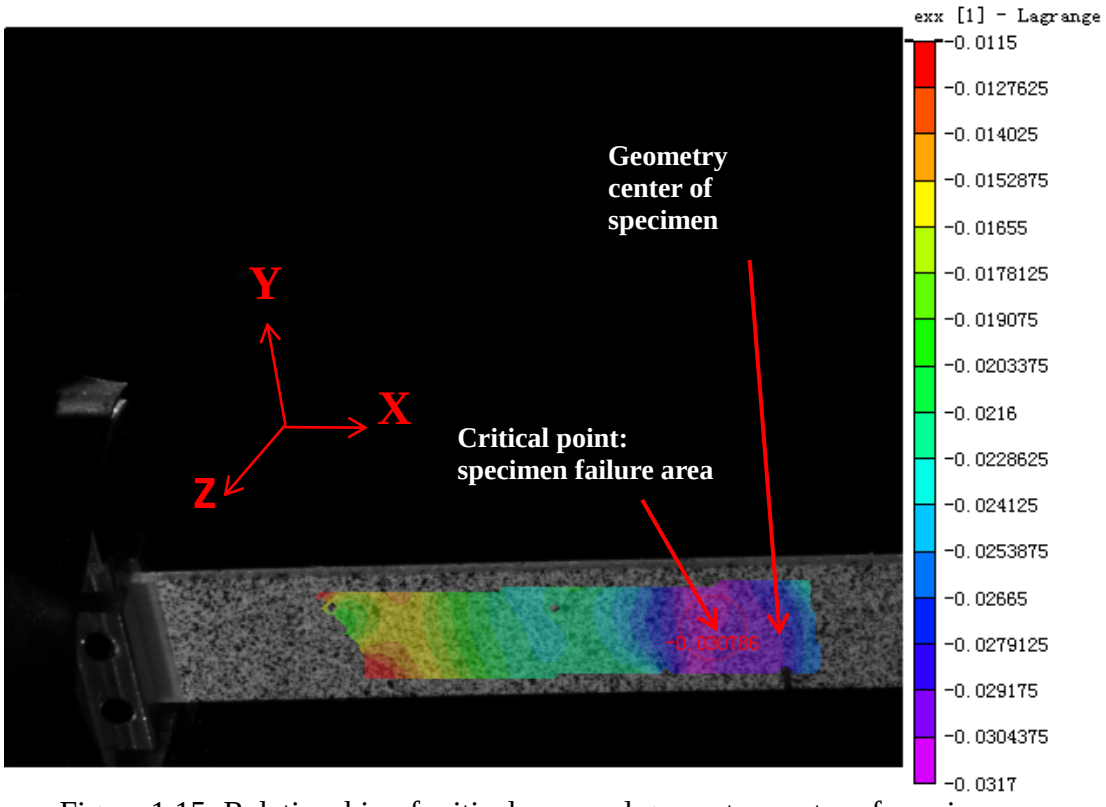

Figure 1.15: Relationship of critical area and geometry center of specimen

Figure 1.15 shows a typical spatial relationship between the beam centerline and the position of the final failure point (which usually has maximum axial strains on both the tension and compression surfaces). Results from our studies indicate that the final failure region occurs within w/2 of the specimen centerline and most often slightly towards the stationary end in Figure 1.9. Since random variations in the fiber distribution/weave during manufacture are inconsistent with this observation, slight asymmetry in the mechanical loading system components (e.g., grips, alignment) is considered to be the most likely source of the preferential shift in failure position.

As one would expect, the evolution of maximum axial strain in the critical region is a function of fiber angle and whether the compression or tensile specimen surface is considered. Figure 1.16 (1.17) show the evolution of ε_{xx} axial strain[7] on the compression (tension) surface of the specimen. Appendix A shows the evolution of both the transverse strain ε_{yy} and the shear strain ε_{xy} on the compression (tension) surface as a function of fiber angle in the same critical region.

[7] For all fiber orientations, each strain component in the critical region is obtained by averaging the strain values within a 5mm diameter region that is centered at the specimen mid-span and mid-width.

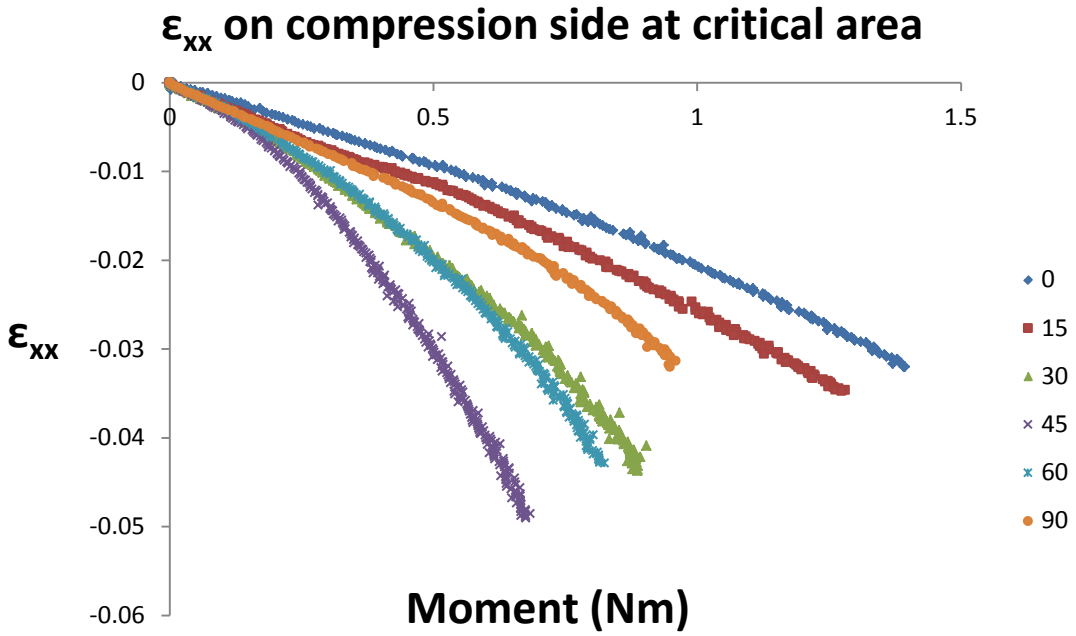

Figure 1.16: Average ε_{xx} strain in critical region on compression surface of specimen versus bending moment

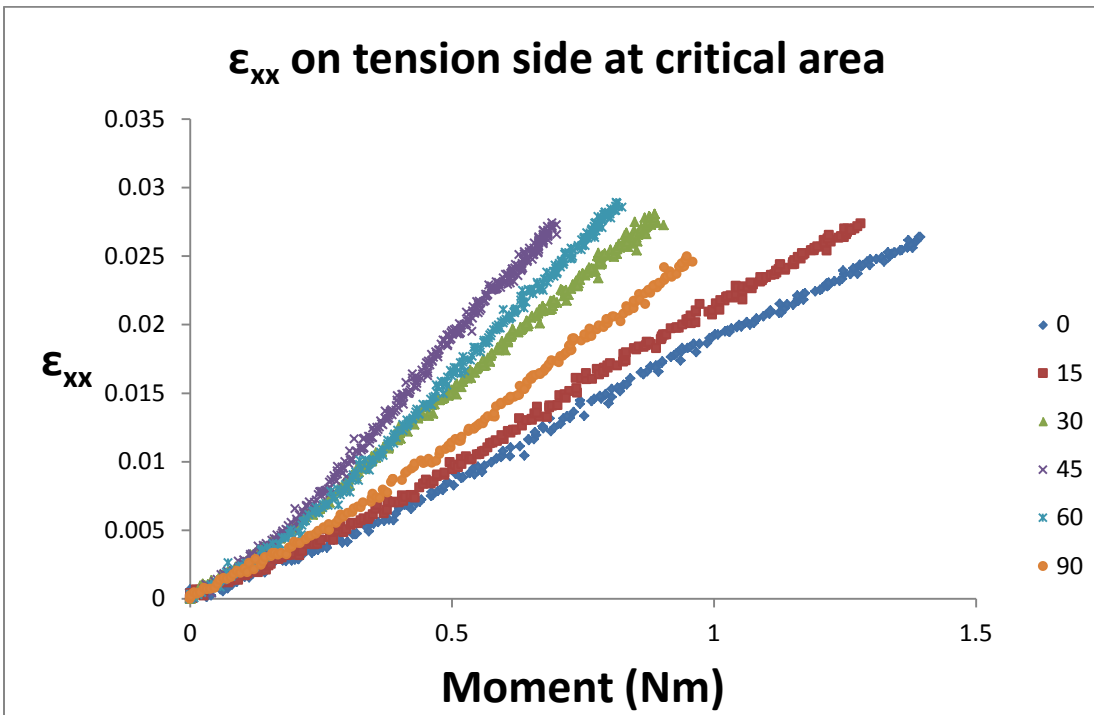

Figure 1.17: Average ε_{xx} strain in critical region on tensile surface of specimen versus bending moment

Comparison of Figures 1.16 and 1.17 indicates that the measured axial strains on the compression side for all fiber angles are much higher than the tension side. Such an observation is nominally consistent with the observed presence of micro-buckling in the critical region for $\theta \neq 45^{o}$ and suggests that the effective bending neutral surface of the damaged specimen has shifted towards the tension surface. Further evidence of a shift in the bending neutral surface is the nature of the bi-linear (changing slope) functional form for the tensile strain data; a shift in slope of the strain-moment data occurs when $\varepsilon_{xx} \geq 0.005$, suggesting that compression-side damage via micro-buckling occurred prior to these strain levels. The observation that the tensile strain field remains linear until reaching maximum axial displacement indicates the damaged fiber-matrix structure on the tension side has relatively constant resistance to the increasing moment. Conversely, the continuing non-linear strain-moment relationship on the compression surface for all fiber angles is consistent with increasing damage and decreasing resistance to the moment in this region up to specimen collapse.

1.3.3 Anticlastic Curvature

For $\Delta < 5$mm, our w(x,y) measurements indicate that nearly the same primary and anticlastic beam curvature are present along the specimen length for all fiber orientation angles; if w(x,y) data for each fiber angle and a specific $\Delta < 5$mm were plotted together, the results are nearly the same. However, for larger Δ, the investigators observed the presence of double curvature near the critical region of the compression-bending specimen, especially for increasing primary curvature (large Δ implies large w(x,y) and hence larger curvature), for all fiber angles.

The largest anticlastic curvature (warping) occurred near mid-length in the $45^o/45^o$ specimen for relatively large Δ. Figure 1.18 shows typical double curvature measurements in a $45^o/45^o$ specimen with $\Delta \approx 40$mm. At the top left of Figure 1.18 is the three-dimensional shape of the left-half[8] of the $45^o/45^o$ specimen. At the bottom left is the out-of-plane displacement data for the center line of specimen. Figure 1.18 indicates that the axial shape of the specimen in the bending-compression experiment approximates a sine curve when the deformation is not too large, which is consistent with the expected shape using Euler–Bernoulli beam theory with the small deformation assumption $1/\rho \approx d^2w/dx^2$. This observation is due to the coupling that exists between the shape of specimen and the bending moment, which is proportional to the second derivative of deflection using small deformation theory. Further analysis in author's next paper shows that, for small deformations, this is quite accurate. For large deformations, the shape of specimen is more arched than a sine curve and a detailed equation description will be given using large deformation theory to show the origin of the differences later.

Also shown in Figure 1.18 is the cross-width shape of the beam on the compression surface in the critical region near the beam centerline. In this case, the difference in out-of-plane deflection between the center and edge of the beam, $\Delta w \approx 0.3$mm, is 30% of the thickness (h=1mm).

[8] Since the specimen is loading in a nominally symmetric manner relative to a Y-Z plane located at the specimen centerline, data is provided for ½ of the specimen length.

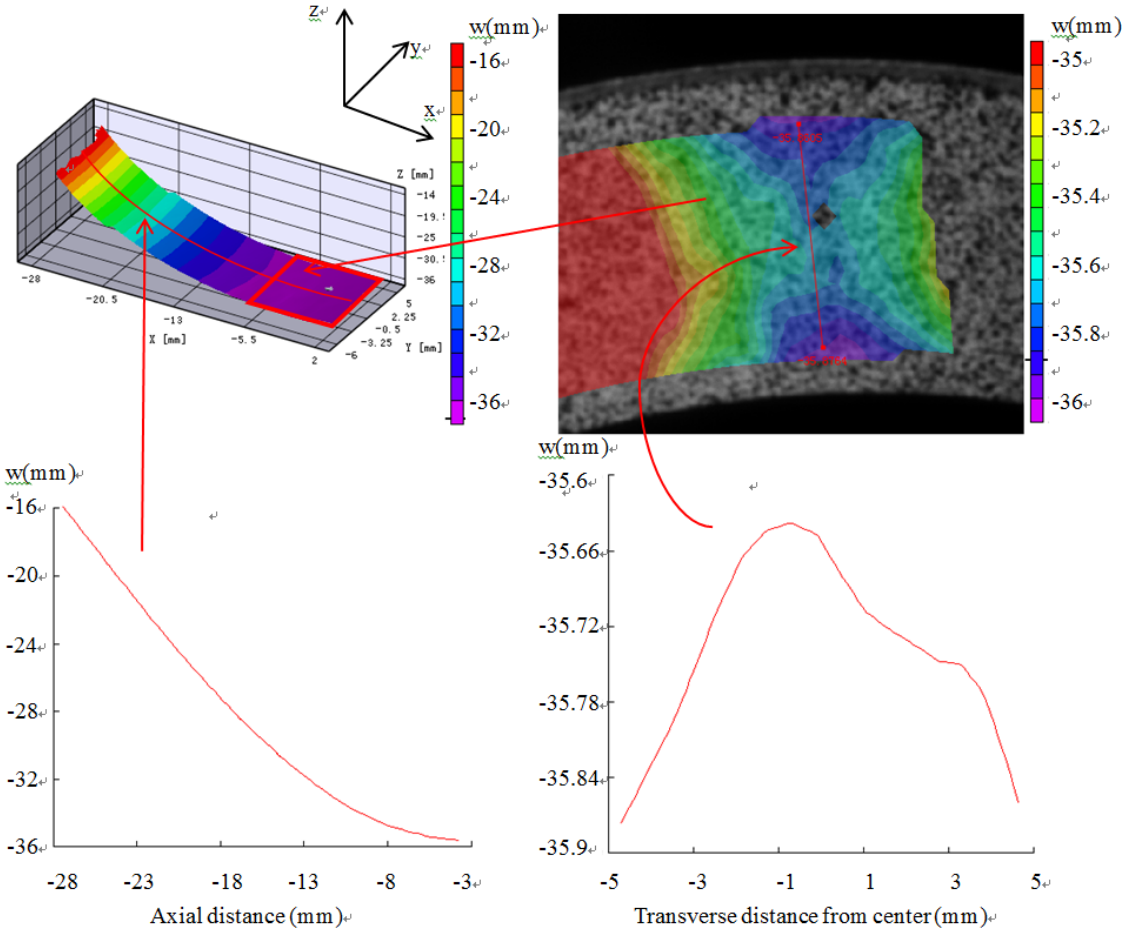

Figure 1.18: Full-field deflection data of 45-45 specimen

Figure 1.19 shows the normalized deflection ratio $\Delta w/h$, for $0^o/90^o$, $15^o/75^o$, $30^o/60^o$ and $-45^o/+45^o$ specimens in the critical region near the specimen centerline for. Inspection of Figure 1.19 shows that (a) for fiber angles from $30^o \rightarrow 60^o$, the effect of anticlastic curvature appears to be significant in the critical region for relatively large values of Δ near final collapse and (b) for lower fiber angles, the measured $\Delta w/h<0.1$ which suggests that, if a simpler analysis methodology is employed, the effect is small and the deformations obtained by considering the response of an orthotropic material with two different Young's moduli may be sufficient.

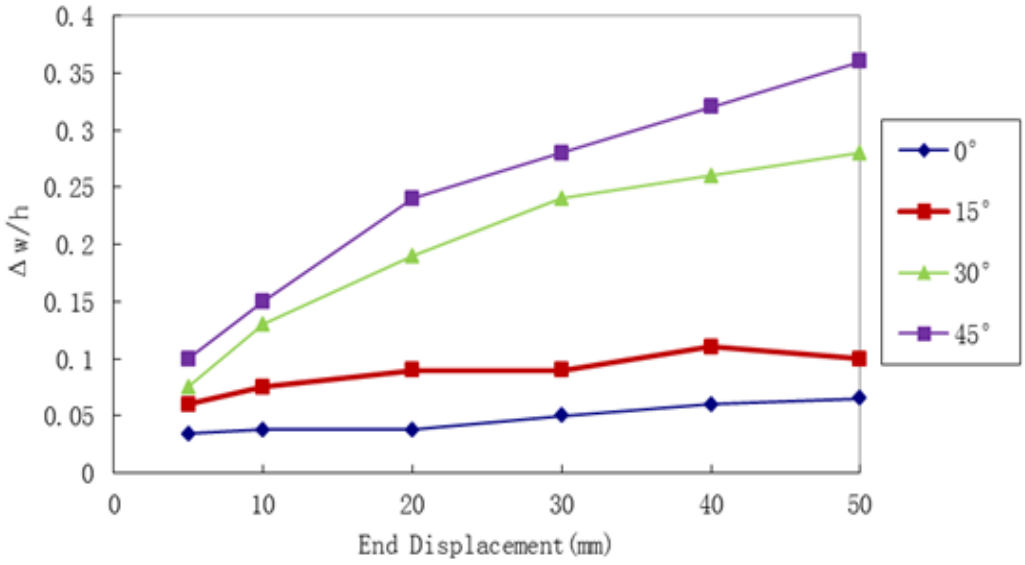

Figure 1.19: Normalized deflection difference along transverse direction.

Figures 1.20 and 1.21 show the measured transverse strain, ε_{yy}, and the axial strain, ε_{xx}, on the tension side at mid-span, respectively. Inspection of Figures 1.19 and 1.20 indicates that when the anticlastic curvature appears to be significant in $30^o/60^o$ and $-45^o/+45^o$ specimens, the transverse strain is also much larger. However, as shown in Figure 1.21, the axial strain at mid-span is only slightly different for all fiber angles.

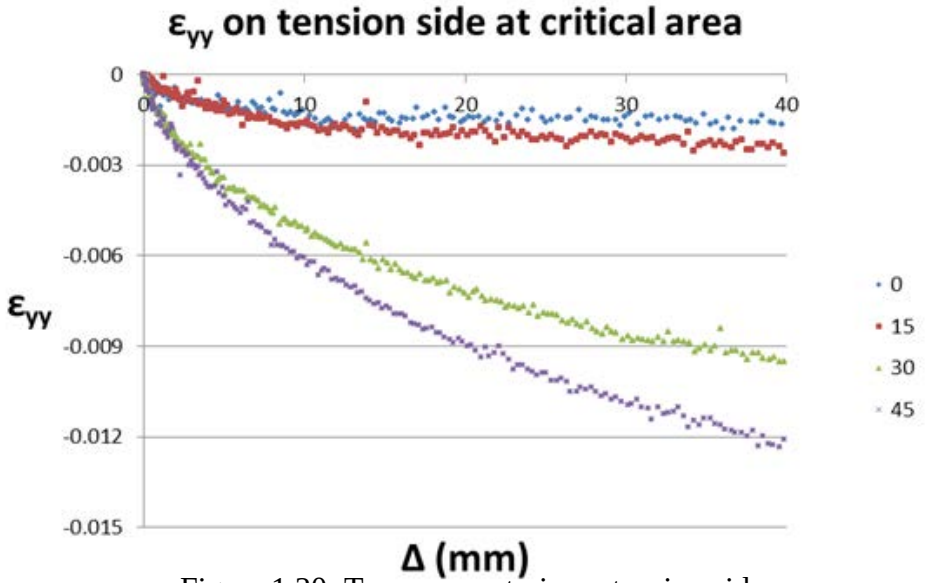

Figure 1.20: Transverse strain on tension side.

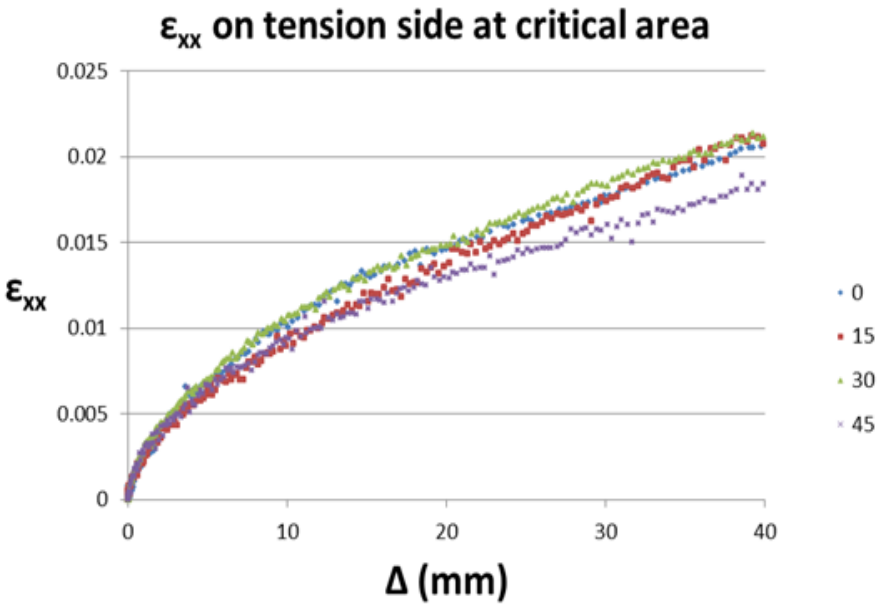

Figure 1.21: Axial strain on tension side.

Though classical lamination theory (CLT) is not strictly applicable for our woven composite system, the authors have used CLT as a predictor for our specimen behavior in the small displacement regime. According to the mechanical properties given in Table 1.2, we can determine the extension-bending coupling matrix B to help understand the relationship between bending and in-plane strains.

For $0^o/90^o$ specimen, only B11 and B22 are non-zero terms in matrix B, which couple in-plane normal forces to bending curvatures, and bending moments to in-plane strains. Experimental evidence to corroborate the presence of coupling is shown in Figures 1.22 and 1.23. Here, it is clearly shown that the in-plane strain ε_{xx} increases with end displacement, which shows positive correlation with bending moment in Figure 1.12. Figures 1.16/1.17 gives this relationship more directly.

In addition, the authors used CLT to help explain the $0/90^o$ specimen response after fiber buckling occurs on the compression side and stiffness is lost (less than 10%) along the axial direction. As the absolute values of B11 and B22 decrease, this leads to

increasing in-plane compressive strain relative to the tension surface. This trend is shown in Figure 1.22 for the $0/90^0$ specimen, where the compressive strain is considerably larger than the tensile values, resulting in through-thickness asymmetry in the axial strain distribution.

Also, CLT theory suggests there is no coupling between bending and in-plane strains for +/- 45^o fiber orientation, This prediction is consistent with observations documented in Figure 1.23, where even for very large axial displacements, the range in strain for ε_{xx} is nearly the same on both compression and tension surfaces.

Additional figures demonstrating the observed relationship between in-plane strain and end displacement are given in Appendix A.

1.3.4 Strain Variations for Small and Large Compressive Displacement

Figures 1.22 and 1.23 shows the axial strain field ε_{xx} on the compression side and tension side of $0^o/90^o$ and $45^o/45^o$ specimens, respectively, when the end displacement Δ equals to 10, 20 and 40mm. In each figure, both full-field data and a line plot in terms of arc length, S, of the data along the specimen centerline are shown. The S coordinate has the same direction as X coordinate, with origin identified by a red arrow on the left edge of the specimen. Appendix A presents the transverse strain field, ε_{yy}, and shear strain field, ε_{xy}, on the compression side and tension sides for $0^o/90^o$ and $45^o/45^o$ specimens, respectively, when the end displacement Δ equals to 10 and 20mm.

.

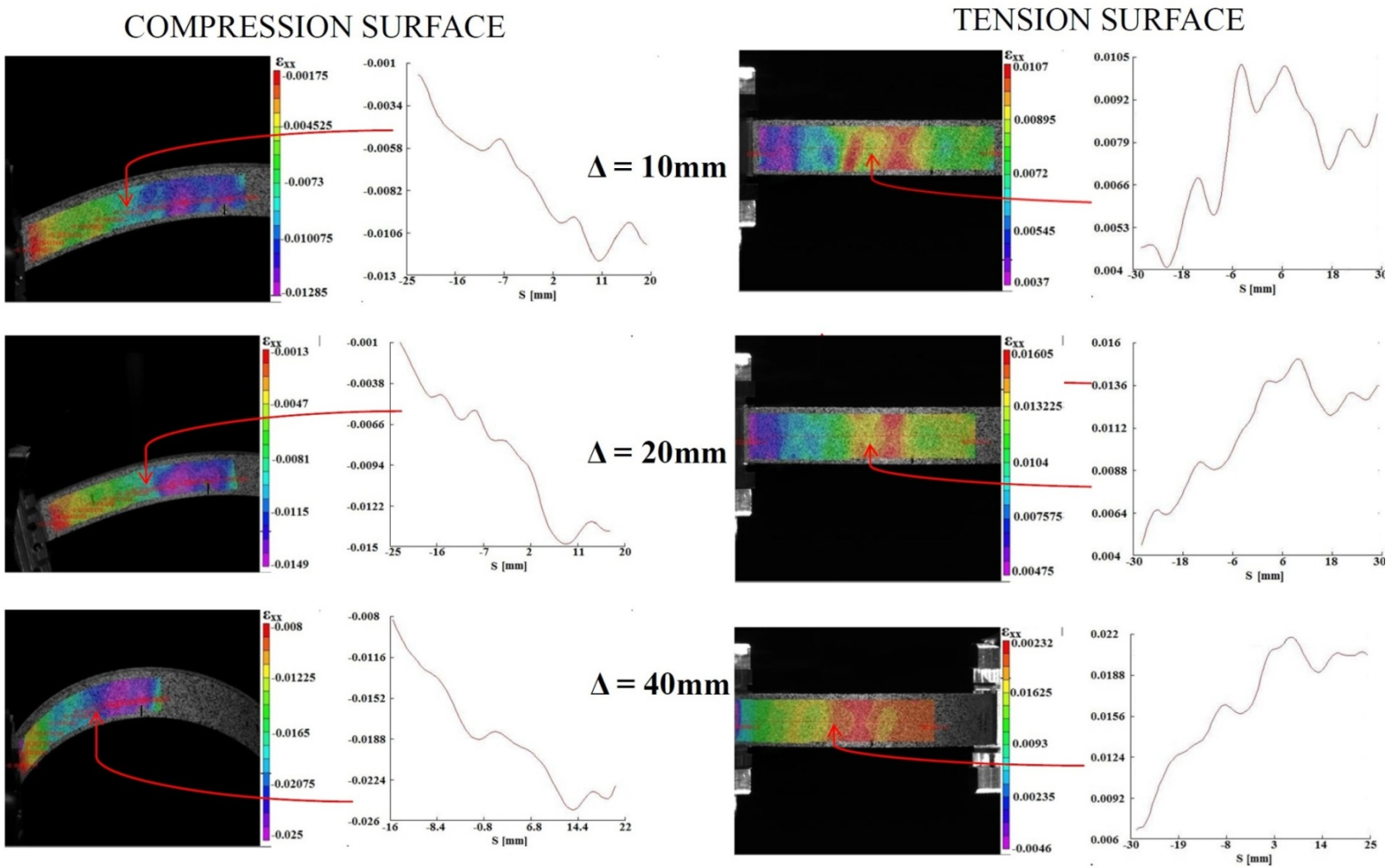

Figure 1.22: Axial ε_{xx} field and centerline plot of ε_{xx} on compression and tension surfaces of $\theta = 0^o/90^o$ specimens for Δ =10mm, 20mm and 40mm.

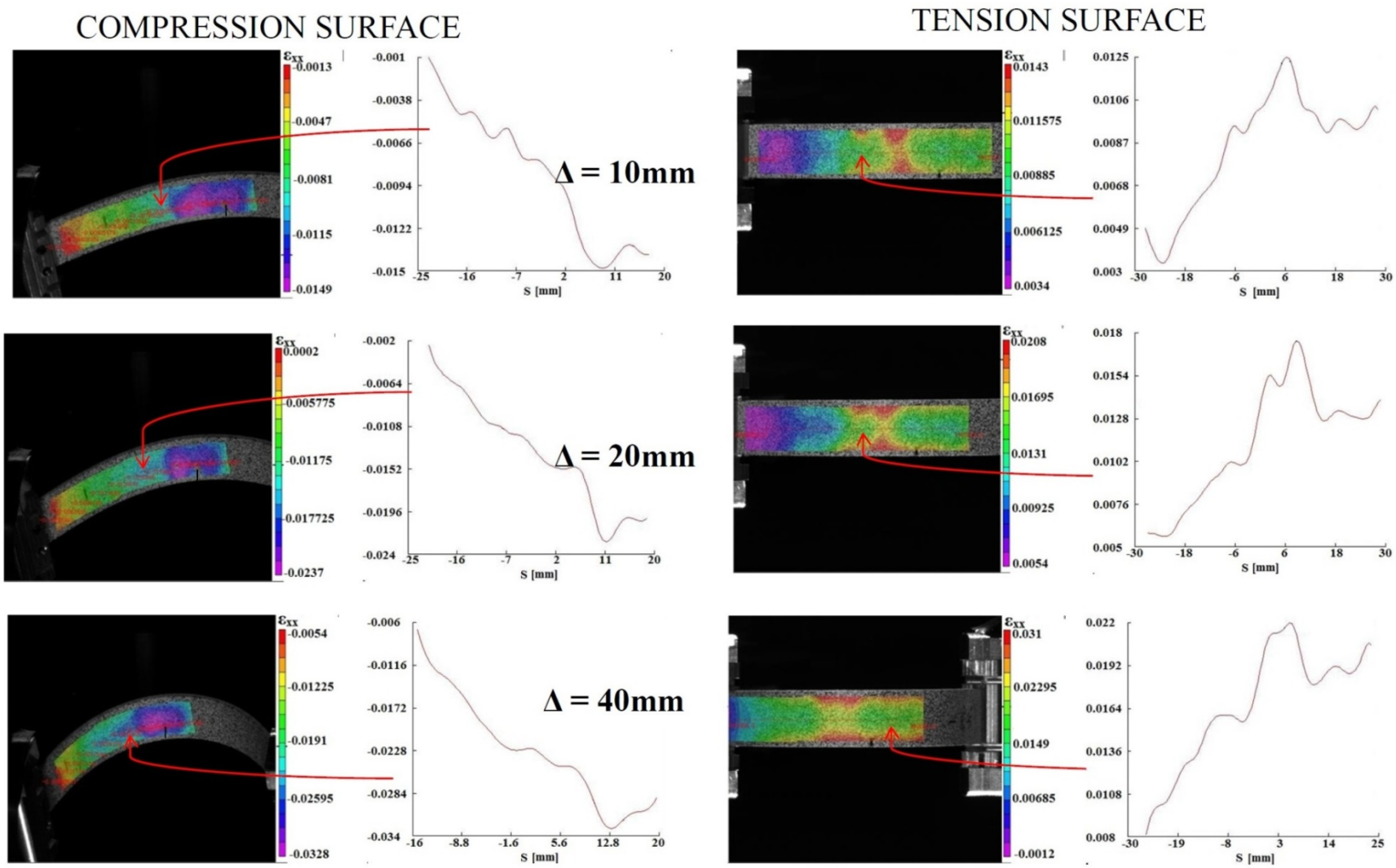

Figure 1.23: Axial ε_{xx} field and centerline plot of ε_{xx} on compression and tension surfaces of $\theta = 45^{o}/45^{o}$ specimens for Δ =10mm, 20mm and 40mm.

Axial Strain Field

Inspection of the tension surface data on the 0/90 specimen in Figure 1.22 clearly shows an oscillatory strain field for Δ = 10mm that is considerably larger than the estimated variability in strain for our measurements. The oscillations in strain are somewhat muted as the deformation increases. These observations are consistent with the expected shear transfer process between fibers and matrix that requires sufficient distance to complete; the distance between peaks is ~10mm for our woven fiber-matrix material system, which is about 10 times of weave size of specimen and physical subset size of DIC, and hence is resolvable by the stereo-vision measurement method. Conversely, for the $45^o/45^o$ specimen, all local peaks in axial strain are muted, suggesting that load transfer processes are relatively insensitive to axial position along the specimen for high fiber angle configurations.

As noted previously, for all fiber angles the general shape of the beam-compression specimen is quite similar for all fiber angles. Even so, the measured strains in the region of final collapse can be quite different, as well as the local curvatures. For Δ=40mm, Figure 1.24 shows the axial strain ε_{xx} distribution along the transverse direction on the compression side for the $0^o/90^o$ and $45^o/45^o$ specimens. It is clear that the strain differences along transverse direction are quite different, most likely due to the effect of increased anticlastic curvature for the $45^o/45^o$ specimen.

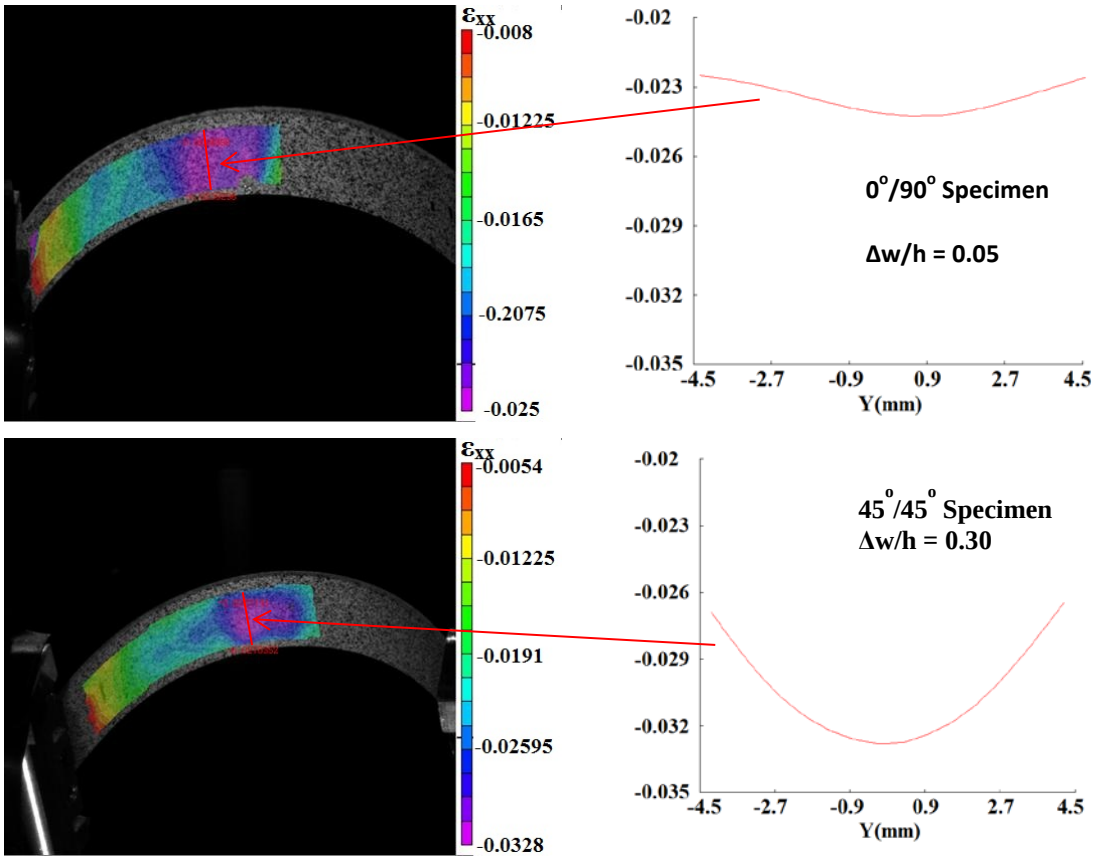

Figure 1.24: Axial strain ε_{xx} distribution along transverse direction on compression side of $0^o/90^o$ (top) and $45^o/45^o$ (bottom) specimen, $\Delta = 40$ mm.

1.3.5 Fiber direction and axial-transverse direction strains in critical region

Using full-field data such as shown in Appendix A, the average ε_{yy} and ε_{xy} on both the tension and compression surfaces in the critical region were obtained (see Footnote 7) as a function of applied moment. By transforming the measured strains from specimen coordinates (x,y) into the primary fiber directions (1,2) as shown in Figure 1.25, Figures 1.26 and 1.27 present the average fiber 2 strain, ε_{22}, vs. moment in the critical region on both compression and tension surfaces for all fiber angles. Figures 1.28 and 1.29 present the average shear strain, ε_{12}, vs. moment in the critical area on both the compression and tension surfaces for all fiber angles.

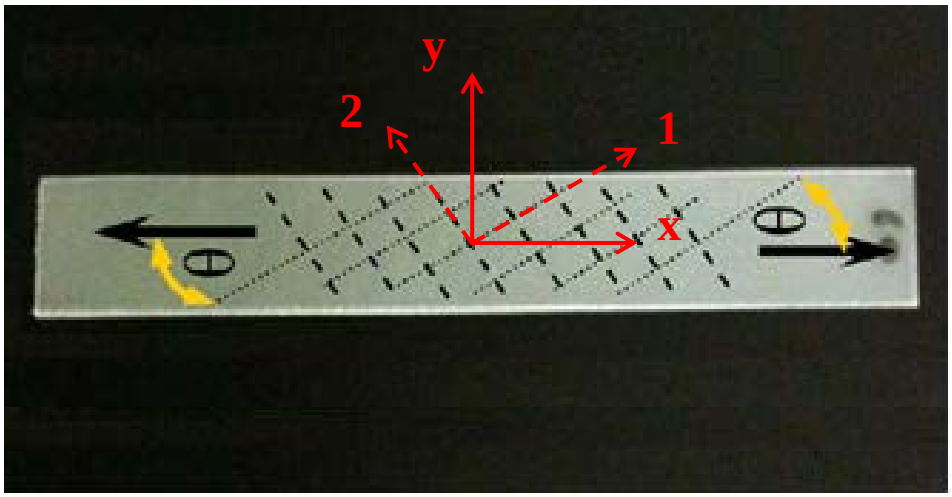

Figure 1.25: Coordinate systems for transformation between specimen and fiber directions.

With regard to the strain ε_{22}, as shown in Figure 1.26/1.27 for 0^o-90^o, 15^o-75^o, 90^o-0^o specimens, ε_{22} is small on both compression and tension surfaces, increasing for 45^o-45^o, 60^o-30^o and 90^o-0^o as the fiber 2 direction orients more closely with the loading direction.

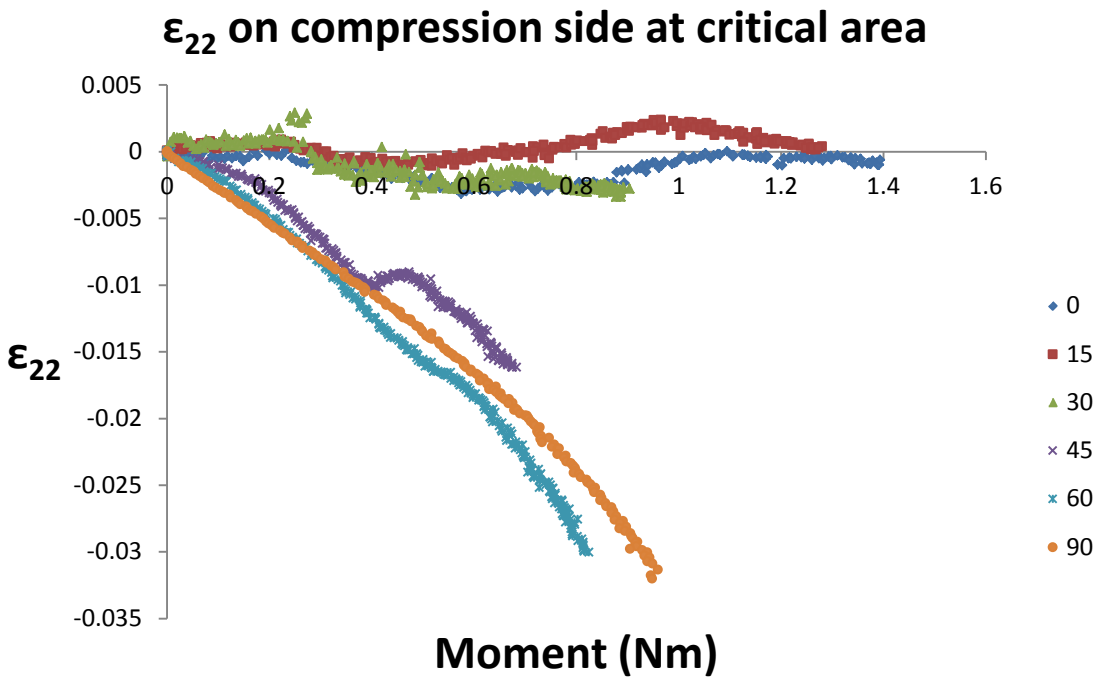

Figure 1.26: Average ε_{22} strain of critical area on compression surface of specimen versus bending moment

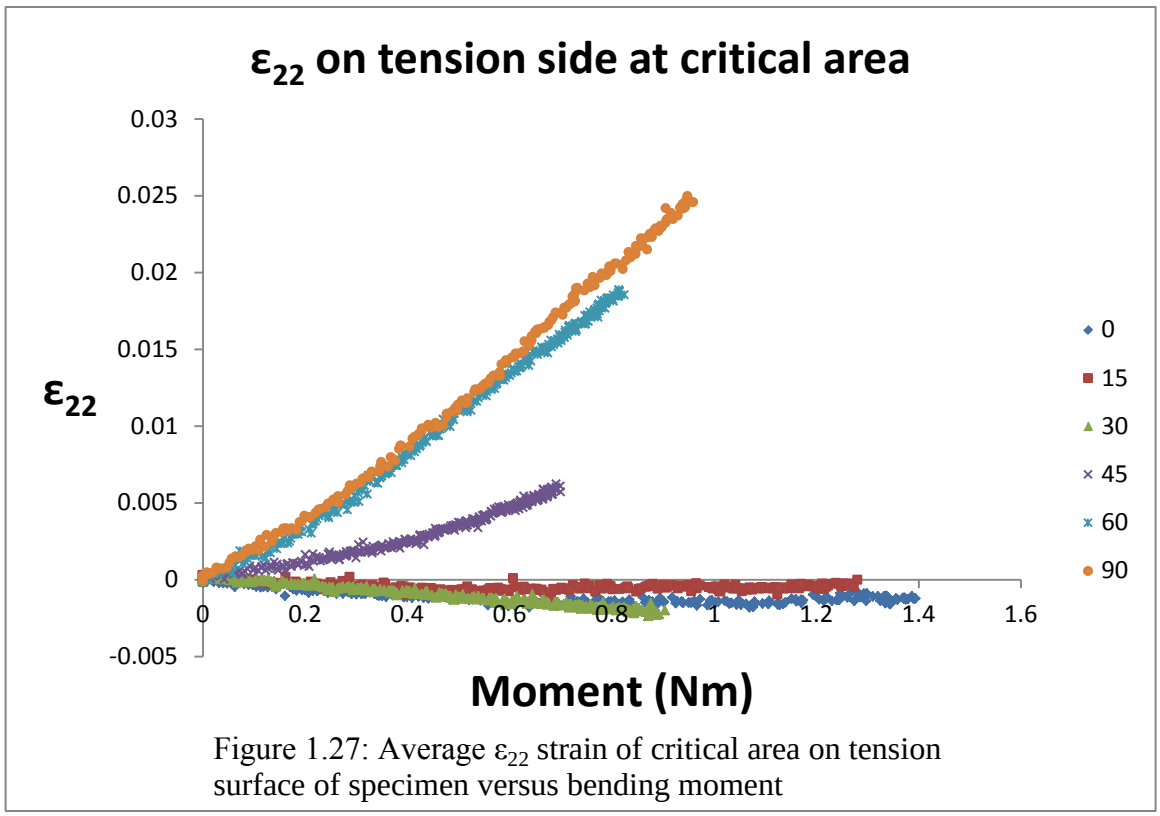

Figure 1.27: Average ε_{22} strain of critical area on tension surface of specimen versus bending moment

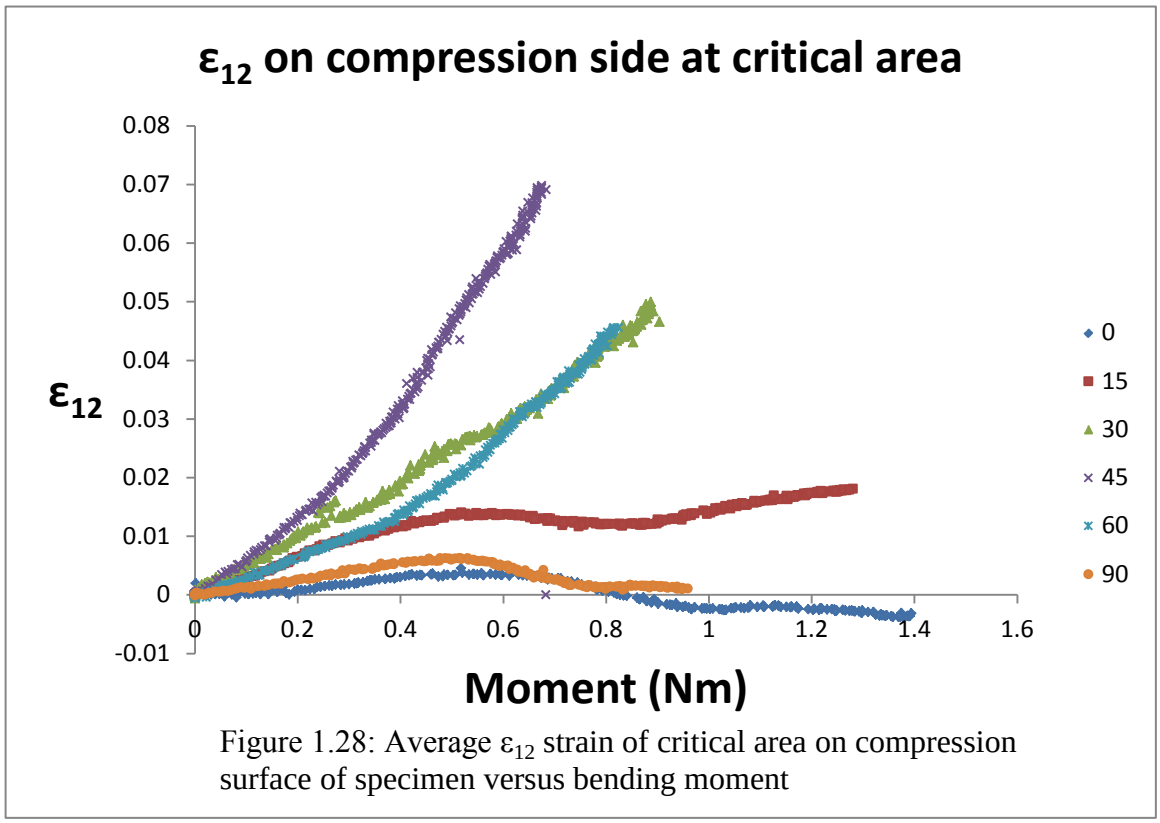

Figure 1.28: Average ε_{12} strain of critical area on compression surface of specimen versus bending moment

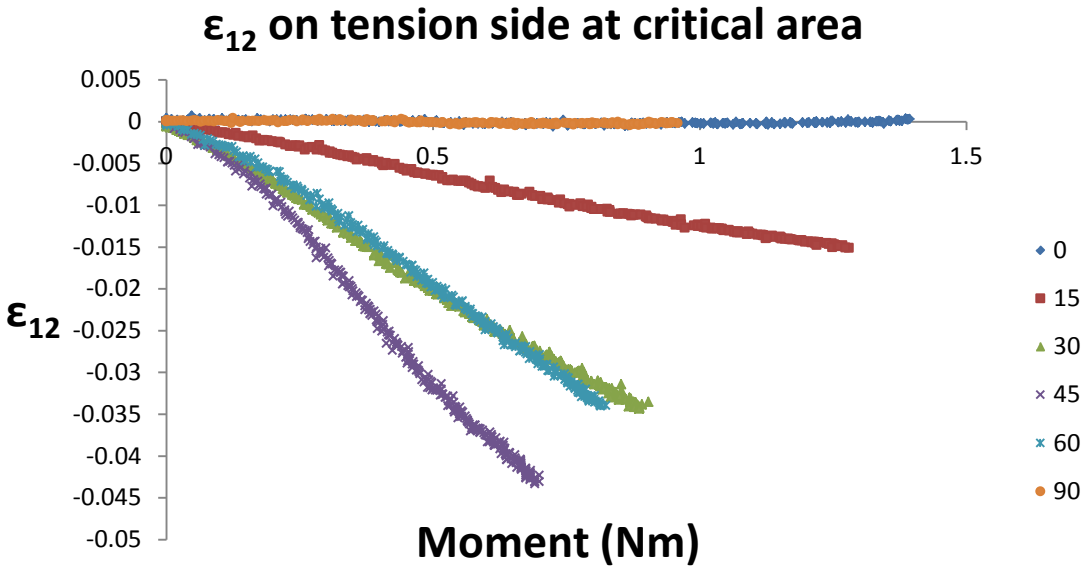

Figure 1.29: Average ε_{12} strain of critical area on tension surface of specimen versus bending moment

As shown in Figures 1.28 and 1.29, the shear strain ε_{12} is negligible between the fiber directions for both 0^o and 90^o specimens, consistent with expectations and demonstrating that any fiber motions were essentially rigid rotations on the macroscale. With regard to other fiber orientations, as shown in Figures 1.28 (1.29), increasing positive (negative) shear strain was measured as the fiber angle increased from 15^o to 45^o or decreased from 90^o to 45^o on the tension (compression) surfaces. Thus, our measurements indicate that the fiber directions 1 and 2 rotated towards (away from) each other on the tension (compression) surfaces, an observation that is consistent with theoretical predictions and physical expectations.

1.3.6 Poisson's Ratio

In addition to the fiber oriented strain data, measurements reveal an approximate linear relationship between transverse strain ε_{yy} and moment for all fiber angles. Consistent with the results in Figures 1.16 and 1.17, which show a linear relationship between axial strain and M_{max}. The results indicate that the ratio between axial and

transverse strain is essentially constant throughout the deformation process. This is also true for 30-60, 45-45 and 60-30 specimens, which have much larger transverse strains (nearly 50% of axial strain).

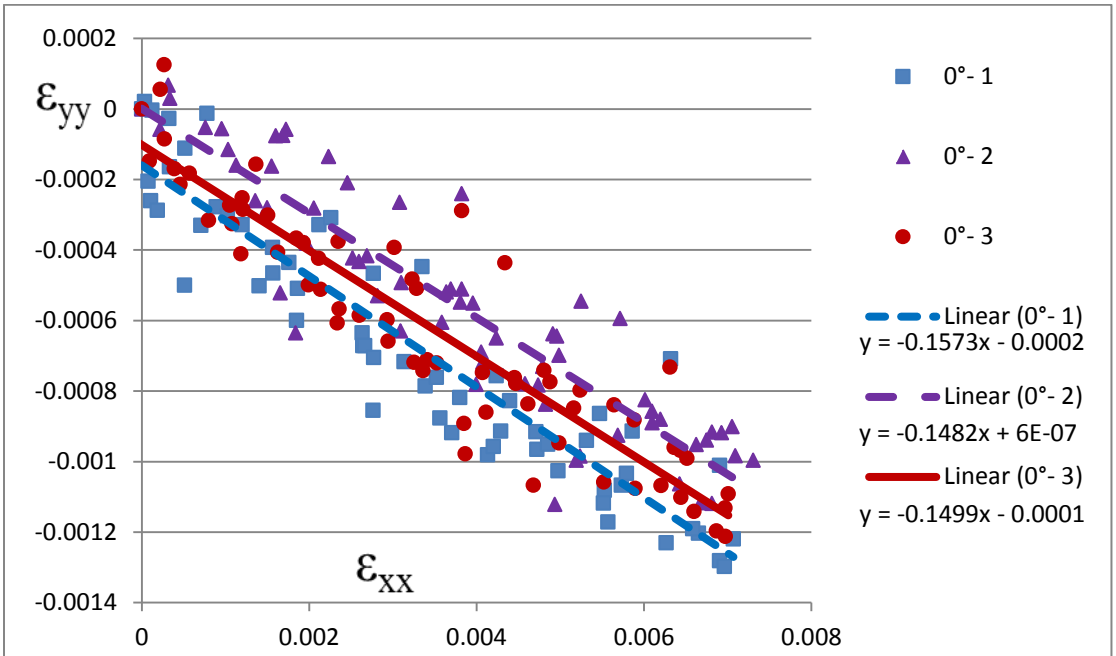

Figure 1.30: ε_{yy} Versus ε_{xx} on tension side for 0° specimens

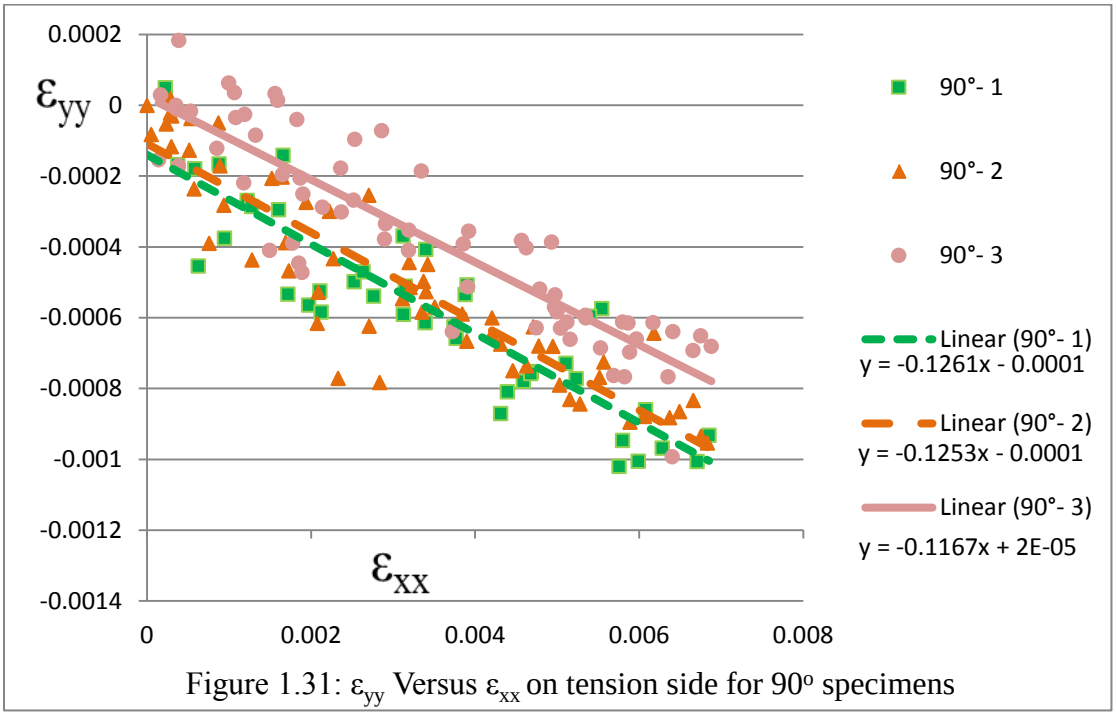

Figure 1.31: ε_{yy} Versus ε_{xx} on tension side for 90° specimens

Using the measured axial and transverse strains for three 0^o and three 90^o specimens in small deformation region (maximum strain less than 0.8%), the investigators computed the average ν_{12} and ν_{21}, respectively, for the specimen on the tension and compression surfaces. On the tension surface, the investigators obtained $\nu_{12} = 0.152$ +/- 0.005 and $\nu_{21} = 0.122$ +/- 0.005, which is graphically shown in Figure 1.30 and 1.31. This result is in good agreement with recent findings of Pollock et al [22] where $\nu_{12} = 0.15$ and $\nu_{21} = 0.13$.

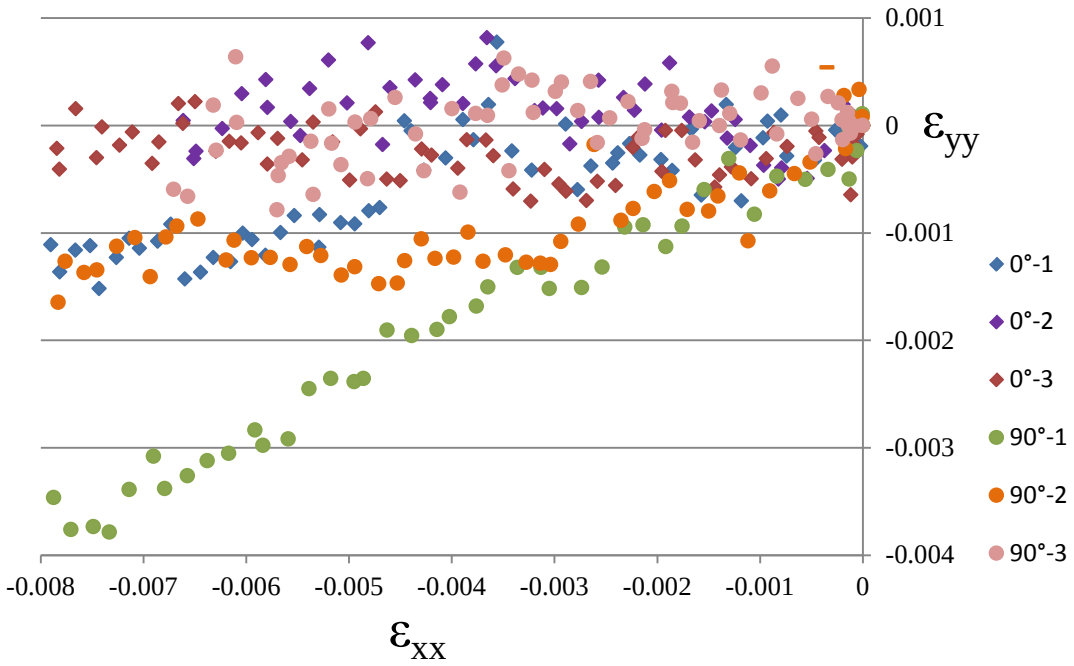

Figure 1.32: ε_{yy} Versus ε_{xx} on compression side for 0^o and 90^o specimens

On the compression surface, the investigators observed a different behavior in Poisson's ratio. Graphically, this is shown in Figure 1.32 for 0^o and 90^o specimens. Though there is considerable scatter in the data in Figure 1.32, the investigators obtained $\nu_{12} \approx 0$ and $-0.10 \leq \nu_{21} \leq -0.40$. With regard to the somewhat anomalous behavior on the compression side for Poisson's ratio, the investigators observed that Poisson's ratio on the compressive surface varied considerably across the specimen width at various axial

positions. This anomalous behavior is also shown graphically in the ε_{yy} results on compression side presented in Figures A.1 and A.2. Specifically, our compression-surface measurements indicate that Poisson's ratio is small near the specimen centerline, becoming either negative near the edges or positive near the edges of the 0^o and 90^o specimens, depending upon the axial position that is selected. The variability shown in Figures A.1 and A.2 demonstrate that compressive effects in woven composite components can lead to highly localized deformations due to effects such as fiber buckling or crimping.

Figure 1.33 shows the experimental $\varepsilon_{yy}/\varepsilon_{xx}$ results on tension side for all fiber orientation specimen and Poisson's Ratio values quantitatively determined using the equations in [22]. All experiment results in plot are close to theoretical expectations except for 45 degree specimen, which is 20% higher than predicted.

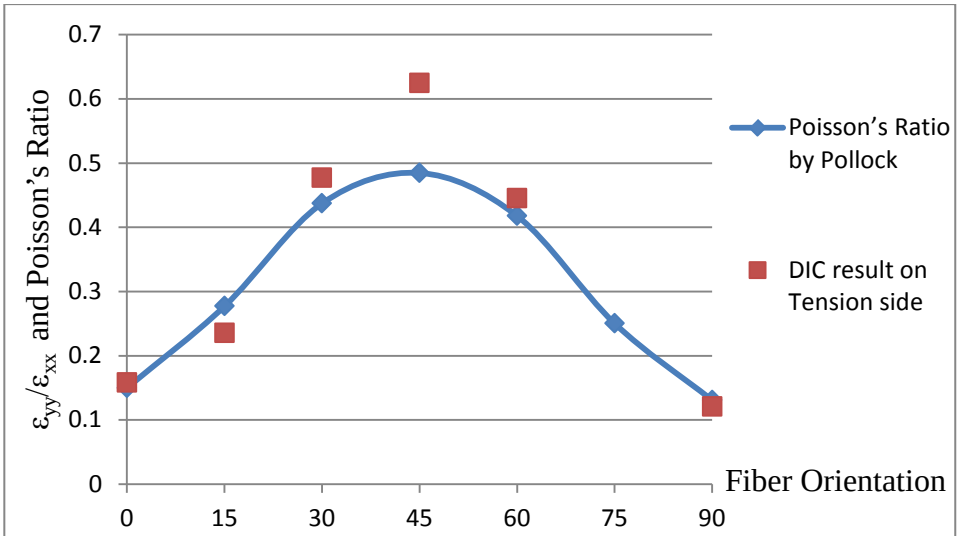

Figure 1.33: Comparison of experimental $\varepsilon_{yy}/\varepsilon_{xx}$ values on tension side and Poisson's Ratio theory result for all fiber orientation specimen

1.4 Theoretical Model

To analyze the loading process for the experiment described in Section 3, the author analyses both the small deformation situation, which uses the Euler–Bernoulli beam theory, and the large deformation situation which uses a modified Drucker's equation.

1.4.1 Euler–Bernoulli beam theory

The Euler–Bernoulli beam theory is a simplification of the linear theory of elasticity which provides a means of calculating the load-carrying and deflection characteristics of beams. The common orthogonal coordinate system used for all analysis is shown in Figure 1.34.

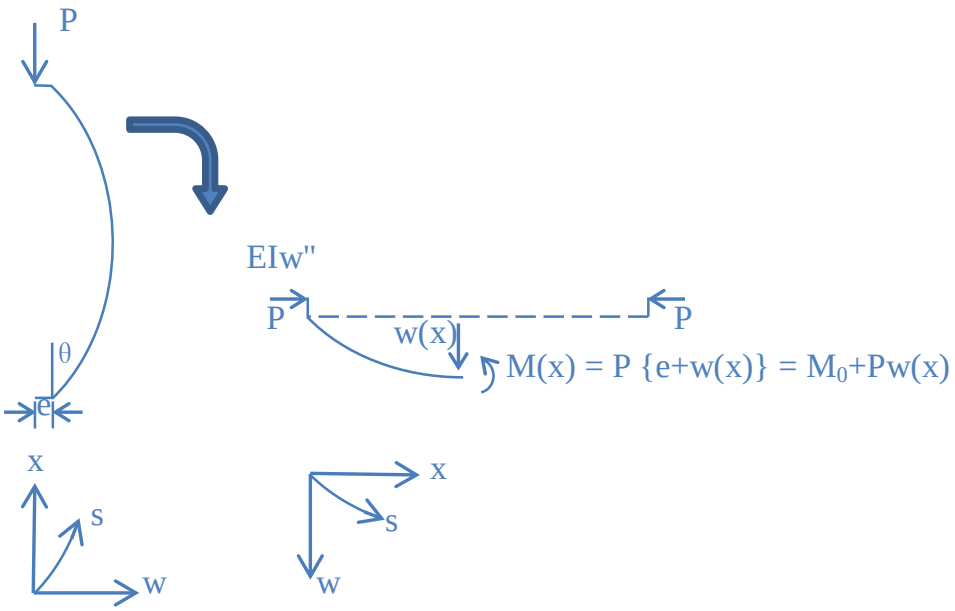

Figure 1.34: Coordinates Setup.

Here, x is along the original beam length, s is arc length along the beam at any loading, w is the transverse displacement of the beam at any x or s position, and e is the load eccentricity. Appendix B provides the detail theoretical development, leading to the following solution for the out-of-plane displacement;

$$w(x) = e \times (-1 + \cos \lambda x + \frac{1 - \cos \lambda L}{\sin \lambda L} \sin \lambda x) \quad (1)$$

with $\lambda = (P/ E_\theta I)^{1/2}$, where E_θ is the Young's modulus obtained during axial loading of a specimen with fiber orientation θ relative to the loading axis. The Euler-Bernoulli expression in Equ (1) is valid only for small strains and small rotations. It will have substantial errors for large deflections of a cantilever beam because the elementary theory neglects the square of the first derivative in the curvature formula, which gives an increasingly important contribution to the solution for large deflection problems.

1.4.2 Large Deformation of Beams

In 1945, Bisshopp and Drucker [51] presented a new theory which corrects for the shortening of the moment arm as the loaded end of the beam deflects. As shown in Figure 1.35, key parameters in the development are related to the arc length, s, which is required to analyze large deflection bending analyses.

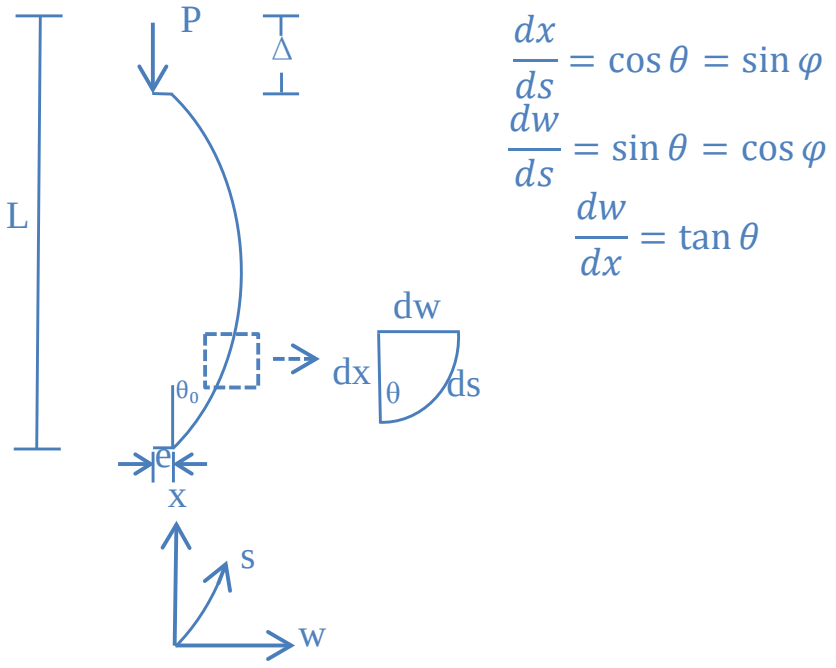

Figure 1.35: Differential relationship.

The differential equation describing beam-column response under large deflections as shown in Figure 1.35 is written as:

$$M_0 + Pw(s) = M(s) = -EI\frac{d^2w}{ds^2} = -EI \times \frac{d\theta}{ds} \tag{2}$$

Assuming that the load eccentricity, e, is small, the solution for the large deformation response of a bending compression member is given in Appendix B, resulting in the following key results for the axial load and lateral displacement;

$$P = \frac{4\left[F(k)\right]^2 EI}{L^2} \tag{3}$$

where k is the elliptic modulus or eccentricity, and F(k) is the complete elliptic integral of the first kind in trigonometric form ;

$$F(k) = \int_0^{\frac{\pi}{2}} \frac{d\beta}{\sqrt{1-k^2\sin^2\beta}} \tag{4}$$

Thus,

$$w = -\sqrt{\frac{EI}{2P}}\int_{\theta_0}^{\theta} \frac{1}{\sqrt{\cos\theta - \cos\theta_0}}\sin\theta d\theta = \sqrt{\frac{2EI}{P}} \times \sqrt{\cos\theta - \cos\theta_0} \tag{5}$$

where, as shown in Figure 1.35, θ_0 is the end rotation angle of the specimen about the unrestrained z-axis, and

$$\cos\theta = 1 - 2k^2\sin^2\beta \qquad \cos\theta_0 = 1 - 2k^2 \tag{6}$$

Figure 1.36 shows the relationship between experimental and predicted trends between end compression load, P, and the maximum lateral beam deflection at the middle of the specimen, w_{max}, for a nominally isotropic fiber orientation (0-90). Results indicate that the linear theory is in excellent agreement with experimental measurements during

the early stages, eventually diverging as the beam approaches the buckling load. As the load increases further, trends in the large deformation prediction are in good agreement with experimental results beyond the initial "buckling" load, though slightly over-predicting the required loading for continued deformation. The deviation observed for larger loading will be reviewed in more detail in the Discussion section.

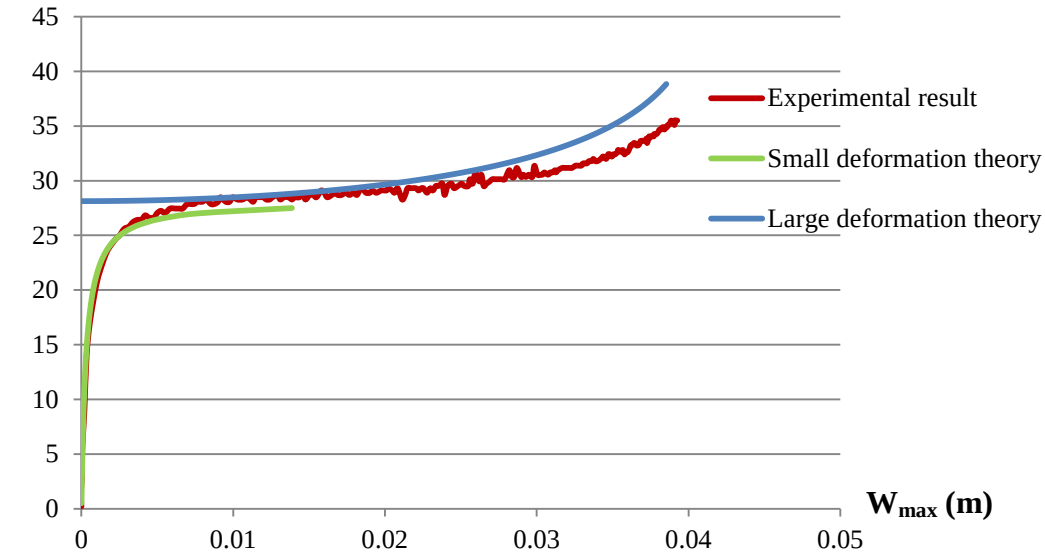

Figure 1.36: Load versus maximum beam displacement at x=L/2 for 0-90 fiber orientation.

1.4.3 Shape and Strain Estimates

Since specimen strain is related directly to the bending shape, both the shape of specimen and the strain at each point along the length can be determined for each applied load and axial displacement. The results are given in Appendix B and the key results are presented below.

$$\Delta = L - L\times\cos\theta_0 - 4\times\sqrt{\frac{EI}{P}}\times E\left(k,\frac{\pi}{2}\right) + 2\times\sqrt{\frac{EI}{P}}\left(1+\cos\theta_0\right)\times F\left(k,\frac{\pi}{2}\right) \qquad (7)$$

Using Equ (B-27) in Appendix B, this expression can be written as follows;

$$\Delta = L - L \times \cos\theta_0 - 2L \times \frac{H(k)}{F(k)} + L \times (1 + \cos\theta_0) \qquad (8)$$

With Equ (8), we can define the relationship between the end displacement, Δ, and the deflection, w(x), along the x-direction throughout the entire bending and compression loading process. Furthermore, for nominally isotropic material response, this relationship is independent of the modulus, E, suggesting that both $0^o/90^o$ and $-45^o/+45^o$ fiber orientation specimens may have similar deflected shapes along the axial direction.

Figures 1.37a and 1.37b present the predicted (blue line) and measured (red line) shape of the beam centerline for $0^o/90^o$ and $-45^o/+45^o$ fiber angles, respectively, for Δ=10mm, 20mm and 40mm. As anticipated, the shape of the beam centerline is accurately predicted for all cases. This observation is expected to be true since the experiment was performed in displacement control where large deformation beam theory should provide excellent agreement. It should be pointed out that the experimental loads to achieve these deformed shapes are slightly over-predicted by the large deformation theory (see Figure 1.36 for the $0^o/90^o$ fiber orientation results).

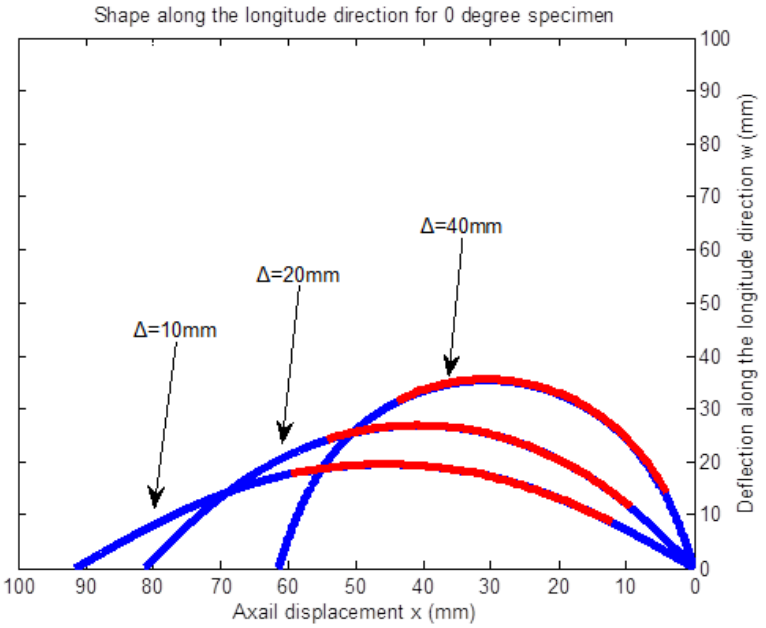

(a)

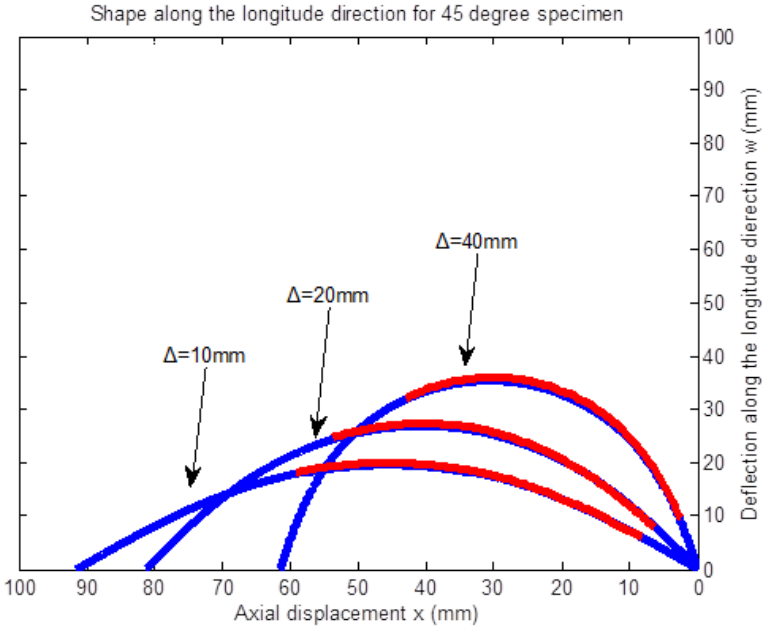

(b)

Figure 1.37: Shape of the beam: (a) $0^o/90^o$ specimen; (b) $-45^o/+45^o$ specimen. Blue line is the theoretical prediction. Red line represents the experimental measurements.

According to Equ (B-15) in Appendix B, the curvature of specimen can be expressed as a function of load P and rotation angle θ as follows;

$$\frac{1}{\rho}=\frac{d\theta}{ds}=-\sqrt{\frac{2P}{EI}}\times\sqrt{\cos\theta-\cos\theta_0} \tag{9}$$

where ρ is the radius of curvature along the primary beam axis. If we assume the neutral surface is at the mid-plane through the specimen thickness, the surface strain prediction under large deformation is written:

$$\varepsilon_{xx}=-\frac{h}{2}\times\frac{1}{\rho}=-\frac{h}{2}\times\frac{d\theta}{ds}=\frac{h}{2}\times\sqrt{\frac{2P}{EI}}\times\sqrt{\cos\theta-\cos\theta_0} \tag{10}$$

Using Equ (B-27) and (B-30), this expression can be simplified to give;

$$\varepsilon_{xx}=\frac{h}{2}\times\frac{Pw}{EI}=2h\times\frac{\left[F(k)\right]^2}{L^2}\times w \tag{11}$$

where w(x,y) is the out of plane displacement at the section of interest.

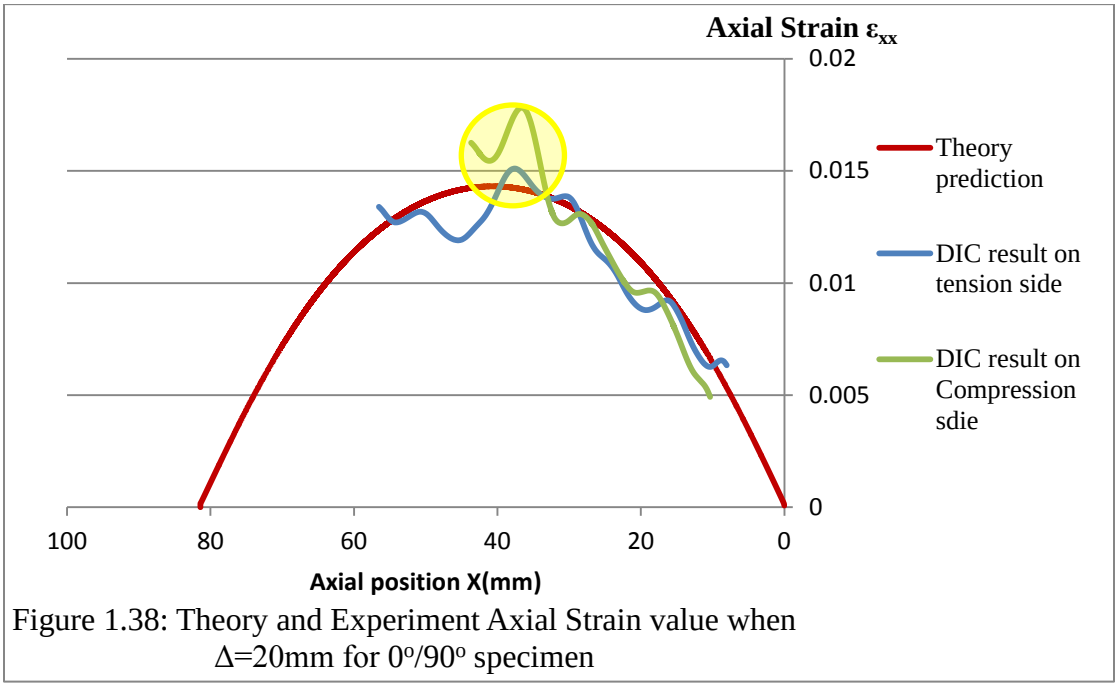

Figure 1.38: Theory and Experiment Axial Strain value when Δ=20mm for 0°/90° specimen

For 0°/90° specimen with axial displacement Δ = 20mm, Figure 1.38 compares both large deformation predictions (red line) and experimental measurements on the tensile (blue line) and compressive (green line) sides of the specimen. Although there are

oscillations in the measured strain field caused by the heterogeneous nature of the composite, the theoretical strain results and trends are in very good agreement with the experimental measurements (Appendix B discusses the accuracy of the strain measurements). It is noted that the compression side result deviations from the predictions are in the most highly strained region near mid-length. In this region, the authors observed the presence of fiber buckling[9] on the compression surface when $\Delta \geq$ 20mm, which most likely contributed to the increase in measured macroscopic deformation. Figure 1.39 shows the detail axial ε_{xx} field and centerline plot of ε_{xx} on compression and tension surfaces of $\theta = 0^o/90^o$ specimens for Δ = 20mm.

Additional evidence to support this conjecture is given in Figure 1.39, which focuses on the evolution of axial strain[10] ε_{xx} vs. end displacement in this critical region on both the tension and compression surfaces of the specimen. In the small deformation regime (axial strain less than 0.3-0.5%), the theoretical prediction matches the tension and compression experimental results. However, beyond this point the strain values on the compression side begin to deviate by increasing amounts from both the theoretical predictions and the tensile data, with microbuckling evident on the compression surface in the high strain region of the specimen.

[9] Another factor that contributes to composite failure, and is assumed to be an independent mechanism, is fiber kinking. The authors did not observe isolated fiber kinking in the initial specimens, nor in the damaged specimens, in these studies though some fiber kinks appeared in the micro-buckled regions of the specimen. Such observations are consistent with the work of Sun and Tsai [55] and Panasart et al [56] who noted that fiber kinking is likely initiated during micro-buckling and may not be an independent failure mechanism in many cases.

[10] Axial strain in the critical area is obtained by averaging the strain values within a 5mm diameter region that is centered at the specimen mid-span and mid-width.

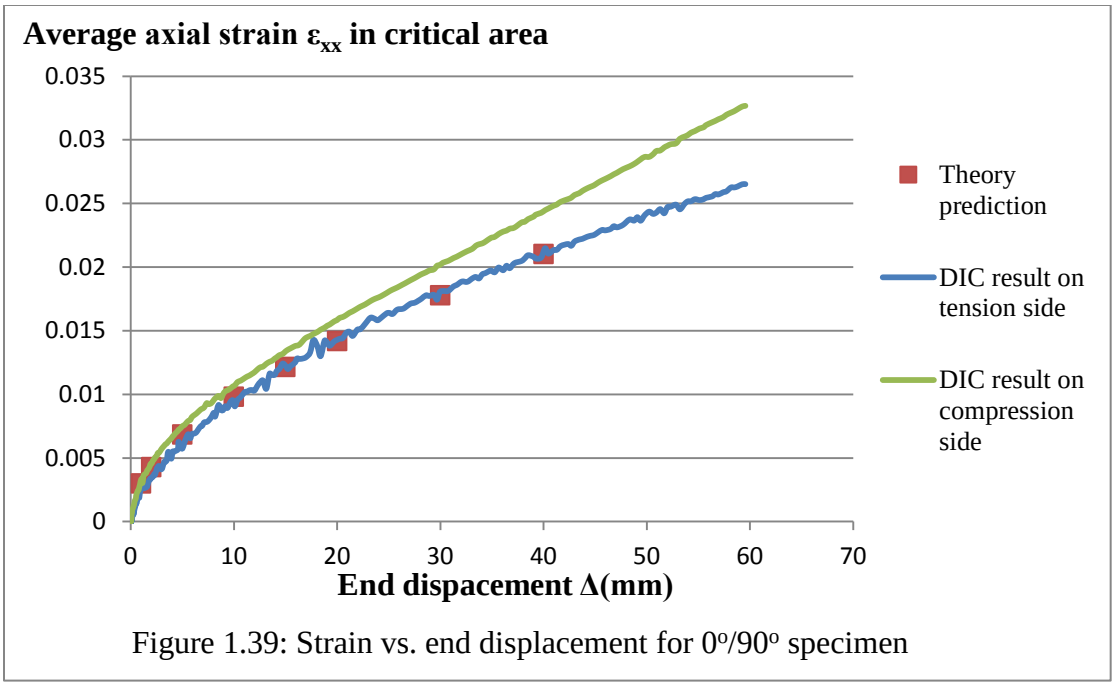

Figure 1.39: Strain vs. end displacement for $0^o/90^o$ specimen

Since the local reaction bending moment at mid-length is a monotonic function of end-point displacement throughout the loading process, including the influence of both the applied load and the transverse deflection, Figure 1.40 shows how the axial strain component at L/2 evolves with increasing bending moment M(L/2) for $0^o/90^o$ specimens. Inspection of Figures 1.39 and 1.40 clearly shows that (a) the compression side axial experiment result matches the theoretical prediction for $\varepsilon_{xx} \leq 0.003$, and (b) the tension side axial strain agrees with predictions for $\varepsilon_{xx} \leq 0.010$. The deviations shown in Figures 1.39 and 1.40 appear to be early indicators of increasing damage during the deformation process, though other factors may also affect the comparison.

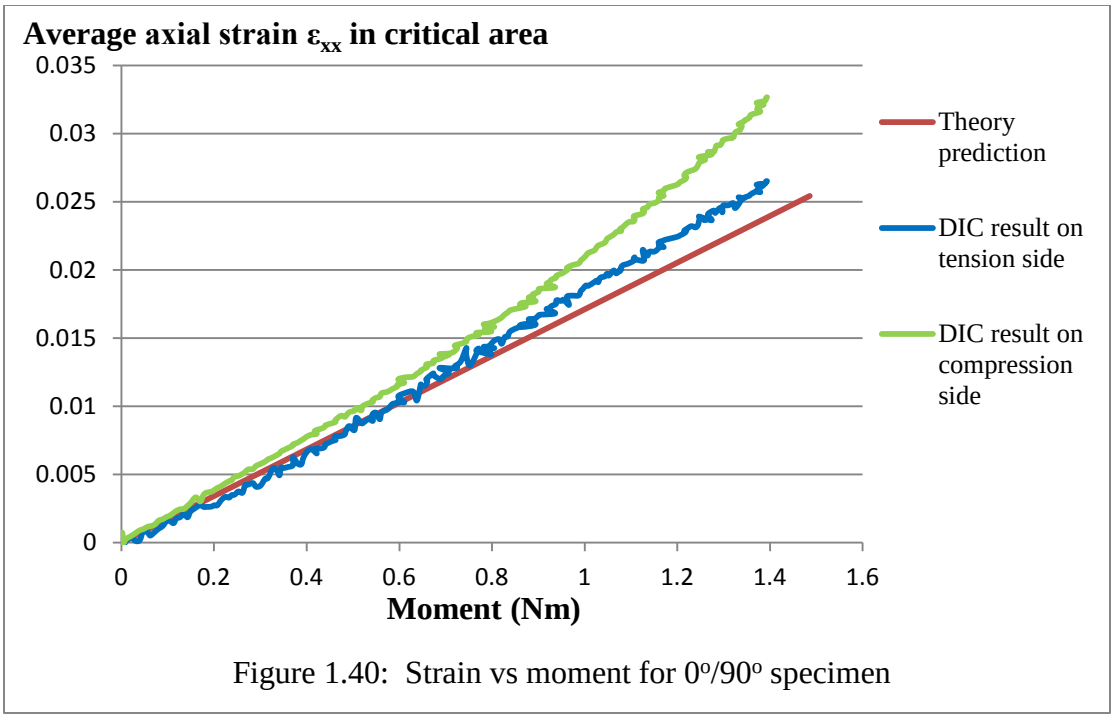

Figure 1.40: Strain vs moment for 0°/90° specimen

1.5 Effective Stress and Effective Strain

The theory for determining engineering constants and developing a single equation that describes the macroscopic/continuum behavior of a composite into the non-linear regime, regardless of specimen orientation, has been developed and employed by investigators in the past few decades, including Sun [2], Dvorak [3], Kenaga [13], Reifsnider et al [19-21], and Pollock et al [22], who used the concepts to extract specific elastic composite material properties.

Assuming a planar state of stress and an orthotropic material system aligned with the primary fiber direction, then the stored energy function can be written;

$$w = \frac{1}{2}\left(a_{1111}\sigma_{11}^2 + a_{1122}\sigma_{11}\sigma_{22} + a_{2222}\sigma_{22}^2 + a_{1212}\sigma_{12}^2\right) \tag{12}$$

where

$$a_{1111} = 1/E_1, \quad a_{2222} = 1/E_2, \quad a_{1122} = -\nu_{12}/E_1, \quad a_{1212} = 1/G_{12} \tag{13}$$

Here, it is further assumed that $\sigma_{33} = \sigma_{13} = \sigma_{23} = 0$ in our thin compression-bending specimen, with the end conditions determined using the measured axial loading and bending moment.

By transforming the measured strains from specimen coordinates (x,y) into the primary fiber directions (1,2) as shown in Figure 1.41, the stresses along the fiber axes 1 and 2 can be written in terms of the axial stress, σ_θ, as follows

$$\sigma_{11} = \sigma_\theta \cos^2(\theta), \quad \sigma_{22} = \sigma_\theta \sin^2(\theta), \quad \sigma_{12} = -\sigma_\theta \sin(\theta)\cos(\theta) \qquad (14)$$

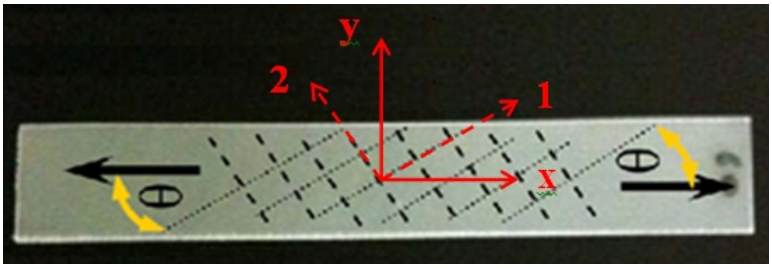

Figure 1.41: Coordinate systems for transformation between specimen and fiber.

Combining Equations (12) and (14), the following form for the stored energy is obtained;

$$w = \frac{1}{2}\sigma_\theta^2\left[\frac{1}{E_1}\cos^4(\theta) + \left(\frac{1}{G_{12}} - \frac{2\upsilon_{12}}{E_1}\right)\sin^2(\theta)\cos^2(\theta) + \frac{1}{E_2}\sin^4(\theta)\right] \qquad (15)$$

If we define the "axial" stress as σ_θ when the direction of applied loading at an angle θ relative to the primary fiber direction[11], then the component of axial strain along the direction of applied loading is ε_θ and it is given by;

[11] There are two primary fiber directions for an orthogonal weave. During CT scanning of this material, it was observed that one of the primary directions had slightly more fibers per unit volume than the companion orthogonal set. Thus, the "primary fiber direction" is based on the direction with maximum load in a tension test, which also has the larger number of fibers.

$$\varepsilon_{\theta} = \frac{\partial w}{\partial \sigma_{\theta}} = \frac{\sigma_{\theta}}{E_1}\, h^2(\theta) \tag{16}$$

For woven composites with nonlinear deformation, Xing and Reifsnider [21] defined h(θ) as

$$h(\theta) = \sqrt{\frac{3}{2}[\cos^4(\theta) + c_1 \sin^4(\theta) + 2c_2 \sin^2(\theta)\cos^2(\theta)]} \tag{17}$$

In the linear elastic region, we can determine the value of c_1 and c_2 by the material properties,

$$c_1 = \frac{E_1}{E_2} \qquad c_2 = \frac{E_1}{2G_{12}} - \upsilon_{12} \tag{18}$$

Consistent with Reifsnider work [19-21], we can define an effective stress $\tilde{\sigma}_{\theta}$, and the corresponding effective strain $\tilde{\varepsilon}_{\theta}$ as follows;

$$\tilde{\varepsilon}_{\theta} = \frac{\varepsilon_{\theta}}{h(\theta)} \quad , \qquad \tilde{\sigma}_{\theta} = \sigma_{\theta} h(\theta) \tag{19}$$

In this study, the stress σ_{θ} is determined using Equ (20), where the mechanical loads and specimen dimensions are determined experimentally, with the effective strain obtained by transforming the measured strain field, which uses the axial specimen direction as x and the transverse specimen direction as y.

$$\sigma_{\theta} = \frac{P \times \cos\varphi}{A} \pm \frac{M \times h}{I} = \sigma_{xx}, \quad \varepsilon_{\theta} = \varepsilon_{xx} \tag{20}$$

It is worth noting that the ratio of effective strain and stress using Eq (19) can be written as follows;

$$\frac{\tilde{\varepsilon}_{\theta}}{\tilde{\sigma}_{\theta}} = \frac{1}{E_1} \tag{21}$$

Thus, it is evident that $\tilde{\varepsilon}_\theta / \tilde{\sigma}_\theta$ should equal a constant regardless of the orientation of the specimen, indicating that Equ (21) provides a framework for extracting a "single" stress-strain relationship for a specimen. To assess the utility of Equ (21) in these studies, Figure 1.42 and Figure 1.43 show the effective stress and strain relationship obtained on both the compression and tension surfaces under bending-compression loading, respectively. Inspection of Figures 1.42 and 1.43 shows that, the results for all fiber orientation specimens are nearly identical when the effective strain is less than 0.004 on both sides. Thus, in this region, the values of parameter c_1 and c_2 obtained using the elastic material properties are sufficient to characterize the effect of fiber orientation and collapse all of the experimental data into a signal master curve. These results are consistent with previous work by Sun [7] for a single parameter model and Ogihara [19] for a dual parameter model which indicated that for tensile specimens, even in the non-linear range it is oftentimes possible to use effective properties and obtain a "single master curve".

For our bending specimen, beyond this initial region, the results deviate from this single functional form as the deformation increases further. Consistent with the work of Ogihara and Sun, the authors varied c_2 to seek an optimal coalescence of the results. However, in this case, there was limited improvement since the +/-45^o results did not coalesce with the remaining angles. As noted by Sun [7] the effective stress and strain concept will be effective only when the matrix damage is dominant and the fibers do not participate in the nonlinear response in any substantial way. In our case, fiber rotation was observed in the +/-45^o specimen as the deformations and damage increased. Furthermore, significant fiber buckling was observed on the compression side as the

damage increased for most fiber angles. Taken together, these observations indicate that it is unlikely that a single master curve can be identified in the larger strain range for our bending specimen using these effective stress and strain concepts.

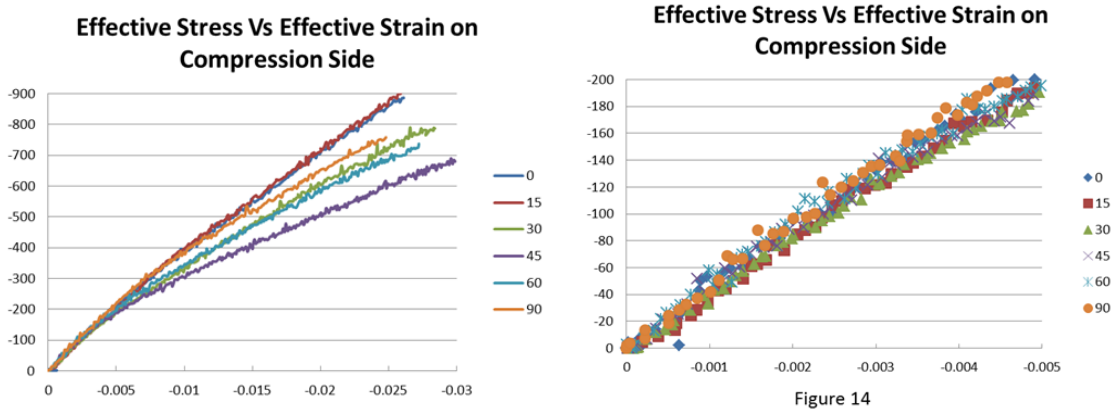

(a) (b)

Figure 1.42: Effective stress versus the effective strain on the compression side for all fiber orientation. (a) Maximum axial strain from 0.000 to -0.030; (b) Maximum axial strain from 0.000 to -0.005

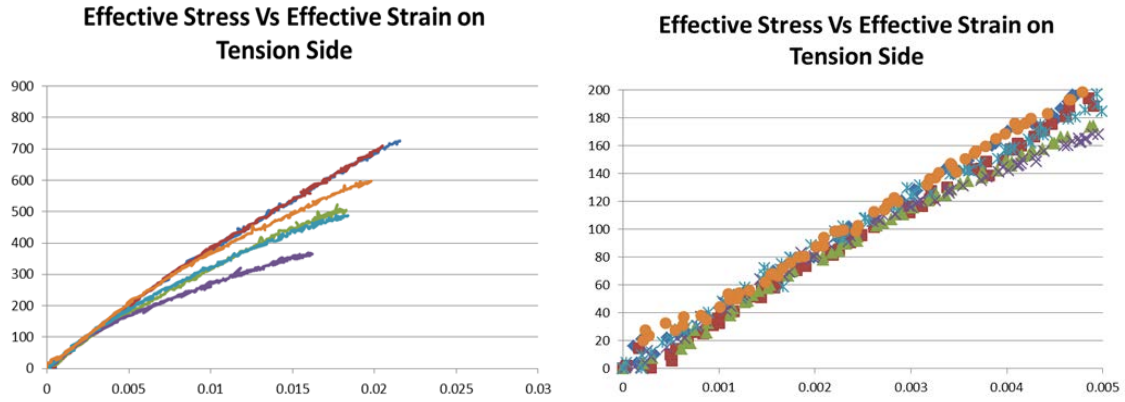

(a) (b)

Figure 1.43: Effective stress versus the effective strain on the tension side for all fiber orientation. (a) Maximum axial strain from 0.000 to 0.030; (b) Maximum axial strain from 0.000 to 0.005

1.6 Finite Element Analyses

To further explore the applicability of σ_{eff} - ε_{eff} concepts for characterizing the compression and tensile response, a finite element analysis of the beam-compression

member is performed by the authors. The explicit[12] finite element code, Abaqus [57], was selected for this investigation. All models were defined using (a) reduced integration solid elements CPE4R and (b) shell elements in the Abaqus/Explicit solver where the composite material model employed is consistent with experimental measurements [22] for the woven glass-epoxy material. For the solid element model, a total of 1500 elements were used; 6 layers through the 1mm thickness and 300 elements along the 150mm length. For the shell element model, a total of 600 elements along the length in a single layer were used.

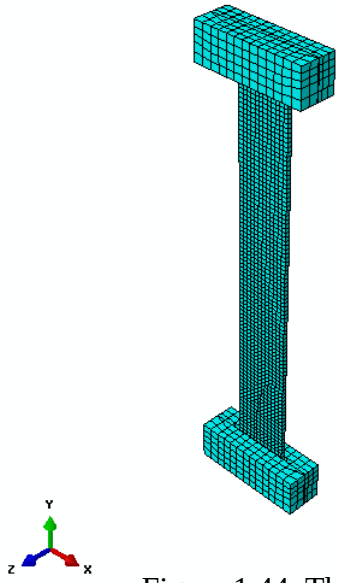

Figure 1.44: The mesh of FE model

Boundary conditions were applied at each end of the specimen that approximated the experimental grip conditions. At one end, all three displacement components along a transverse line at mid-thickness were set to zero and rotation about this line was

[12] An implicit finite element method (FEM) is usually employed for small displacement stress analysis. An iterative solution of this type is not particularly well suited to the large displacement analysis of composite materials, whose post first-ply failure behavior is often highly non-linear.

unrestricted. At the other end, two of the three displacement components along a transverse line that is offset from the centerline by the eccentricity, e, were set to zero. At this end, the axial displacement component (Δ) was specified for this line element and rotation about the line again was unrestricted.[13]

For the same axial displacement $(\Delta = 10\,\text{mm}$ or Δ=20mm$)$, Table 1.4 shows the typical axial strain results at mid-span and mid-width, ε_{xx} (x=L/2, y=0), on both the tension and compression surfaces for $0^o/90^o$ and $-45^o/+45^o$ specimens; strain values shown in Table 1.4 for both FE and Experiments are the average over a 5mm diameter region centrally located across the width of the beam specimen. As shown in Table 1.4, there is very good agreement between the FEM results and the experimental measurements for the two applied axial displacement values.

Table 1.4: Comparison between the DIC and the FEM simulation on the strain on tension and compression side two displacement, i.e. 10 mm and 20 mm.

0^o	Tension side		Compression side	
	DIC Exp.	FEM	DIC Exp.	FEM
10 mm	0.0092526	0.007937	-0.010326	-0.00839
20 mm	0.0147219	0.01294	-0.015405	-0.01359
45^o	Tension side		Compression side	
	DIC Exp.	FEM	DIC Exp.	FEM
10 mm	0.0096017	0.00838	-0.013182	-0.01366

[13] Another approach for assigning boundary conditions is to use the measured (u,v,w) displacement data on both surfaces at positions near the grips with a linear approximation through the thickness. This was used effectively in previous studies by the authors [58]

20 mm	0.0131822	0.01483	-0.019687	-0.02043

The comparison between the experimental and the FEM results of the deflection W versus the axial displacement Δ with shell and solid elements are shown in Figure 1.45. As shown in Table 1.4, a nearly perfect matching between the experiment and the FEM simulation is obtained using solid elements. The deflection prediction using the shell element deviates substantially for $\Delta > 1$mm, so that all further analyses were performed with the solid element mesh.

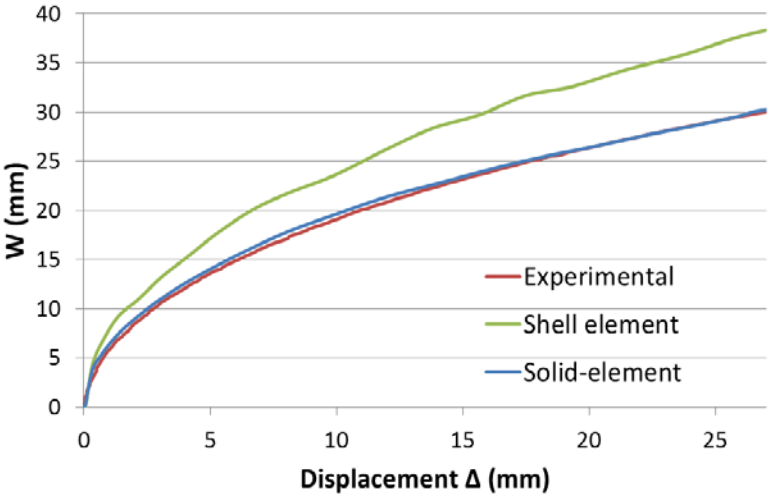

Figure 1.45: Deflection along the longitudinal direction w (mm) versus the displacement x (mm) for the experiments, the shell and the solid finite element.

Figure 1.46 and 1.47 compare experimental measurements and simulation predictions for the effective stress versus the effective strain on the tension surface for $0^o/90^o$ and $-45^o/+45^o$ specimens, respectively. As shown in the two figures, simulation results provide reasonable upper and lower bounds on the measurement results, with the tensile predictions for $0^o/90^o$ specimen providing an upper bound and tensile predictions for $-45^o/+45^o$ providing a reasonable lower bound. Regarding these comparisons, it is important to remember that;

- Woven specimen structure is not considered in the FE models

- Damage is not considered in the FE models

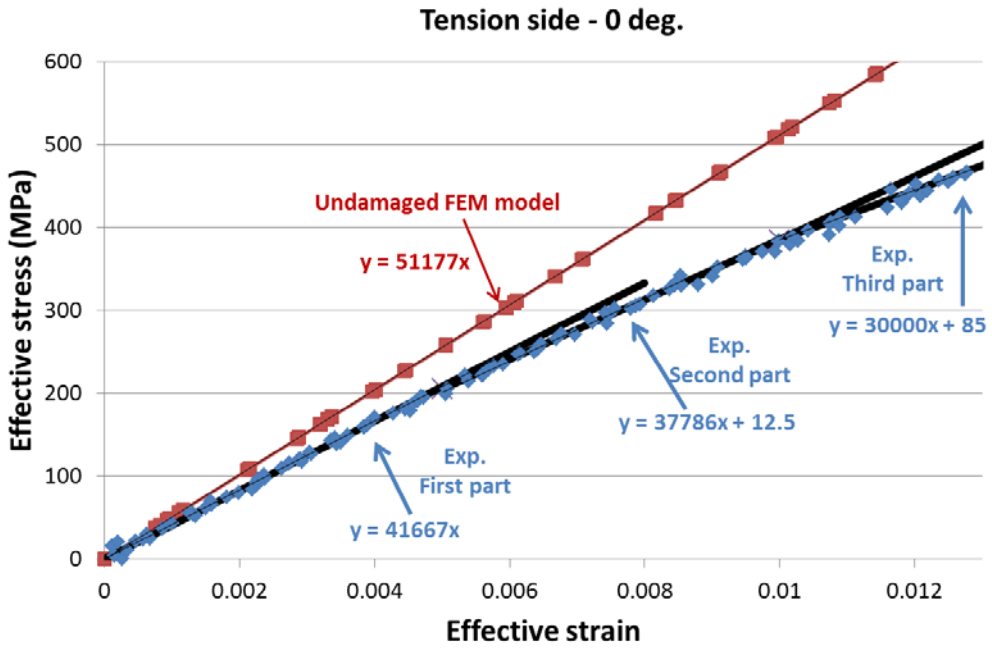

Figure 1.46: Effective stress versus the effective strain on the tension side for 0 degree fiber orientation.

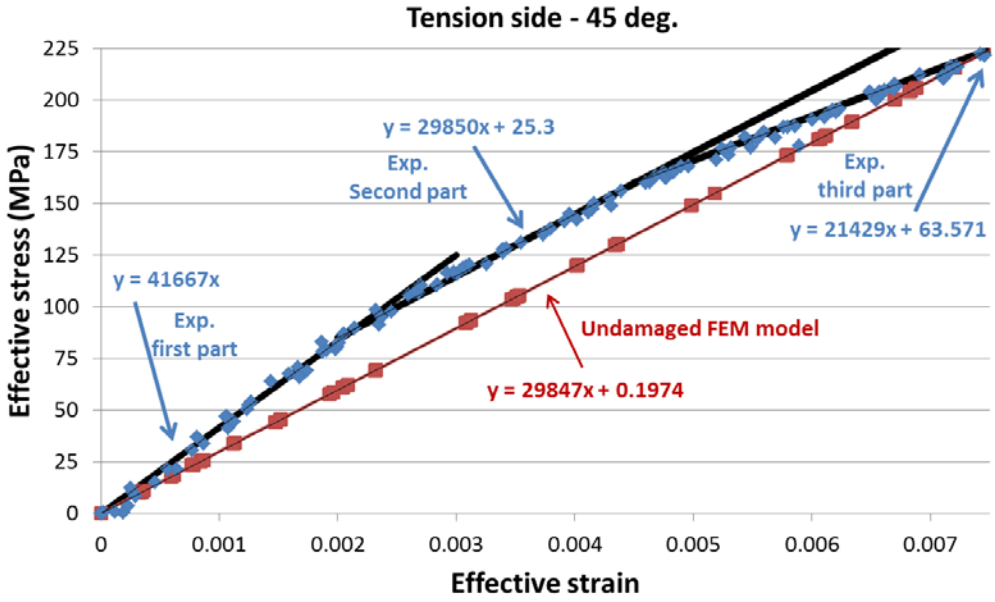

Figure 1.47: Effective stress versus the effective strain on the tension side for 0 degree fiber orientation.

It is also noted that, for both fiber angles, there is reasonably good agreement between simulation results and the experimental data for an effective strain less than

0.003. Since these two cases provide the extremes, one could logically conclude that there is acceptable agreement for all fiber angles in this regime.

In addition to the simulation-experiment comparison, it is relevant to study the experimental data in more detail. Figures 46 and 47 indicate that we can identify three linear regimes in the specimen response. In the 1st stage, it is conjectured that the specimen undergoes limited damage and fiber reorientation. This regime extends from $0 \leq \varepsilon_{eff} < 0.005$ for $0^o/90^o$ specimen and $0 \leq \varepsilon_{eff} < 0.002$-$0.003$ for the $-45^o/+45^o$ specimen. It is conjectured that the $-45^o/+45^o$ specimen behaves the same as the $0^o/90^o$ due to the presence of a woven laminate structure. Of course, this trend is not visible in the FEM simulation because the woven nature of the structure is not modeled.

For the $-45^o/+45^o$ specimen, the 2nd stage from $0.003 < \varepsilon_{eff} < 0.05$ response appears to be a combination of damage and fiber rotation, leading to the behavior shown. In fact, the experimental response is parallel to the simulation prediction, indicating that the woven laminate is behaving as an unwoven $-45^o/+45^o$ laminate. For the $0^o/90^o$ specimen, there is only a slight difference in response in the 2nd and 3rd stages, suggesting that for $0.005 < \varepsilon_{eff} < 0.01$ there is a combination of micro-crack accumulation and eventually crack/damage propagation. Finally, for the 3rd stage in the $-45^o/+45^o$ specimen, there is a clear indication that damage is accumulating as the internal fiber structure reaches maximum fiber rotation in the woven geometric structure, with the onset of further micro-cracking and propagation as this occurs.

1.7 Conclusion

A series of large deflection bending-compression experiments and model predictions have been performed on a woven glass-epoxy composite material to improve our understanding of the specimen response.

A combined specimen-fixture-mechanical loading system has been (a) developed with an integrated 3D-DIC measurement system, (b) used successfully to obtain the full-field deformation measurement for both tension side and compression surfaces of a small woven composite specimen undergoing combined compression-bending loading and large deformation and (c) used to study the nonlinear behavior of a woven glass/epoxy laminate undergoing compression-bending loading.

Experimental results for specimens undergoing both linear and highly non-linear deformations during monotonic loading clearly show the strong relationship of fiber angle to the global response variables, P-Δ and M_{max}-Δ. The critical strain concentration region on the compression bending specimen has been investigated for all fiber angles. The strain results show that the axial strain ε_{xx} along the longitudinal and transverse directions are generally non-uniform and a strong function of fiber angle. Similar results were measured for both the transverse strain ε_{yy} and shear strain ε_{xy}. The presence of anticlastic curvature in the specimens is clearly shown in Figures 18 and 19, reaching a maximum approaching 40% of the specimen thickness at mid-span for $+45^o/-45^o$ specimens. Furthermore, there is a 1-1 correspondence between increasing anticlastic curvature and increasing negative transverse strain, ε_{yy}, at mid-span, confirming the expected coupling between the in-plane strain field and the corresponding curvature component.

Using both Euler–Bernoulli beam theory for small deformations and a modified Drucker's equation for large displacement applications, direct comparisons of experimental and model predictions have been presented. Especially, the modified Drucker's equation effectively extends the theory prediction to the large deformation region, providing an accurate estimate for (a) the buckling load, (b) the post-buckling axial load-axial displacement response of the specimen, (c) the axial strain along the beam centerline, (d) axial strain at mid-span as a function of local applied moment and far-field axial displacement Δ. The modified Drucker formulation prediction of axial strain at mid-span in the $+0^o/90^o$ specimen is in excellent agreement with the tensile and compressive surface measurements over a specific range in the local moment ($M < 0.2$N-m). Beyond this point, the tensile surface data deviates slightly from the model predictions, whereas the actual compressive strains deviate further from the model. The results are consistent with physical observations which clearly showed (a) limited matrix cracking on the tensile surface, and (b) micro-buckling on the compression side that resulted in higher local strains than would be predicted by the undamaged model.

As shown in Figs 42 and 43, there appears to be a nearly 1-1 correlation between effective stress and effective strain for strain values < 0.005. Since damage has been observed in this material for much lower levels of strain, the results suggest there may be the potential to employ these observations in an appropriate damage prediction methodology. Thus, this is one of the most important observations in the paper. By employing concepts developed by other authors including CT Sun [7] and KW Reifsnider et al [19-21], the authors have shown for the first time that there exists a range of deformations where the measured effective stress-effective strain response of the

composite material coalesces into a single master curve for both tensile and compressive loading regimes. Here, the definition of effective quantities essentially attempts to "normalize" the response through use of a function that represents the effect of the fibers oriented at different angles. In principle, such an approach should work well as long as the primary failure mode is matrix cracking with minimal change in fiber orientation or damage. When fiber effects become more important, then the normalization used in the definition may not account for the differences in deformation, and this is confirmed by the slow deviation of the response with fiber angle on both the tensile and compression surfaces of the beam specimen.

Finite element analysis also has been used to further investigate the behavior of woven GFRP under combined bending-compressive. Concerning the nonlinearity expected in these experiments, the result presents a finite element model capable of estimating the large deformations (e.g., axial, transverse) induced by the combined bending-compression loading. The FE model shows the effectiveness in predicting the response of laminated composite beams with different fiber orientation angles, and further explore the applicability of σ_{eff} - ε_{eff} concepts for characterizing both the compression and tensile response

.

CHAPTER 2

SEM-DIC Based Nanoscale Thermal Deformation Studies of Heterogeneous Material

2.1 Introduction

Current developments in science and engineering have led to increasing demand to fabricate and control materials structures on the scale of micro/nanometers, and have brought a significant increase in need for quantitative measurements of material behavior on the micro/nanometer scale. In particular, modern electronic packaging and micro-devices are being manufactured with heterogeneities and reduced spatial size, requiring detailed understanding of the true response of these heterogeneous material systems on the micro/nano-scale under controlled thermal, mechanical and hygroscopic environmental condition. However, measurements on microstructural scales have serious challenges [60] which require specific tools and methods.

Aside from the widely used strain gauge technique, which is pointwise and hard to decrease its physical size to satisfy the micro/nanometer scale, various full-field non-contact optical methods [61] have been developed and applied for this purpose. Interferometric techniques, including holography interferometry, speckle interferometry and moir´e interferometry have been used in specific cases. For example, Kujawinska [62] introduced the general concept of an optical measurement station with optical microscope and interferometry technique. He used a cross-type diffraction grating with 1200 lines/mm to measure the in-plane displacements on a two-phase steel polycrystalline material after plastic. A drawback of interferometric metrologies is that they oftentimes

have stringent requirements under experimental conditions, such as the need for a coherent light source. Thus, the measurements are normally conducted using a vibration isolated optical platform. The resultant measurements are oftentimes presented in the form of fringe patterns which require fringe processing and phase analysis techniques [63]. Another type of measurement method is known as non-interferometric. These include grid methods [64, 65] and digital image correlation (DIC) [66-74].

As a representative non-interferometric optical technique, the DIC method has been well established and widely used as a powerful and flexible tool for the deformation measurement in experimental mechanics. Its full-field capabilities and non-contacting approach are especially advantageous to provide both qualitative and quantitative information of the specimen's deformation response. It requires simple experimental setup and specimen preparation with low requirements in measurement environment, which can easily be applied to different kinds of areas. In addition, the DIC technique has no inherent length scale, and thus it covers a wide range of measurement sensitivity and resolution, from the macroscopic [75] to micro- or even nano-scale [76-79]. In previous studies, the method has been employed using various high spatial resolution digital image acquisition devices, including optical microscopy [80–82], laser scanning confocal microscope (LSCM) [83, 84], scanning electron microscopy (SEM) [85–94], atomic force microscopy (AFM) [95–105] and scanning tunneling microscope (STM) [106–108]. DIC combined with a high-spatial-resolution imaging device (especially, SEM and AFM) is the most effective and flexible tool for observing and quantitatively measuring microscale deformation at reduced size.

For the application of digital image correlation for full-field deformation measurements, the random pattern must be appropriately sized (e.g., 5x5 pixels^2 in area per speckle) and have good contrast for the size of the region of interest. However, generating a surface pattern of speckles suitable for DIC at the micro- and nano-scale that are achievable using an SEM or AFM is challenging. Because the speckle size requirement is well below the capabilities of patterning methods commonly used for DIC at larger scales, such as airbrushing and toner powder [109], a variety of patterning methods have been developed. Existing methods include nanoparticle (NP) techniques [110,111], chemical vapor thin film rearrangement [112] and patterning of polymeric substrates through the use of a contact lithography method [113]. Patterning techniques have continued to evolve with recent additions including thin film ablation [114], photolithography [109, 112] and electron-beam lithography [115,116]. Most of them are elaborate, expensive, time consuming or can only produce the pattern over small areas of the test sample. Kammers and Daly [117,118] recently developed a self-assembled gold nanoparticle (AuNP) patterning technique that eliminated many of the limitations inherent to other methods. By employing their approach, the author has shown that high quality, nanoscale patterns can be deposited on the whole surface of specimen.

Due to the nature of white light, optical imaging methods are limited to a maximum resolution on the order of the wavelength of light (about 1 μm) as the smallest length unit. To access smaller scale of measurements, imaging systems based on an SEM have been developed and improved by many researchers [85–94]. One critical issue encountered in using SEM systems is that the imaging principle is quite different from traditional optical microscopy, and thus a new model and calibration process are necessary. Figure 2.1

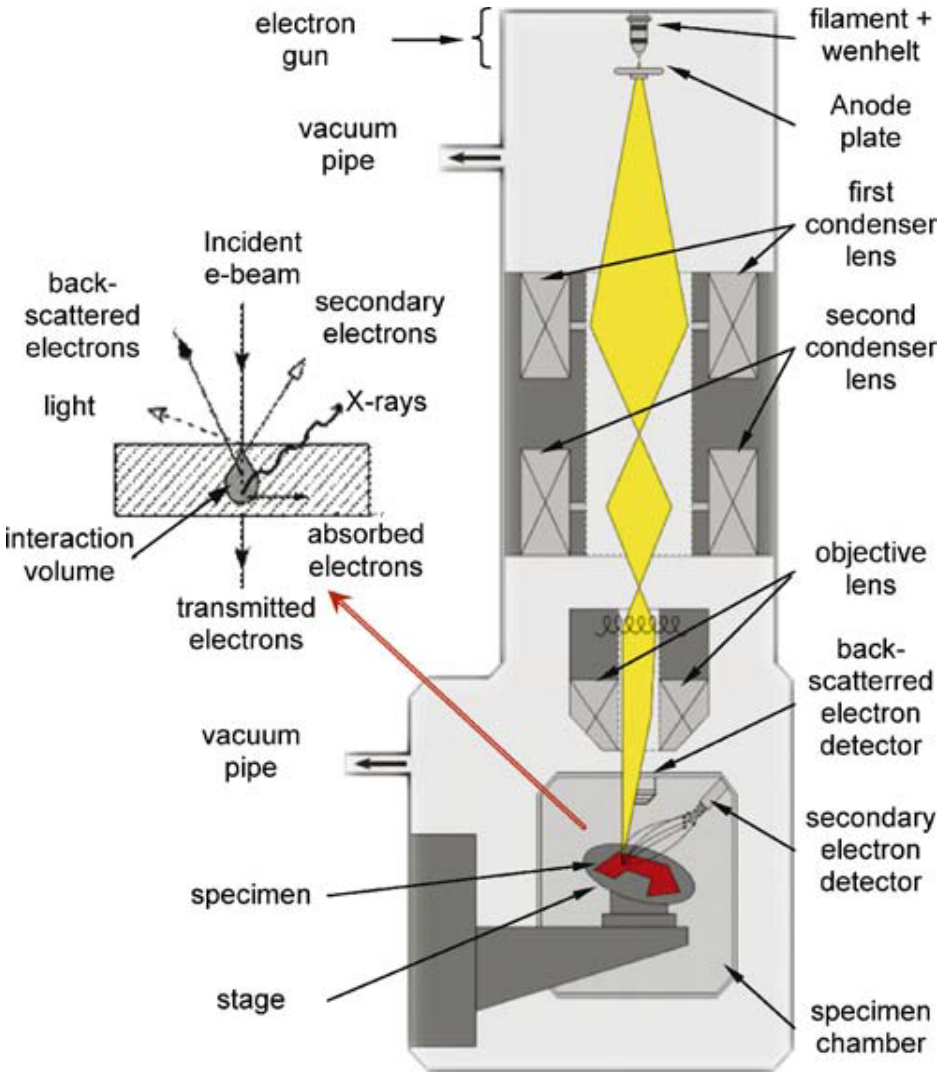

Figure 2.1 Schematic of a typical scanning electron microscope and imaging process

presents a schematic of a typical SEM system. After e-beam generation in a thermal emission gun (TEG) or field emission gun (FEG), the electron beam passes through a series of electromagnets and is focused onto the specimen surface. Radiation is emitted when the electrons interact with the atomic structure of specimen. A digital representation of the specimen's emitted radiation is produced using a raster-scan process and a photon collector; typical photon collectors are the Secondary Electron Detector (SED) and the Back Scattered Electron Detector (BSED). Since the e-beam position is open loop controlled in a typical modern SEM system, the rastering process will cause positional

errors in the scanning process due to environmental and system variations [119], such as electromagnetic field fluctuations, beam positioning spatial distortion, time-dependent drift (most of time associated with charging of the specimen) [120], and mechanical vibrations. Most papers employing SEM imaging, and even commercial SEM measurement system manufacturers, simply ignore these effects and consider a pure projection model [121–126]. Though a few authors do take into account distortion (considering parametric distortion models [127–129]), the effect of drift distortion is generally not considered in experimental studies [130]. This situation was changed when Sutton et al [92-94] developed a new method for accurate measurement of deformations in an SEM at reduced length scales based on their previous work of bundle adjustment method [131] for distortion correction of a general imaging system for use with DIC. The paradigm shift that ensued led Li [132] in his work to show conclusively that higher magnification levels could be handled experimentally with the new approach, provided that a robust and accurate translation sequence was performed during calibration to increase the overall accuracy of the corrections.

Although there have been many experimental studies and application of SEM-DIC, much of the previous work has focused on mechanical loading, with a limited number of recent studies focusing on thermal effects in nominally homogeneous material systems [116,132]. Since thermal reliability is a key issue for the development and design of advanced electronics and micron/nano scale packages, which are inherently heterogeneous in nature, the author applied the SEM-DIC measurement method to quantify the response of small portions of IC packages (areas from 50x50 μm2 to 10x10 μm2) when subjected to thermal loading conditions from RT to ≈250 ^{o}C. Details

regarding the heterogeneous electronic packages specimens used in this study, along with a discussion of the patterning methods employed, are presented in Section II. Section III shows the experimental system setup. Section IV discusses the distortion correction procedure, with an extended discussion of the results after calibration. Results from several preliminary thermal tests on metallic sample are shown to verify the methodology. In Section V, thermal test results on IC package are highlighted, which shows the evolution of deformations around flaws and across the complex material constituents as the temperature increases up to $\approx 250\,^{o}C$.

2.2 Specimen Characteristics

The present work is conducted on heterogeneous electronic packages containing silicon (Si), copper (Cu) bumps, a polymer rich Wafer Photo-Resist (WPR) layer, solder, backing material/composite substrate and/or First level interconnect (FLI). Figure 2.2 shows the cross-sectional surface of one specimen. The regions enclosed by the blue line contain various materials that have different elastic moduli and thermal expansion coefficients. These regions are the AOI for this specimen.

All specimens were cut by an IsoMet low speed precision sectioning diamond saw to 20mm in length and 10mm in height to fit a specially designed aluminum holder. Several different polishing methods has been tried in order to get required surface roughness, including: 1) Use grinding/polishing equipment in the USC EM (Electron Microscopy) Center, including the MultiPrep™ System from Allied High Tech Products, Inc.; 2) Send the specimen to the North Carolina Nanocenter to use their FIB (Focused Ion Beam) and perform surface milling within the AIF (Analytical Instrumentation Facility at NCSU);

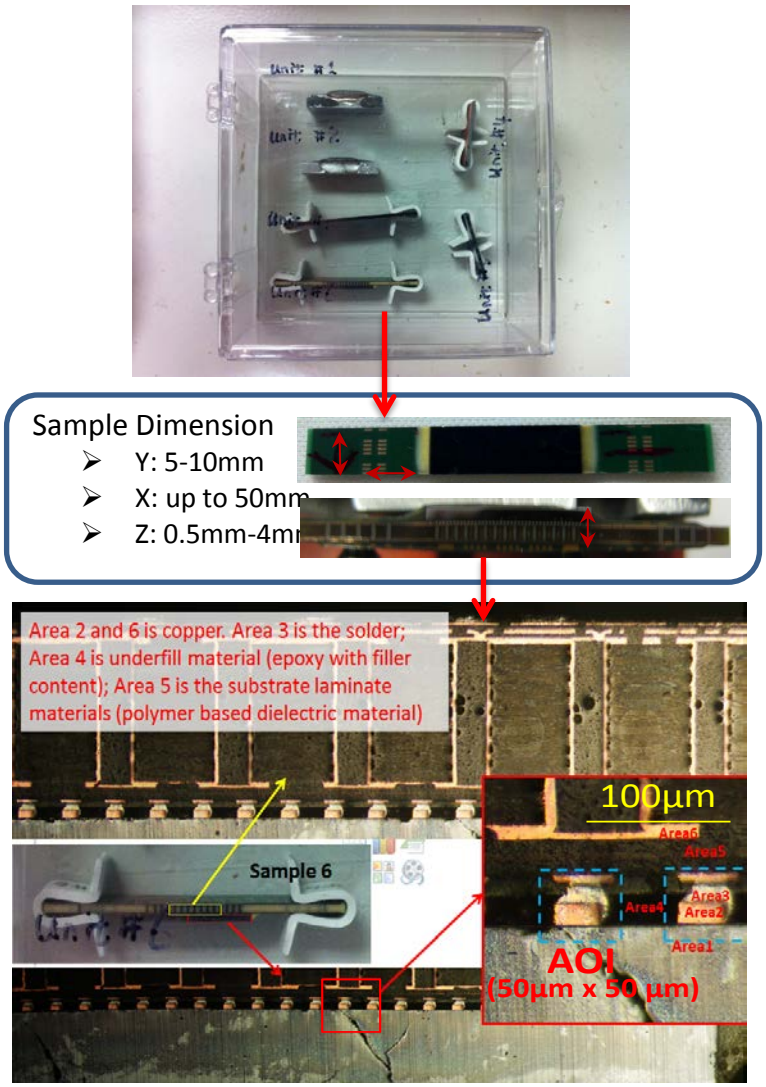

Figure 2.2: Specimen surface and area of interest of one specimen

3) Send a sample to University of Michigan; 4) Apply metallographic standard polishing procedures - the top surface of the specimen (which corresponds to a transverse cross-section of the integrated chip (IC) package) initially is mechanically polished with 120~800 sand paper using deionized (DI) water. After completing the initial polish, a refined polish with abrasive powders such as AlO_2 (5micro, 3micron) was performed. Finally, an abrasive mixture containing 20nm colloidal silica (liquid) was used to obtain a reasonably flat surface on the heterogeneous material system. Unfortunately, none of these approaches were successful.

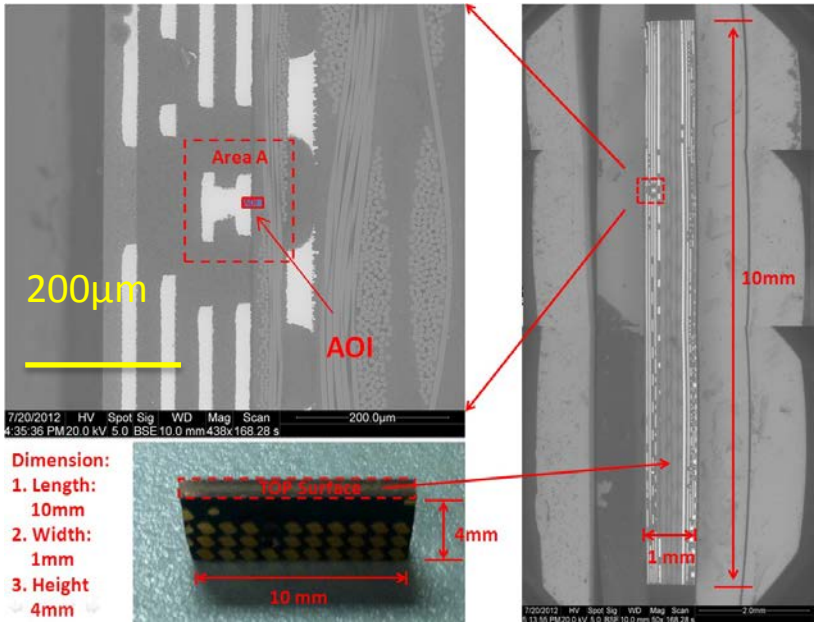

Figure 2.3: Cross sectional surface of one specimen

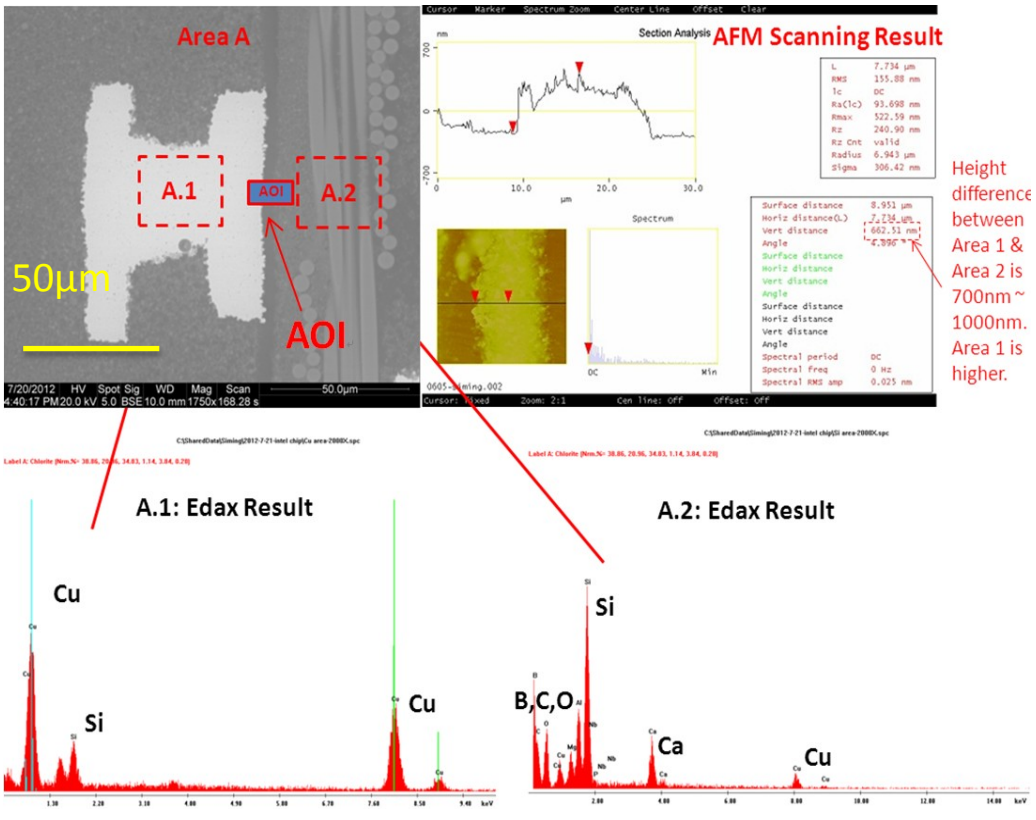

Figure 2.4: AFM and Edax scanning results

2.3 Surface Patterning Study

Figure 2.3 is cross sectional surface of one specimen. According to the EDAX scanning results in Figure 2.4, the AOI included both a copper feature (bright area in SEM image) and a polymer based substrate (gray area). It is noted that results from AFM scanning of the as-polished chip profile shows the surface roughness is about 700 ~ 1000 nm, with relatively steep spatial gradients near boundaries where high modulus differences occur (e.g., copper-polymer interfaces) that resulted in differential surface removal during polishing. These gradients invalidated the use of E-beam lithography for random patterning since the local profile gradients severely affected the quality of the pattern in the interface region where data is most needed. Figure 2.5 shows a trial E-beam lithography patterning result, where the pattern was not visible at all. Fortunately,

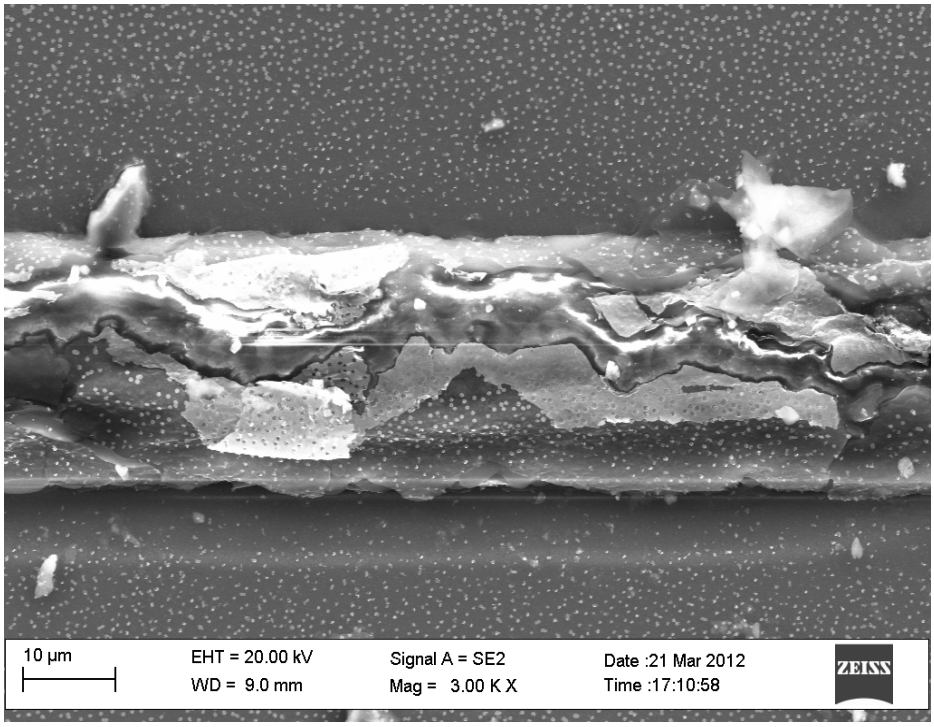

Figure 2.5: E-beam lithography failed to pattern the area near the material boundary

Kammers and Daly [117,118] recently developed a novel self-assembled gold nanoparticle (AuNP) DIC patterning technique that eliminated the need for lithographic methods. By employing this method, the authors have shown that high quality, nanoscale patterns can be deposited on polished heterogeneous material systems such as shown in Figure 2.5.

In their work, Kammers and Daly employed the method for patterning aluminum specimens. As they noted, the gold nanoparticles (AuNPs) are obtained through a reaction between $HAuCL_4$ and Na_3-citrate, with the particle size and distribution density controlled by the proportion of the mixture. In our experiments, one part of 38.8mM Na_3-citrate to 20 part of 1mM $HAuCL_4$, was chosen to obtain AuNPs with the appropriate size and spatial distribution. AuNPs were produced following the procedure as follows: Gold (III) chloride trihydrate (HAuCl4·3H2O) and trisodium citrate dihydrate (C6H5Na3O7·2H2O) purchased from Sigma Aldrich were used to make stock solutions of 10 mM HAuCl4 and 38.8 mM Na3-citrate. To synthesize the AuNPs, 400 mL of 1mM HAuCl4 (diluted from 10mM stock solution) was added to a beaker and brought to a boil while stirred with a magnetic stirring rod. Between 4.5 and 30mL of 38.8 mM Na3-citrate was then added to the boiling solution to produce AuNPs with diameters of 10 to 100 nm. Dispersions of discrete gold nanoparticles via colloidal suspension in transparent media provide different colors. The diameter of gold nanoparticles determines the wavelengths of light absorbed. The colors in the bottles shown in Figure 2.6 illustrate this effect. After synthesis, the AuNPs were stored in dark glass bottles until use to protect them from UV rays that would reduce any remaining HAuCl4.

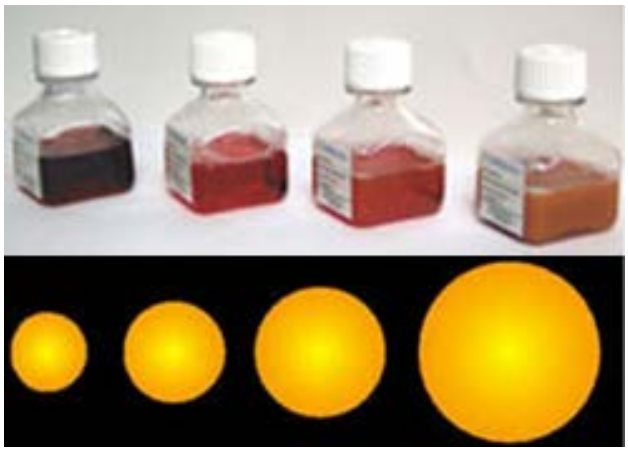

Figure 2.6: Light colored mixture corresponds to larger gold particles

The AuNPs attach to the substrate surface by organosilane molecules that possess a pendant functional group with a strong affinity for gold. When substrates that possess reactive oxide/hydroxyl groups on their surface are immersed in a dilute organosilane solution, the silane molecules covalently bond to the substrate surface. The bound molecules are oriented so that the pendant functional group extends from the substrate surface, causing AuNPs to self-assemble onto the surface upon immersion into the AuNP solution. In this work, the (3-mercaptopropyl) methyldimethoxysilane (MPMDMS) (Sigma-Aldrich) were used.

Different from the 99.99% Al substrates that Kammers and Daly used in their experiments, the IC package contains multiple materials with varying properties. Preliminary studies indicated that differential chemical reactions occurred when exposing the surface to the patterning mixture, resulting in poor spatial distribution of particles as unbonded silane molecules detached from the substrate surface and in some cases, corrosion/erosion of the underlying material occurred during the patterning process (Figure 2.7). To overcome this difficulty, the authors coated the surface with a thin layer of titanium. In this work, results are presented when using a 40nm titanium layer. It is

noted that a side benefit of the coating process was the minimization of “specimen charging”, which is induced by the presence of low electrical conductivity materials on the surface of the specimen when scanned by the electron beam during SEM imaging.

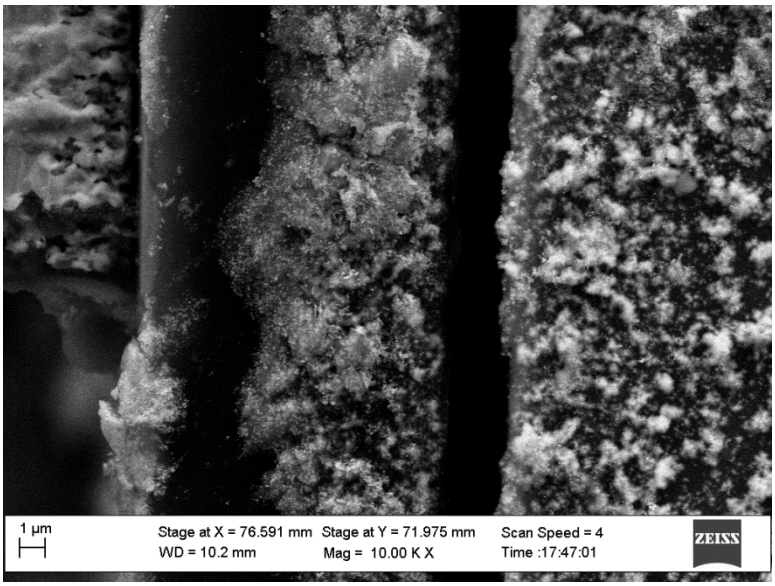

Figure 2.7: Corrosion/erosion of the underlying material occurred during the patterning process

Though described in detail in Reference [118], a brief description of the patterning process for this study is present. After lightly polishing the surface and applying the thin layer of titanium to the outer surface of the entire chip specimen, the surface region of interest on the IC chip is immersed in boiling deionized water to hydroxylate the specimen surface for pattern application. The substrate surface was silanized by soaking the surface in vials filled with one part MPMDMS to four parts methanol for 24 hours. After removal, the substrate surface was immediately immersed in 100mL methanol, and rinsed for 30 minutes using a magnetic stirrer. Following the methanol rinse, the surface was again rinsed with deionized water and then the IC specimen was placed in a vial for one day that contains the mixture 38.8mM Na_3-citrate to 20 part of 1mM $HAuCL_4$. Figure 2.8 shows the 10 KX magnification SEM image of sample surface after

completing the self-assembled gold nanoparticle patterning process. Even though the entire area is coated by titanium, the underlying heterogeneous nature of the surface is clearly visible in the SED SEM image. Here, area 1 is copper, area 2 is solder, area 3 is the WPR under-fill material (epoxy with filler content), area 4 is copper embedded in silicon, and area 5 is silicon. As shown in Figure 2.8, the entire surface has a nearly uniform, high contrast speckle distribution with particle size around 30~60nm, which is appropriate for using DIC to measure accurate local thermal deformations in the various material regions[14].

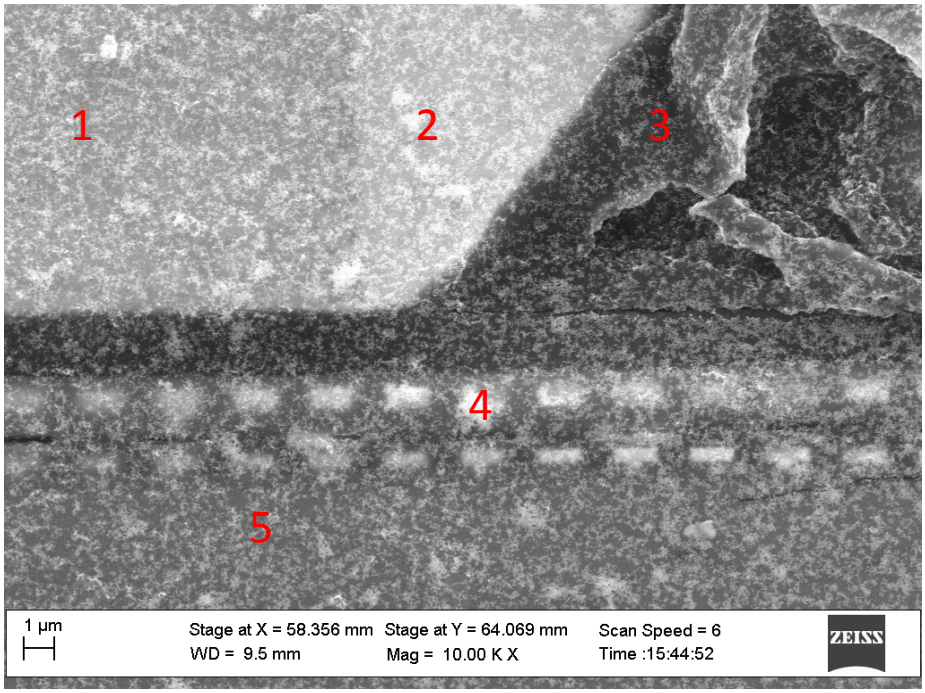

Figure 2.8: Gold speckle pattern on heterogeneous material. Area 1 is copper, Area 2 is solder, Area 3 is under-fill material (epoxy with filler content), Area 4 is copper embedded in silicon, and Area 5 is silicon

[14] Currently, we have successfully applied a speckle pattern with a minimum particle of 5nm on a Si wafer specimen coated with 40 nm of titanium.

2.4 Experiment Setup

The SEM images shown previously were captured with a secondary electron detector to check underlying features of AOI in a Zeiss FEG SEM. In the thermal test, a Back Scatter Electron Detector (BSED) was used instead of secondary electron detector to get uniform contrast and less image distortion. SEM imaging parameters are selected based on overall quality of the image: (a) If contrast is sufficient, lower accelerating voltage is preferred to protect the IC chips from undesirable heating damage. In this work, the accelerating voltage is 5kV; (b) Image size is 1,024×768 pixels; (c) Scanning speed is 6 in Zeiss SEM setting; (d) Line average mode has been used and the averaging number is 6; (f) Total image scan (frame time) to obtain the average of 6 images is 15.6sec; (g) Working distance is around 10mm. Here, longer working distance is used in order to reduce the potential for thermal damage to the BSED due to specimen heating.

Based on the structure and features within each sample, as well as the gold particle size being applied, a magnification on the order of 5000× was used for the first test. In this SEM, 5000X corresponds to ≈ 56nm/pixel. Therefore, the regions being imaged are 57×43 μm at 5000×. In future experiments using this specific speckle size, 20,000× may be preferred to increase the number of pixels sampling each speckle, because as noted in a recent publication [74], oversampling requires that each speckle be sampled by at least 3x3 pixels for optimal accuracy.

The heating plate INSTEC AHP202 were specially designed for thermal stability over the range 0^{o}C to 250^{o}C (which corresponds to 0 to 200^{o}C at the imaged surface of the IC) with demonstrated ability to hold temperature within 0.1°C at 100°C, while

having a slim profile so that it can be used effectively in the Zeiss SEM system. A specially designed PID control strategy was implemented to limit temperature overshoot during incremental heating and thereby reduce the total time required to perform the experiment. In its updated form, the modified thermal stage rapidly approaches and then maintains the set temperature with variability of ±0.1°C. This level of thermal variability introduces strain oscillations in the aluminum specimen of 2.3×10−6 that are negligible in comparison to the effect of the relatively large drift distortion estimates obtained from two consecutive images.

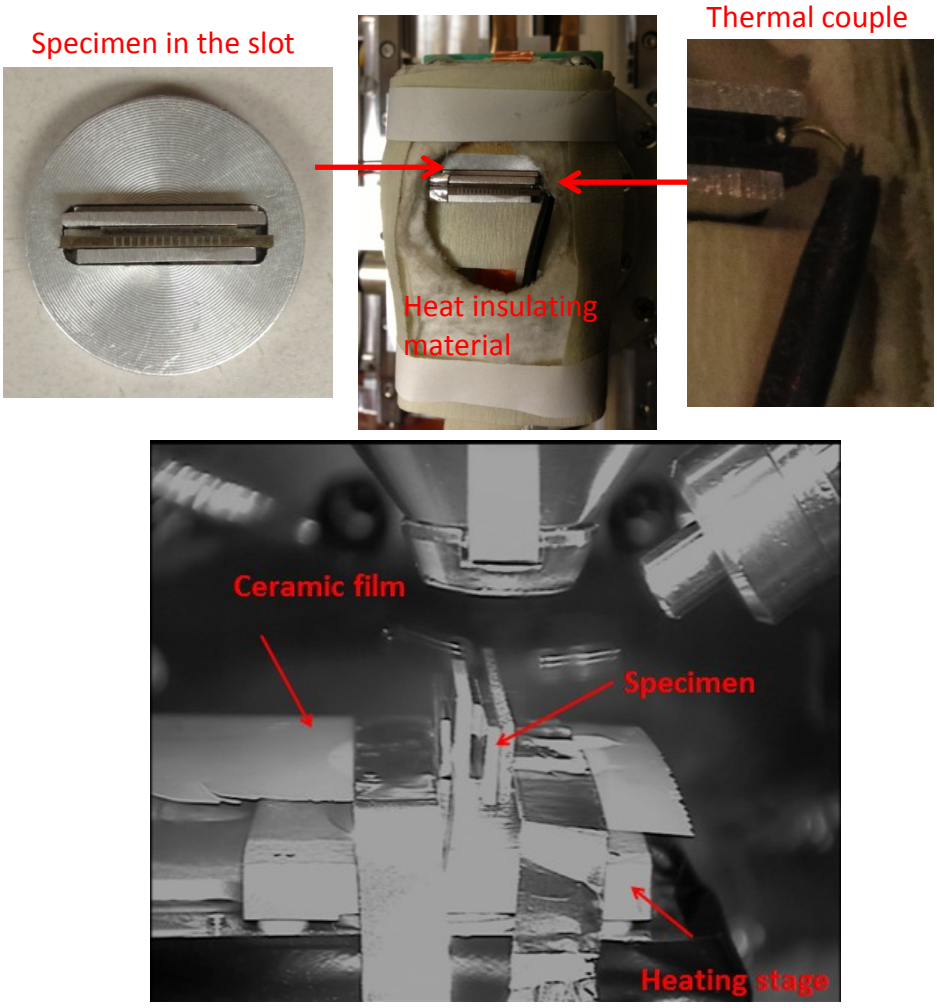

Figure 2.9: Heating plate and specimen configuration

In order to hold the specimen vertically and heat more uniformly, an aluminum holder has been manufactured. The holder is a 28mm diameter round disk with a 5mm deep slot. Another reason the Al holder has been used is that the specimen is composed of relatively low electrical conductivity materials. The metal holder reduces the well-known "specimen charging" issue, which can cause severe imaging drift distortion problems during SEM scanning. Figure 2.9 shows images of the heating plate and specimen configuration. Temperature control was performed using the INSTEC STC200 control system [133]. A digital thermometer with K-Type thermocouple sensor has been modified to use in the test to measure the temperature of the specimen surface. To perform the control process outside the chamber, all wires from the heating plate are routed out of the SEM vacuum chamber through a sealed flange.

Results from our studies show that the temperature a few millimeters above the thermal stage can exceed 130^{o}C in an enclosed environment, which could damage the SEM imaging components. A combination of a Ceramic Fiber Insulation Blanket and a thin ceramic film was used to reduce the temperature to acceptable levels. We performed experiments to show that the method reduces temperature at 10mm above the thermal stage to 60^{o}C.

2.5 SEM Image Distortion Correction

Due to the complexities of high-magnification SEM imaging systems that weaken the normal assumptions for CCD lens systems, the distortions in SEM images cannot be corrected by classical parametric distortion models; use of such simple models could result in inaccurate DIC displacement data. Sutton et al. [92- 94] were the first to

recognize that these distortions existed and need to be corrected prior to displacement and strain calculations. These distortions are characterized in two categories. One is spatial distortion, which is similar to the distortion present in optical lenses and can vary from test to test. The other is drift distortion, which varies over time and pixel drift is not constant within the image (see Figure 2.10). It can lead to significant errors in high spatial resolution experiments. In their work, spatial distortion removal is performed using a methodology that employs a series of in-plane rigid body motions and a generated warping function. Drift distortion removal is performed using multiple, time-spaced images to extract the time-varying relative displacement field throughout the experiment.

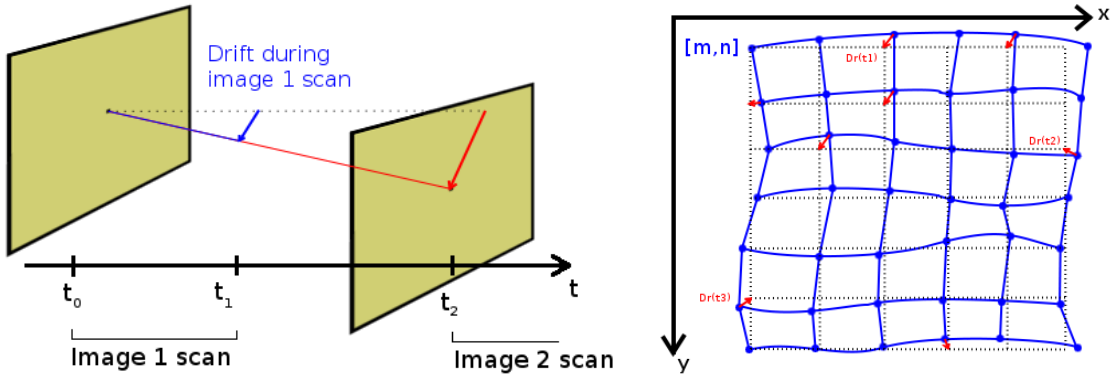

Figure 2.10: Drift Distortion is non-linear and varies over time

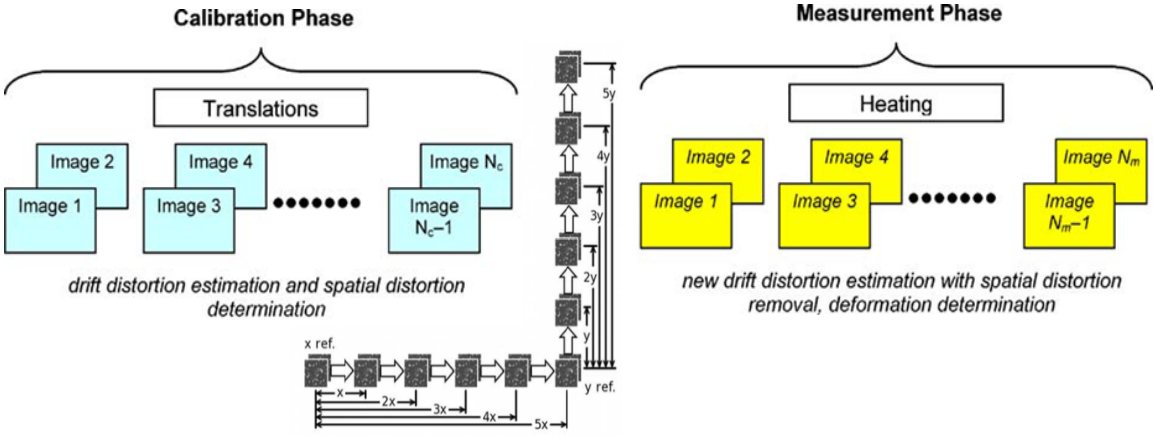

Figure 2.11: Schematic of experimental procedure for distortion removal and specimen heating in an SEM system.

Figure 2.11 shows the schematic of experimental procedure for distortion removal and specimen heating in an SEM system. In order to use VIC-2D[15] which includes experimental functionality to correct for both drift and geometric distortions that occur in SEM images, pairs of images have to be acquired in quick succession and the acquisition time for each image has to be recorded. This applies both to calibration images and images of the test object. There must not be any change in load or position of the object (whether calibration object or test object) between acquisition of the image pairs. Briefly, the procedure can be described as follows.

1) First, obtain the best focus of the image by adjusting SEM parameter settings before the calibration, including working distance, aperture and stigmation.

2) Second, without increasing temperature, all imaging parameters are set for the SEM system and initial images are acquired to ensure that the magnification and focus are adequate.

3) Third, to perform the calibration process and determine the spatial distortion, in-plane rigid body motions are applied. The specimen is translated in two orthogonal directions several times to complete the calibration phase. After each translation, a pair of images is acquired. For the two largest motions relative to the reference image, the motion should be recorded, as it will later have to be entered into the calibration dialog. The largest motions should be approximately 1/20 - 1/10 of the image size and a total of at least 5 motion steps in each of the two axis directions is adequate.

4) Once the translations are complete, the thermal heating experiment is initiated. During the measurement phase, which is simply a continuation of the calibration phase,

[15] Correlated Solutions Incorporated; 121 Dutchman Blvd; Irmo, SC; 29063. www.correlatedsolutions.com

the specimen is heated and undergoes thermal expansion. After each temperature increase has been completed and the temperature is stable, a pair of images is acquired that forms the image set for measurement purposes.

5) Post-processing of images is performed using commercial 2D-DIC software VIC-2D [52] with an a priori distortion correction subroutine to correct and then extract all displacement field data.

Figure 2.12 shows both the uncorrected and corrected displacement field and strain field on an aluminum specimen under 5000x magnification. Figure 2.12 shows that the drift and spatial distortion correction procedures remove most of the imaging errors. After each increment of temperature, two images are acquired and are again used to estimate drift increments.

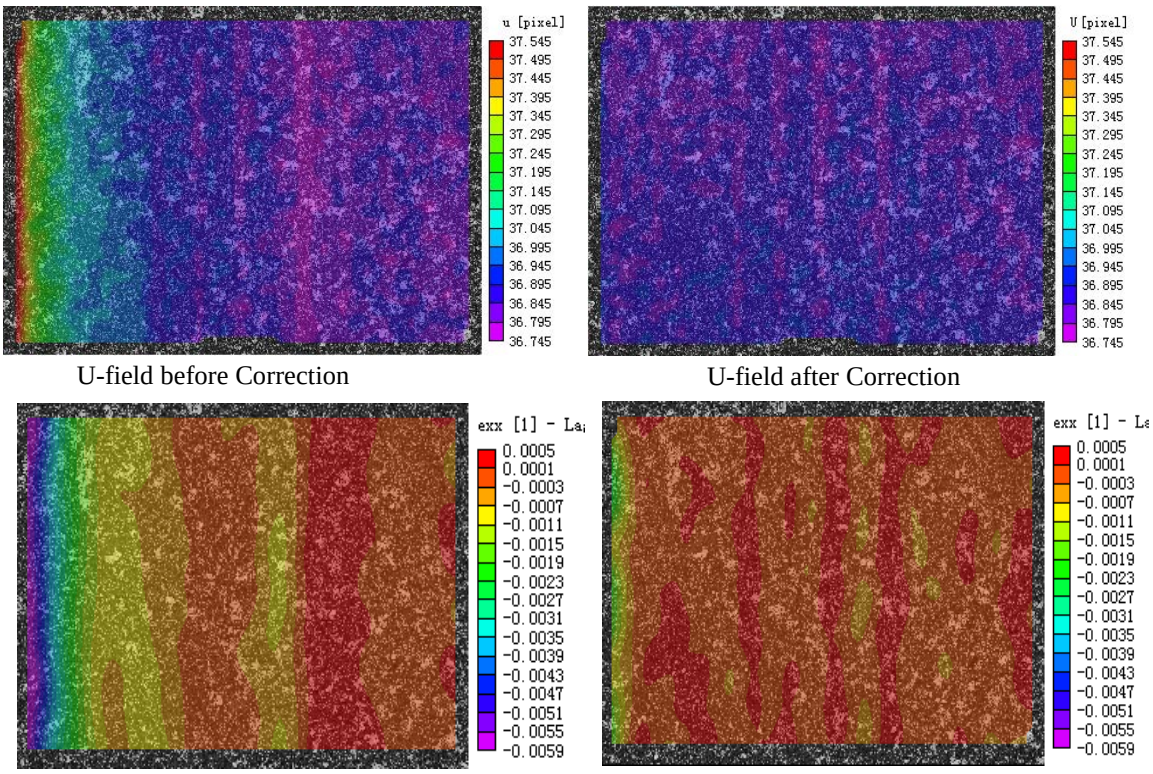

U-field before Correction

U-field after Correction

ε_{xx}-field before Correction

ε_{xx}-field after Correction

Figure 2.12: Uncorrected and corrected displacement fields and strain fields on an aluminum specimen at 5000x magnification.

To determine the drift throughout the entire experiment, digital image correlation is performed on each image pair to extract the incremental drift. The measured incremental drift at each pixel location during the experiment is used to correct all images.

It is noted that there are no changes in SEM parameter settings during an experiment, including working distance, aperture and stigmation after calibration. Our previous work shows that each change in a parameter leads to additional distortion errors in the final DIC results, even though the image itself looks “better” or sharper after an adjustment.

During heating experiments, both the heating plate and the specimen experience thermal expansion. When assuming two-dimensional object motion during the experiment, care must be taken to ensure that the parasitic effects of out-of-plane motions experienced during the heating process do not introduce significant errors in the image-based deformation measurements. In this work, the authors adjusted the position of the specimen via the SEM Z-stage according to the image focus as temperature increases (Figure 2.13), thereby approximately compensating for thermal expansion in the Z-direction (Figure 2.14).

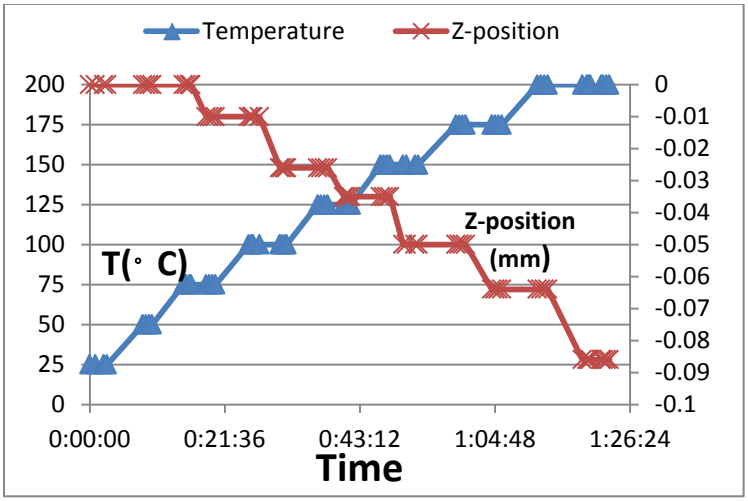

Figure 2.13: Z-stage adjustment with temperature increasing in Aluminum specimen test

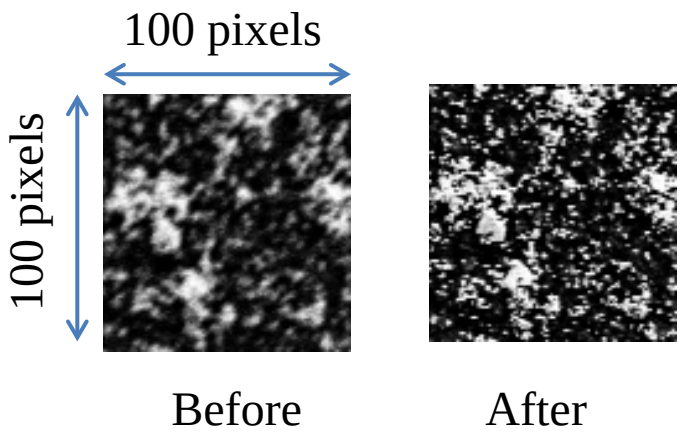

Figure 2.14: Z-stage according to the image focus

2.6 Image Post-processing in Vic-2D

Post-processing of images is performed using commercial 2D-DIC software VIC2D [52] with an a priori distortion correction subroutine to correct and then extract all displacement and strain field data.

First, appropriate subset size and subset spacing should be estimated and input in the ViC-2D before calibration and correlation. Session 7.1 illustrate the best practices for estimating subset size and subset spacing.

2.6.1 Best Practices for Estimating Subset Size and Subset Spacing

To obtain data throughout the region of interest, the reference image is decomposed into subsets and each subset is correlated with deformed images to obtain a discrete set of full-field displacement data. When performing optimal pattern matching between the undeformed and deformed images of a specimen, the most common approach is to select sub-regions on the undeformed specimen that contains several features. The reason for selecting a small sub-region (oftentimes called a subset) is to ensure uniqueness in the matching process.

Guidelines for selecting subset size are as follows.

- When good contrast exists in the image, each subset should contain approximately 6 features in each direction (3 light and 3 dark)
  - If each feature has 3 × 3 pixel sampling, then subsets contain at least 18 × 18 pixels
  - If each feature as 7 × 7 pixel sampling, then subsets contain 42 × 42 pixels
- When contrast is marginal, each subset should contain several more features (e.g. 12 features in each direction) to maintain accuracy in the matching process
  - If each feature is 3 × 3 pixels, then subsets would contain 36 × 36 pixels
  - If each feature has 7 × 7 pixel sampling, then subsets contain 84 × 84 pixels

Regarding the spacing between subset centers, it is recommended that the subsets be separated by at least ½ the subset size. Thus, if an N × N pixel subset has its center at pixel location (P, Q), then the next subset to be correlated would be no closer than (P + Int(N/2), Q), where Int( ) is the integer part of N/2.

2.6.2 Vic-2D Distortion Correction Procedure for SEM images

Drift and spatial distortion corrections are performed using images from both the calibration and measurement phase of the experiment. Results from this process are used to define a warping function that can be applied to all images in the experiment.

To use the correction in Vic-2D, a text file listing image file names and their acquisition times has to be created. This is a simple, comma separated file of strings and times, for example:

"img_00.tif" , "00:00:00"

"img_01.tif " , "00:01:40"

"img_02.tif " , "00:03:20"

"img_03.tif " , "00:05:00"

"img_04.tif " , "00:06:40"

"img_05.tif " , "00:08:20"

"img_06.tif " , "00:10:00"

"img_07.tif " , "00:11:40"

The image sequence can be imported into Vic-2D using Project->Speckle image list. First, the image sequence with the calibration images should be loaded. Select an AOI that fills the entire image, and choose an appropriate subset size for the pattern. Then, analyze the image data, and check “Process as SEM sequence” on the analysis dialog and enter the values for dwell and row time. After processing is complete, click Calibration->Distortion Correction. Select the two images with the largest motions, and enter the motions in the x and y directions and select the unit (mm/microns etc). After the distortion correction analysis, Vic-2D will now have a calibration.

To check how well the distortion removal worked, analyze the data again. The analysis dialog will retain the settings for SEM analysis. Since there is now a calibration, Vic-2D will generate metric values for coordinates and displacements. When analyzing the calibration image sequence, all displacements should be uniform. After verifying the calibration, Vic-2D can now be used to analyze image sequences of the specimen (again, use Project->Speckle image list to import the file sequence and timing information)

Drift distortion correction is performed using images from both the calibration and measurement phase of the experiment. Spatial distortion estimation is performed using only the drift-corrected images from the calibration phase. Results from this

process are used to define a warping function that can be applied to all images in the experiment (both calibration and measurement images). After all corrections are performed, a fully corrected set of displacement field data is obtained for both calibration and measurement phases of the experiment. These displacement fields are used to extract full-field strain data.

2.6.3 Extract displacement and strain field

After all corrections are performed, a fully corrected set of displacement field data is obtained for both calibration and measurement phases of the experiment. These displacement fields are used to extract full-field strain data.

2.7 Thermal Validation Experiment: Metallic Specimen

To verify the complete process works well and is effective for quantifying thermal deformations at high magnification, several different specimens, including aluminum, nickel and brass, have been chosen to compare the experimental result to literature values for the thermal expansion coefficient. Figure 2.15 shows the specimens with a high contrast random pattern on the surface.

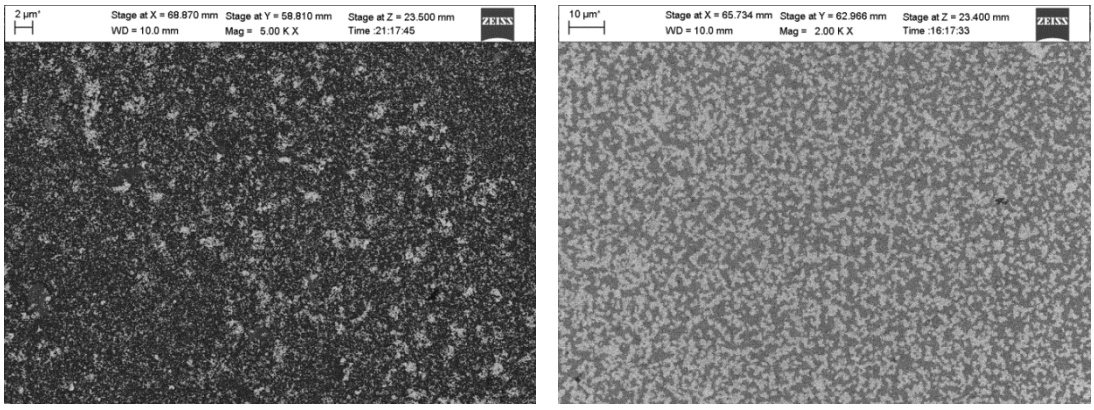

Figure 2.15: Left: Al specimen imaged at 5000x magnification. Right: Nickel specimen imaged at 2000x magnification

Figures 2.16~2.18 present the measured average thermal strain fields for ε_{xx}, ε_{yy} and ε_{xy} (blue dots), as well as estimated thermal strain using literature data (red line), during the heating process. The data in Table 2.1 shows that all experiments thermal expansion coefficients are in good agreement with existing literature values [134], which confirms the effectiveness of new patterning method and accuracy of the methodology for thermal measurements in an SEM.

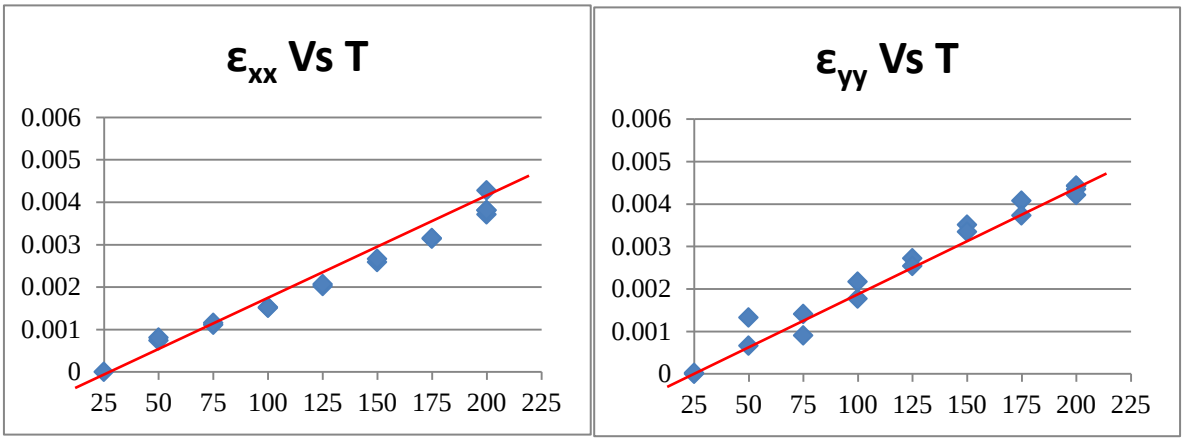

Figure 2.16: Thermal strain vs temperature for Aluminum

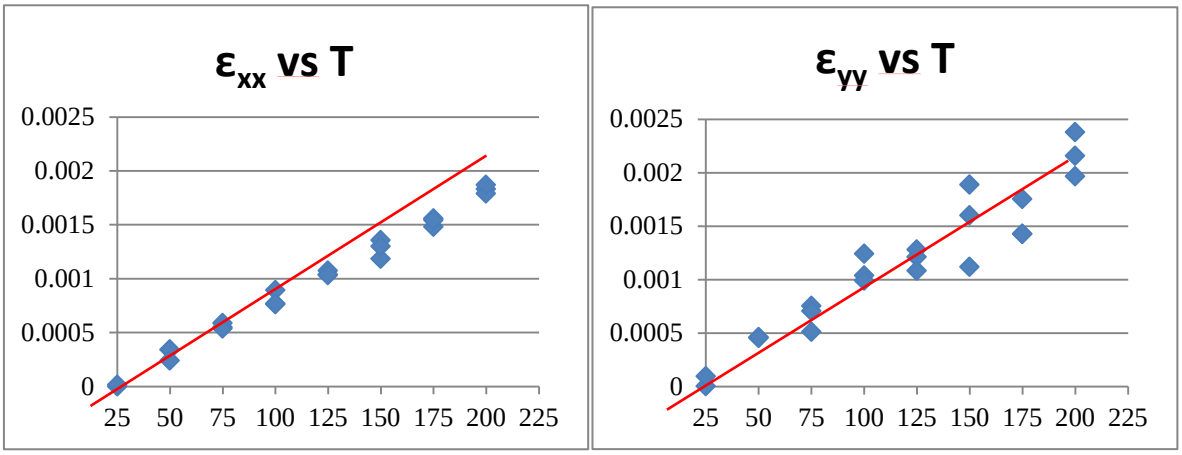

Figure 2.17: Thermal strain vs. temperature for Nickel

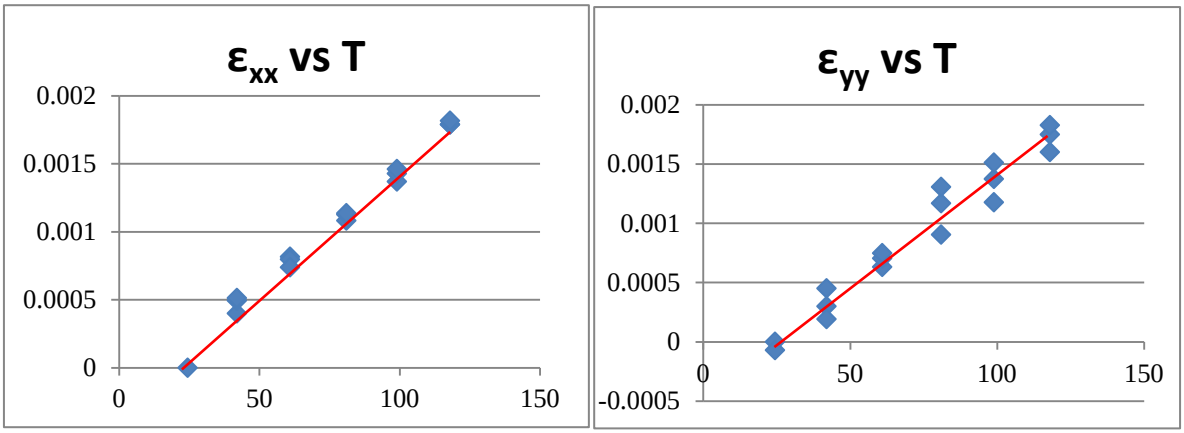

Figure 2.18: Thermal strain vs. temperature for Brass

Table 2.1: Experiments thermal expansion coefficients comparing to literature values

	Literature value	ε_{xx}	ε_{yy}
	$(10^{-6}/°C)$	$(10^{-6}/°C)$	$(10^{-6}/°C)$
Al	23.1	21.4 ± 0.7	24.3 ± 1.0
Ni	13.0	10.9 ± 0.3	13.0 ± 0.8
Brass	19	18.3	18.7

2.8 Thermal Test Results on Cross-section of an IC Package

The validation test for a metallic specimen demonstrates that the complete process is effective for quantifying thermal deformations at high magnification, which gives us the confidence to perform the experiments on real IC packages. Figure 2.19 a~d shows one specimen and the location of area of interest used in these experiments. According to the EDX scanning results, (a) Areas 1 and 2, 5 and 6 in Figure 2.19 are substrate laminate materials (polymer based dielectric material), (b) Area 3 is a copper bump and (c) Area 4 is a mixture of copper and polymer. Nonhomogeneous thermal deformation is expected in this heterogeneous specimen. Secondary electron detector image (Figure 2.19c) was used to detect the shape of each feature before the test. In the calibration and thermal test procedure, Back Scatter Electron Detector (BSED) was used instead of secondary electron detector to obtain uniform contrast and reduce image distortion (Figure 2.19 e-f).

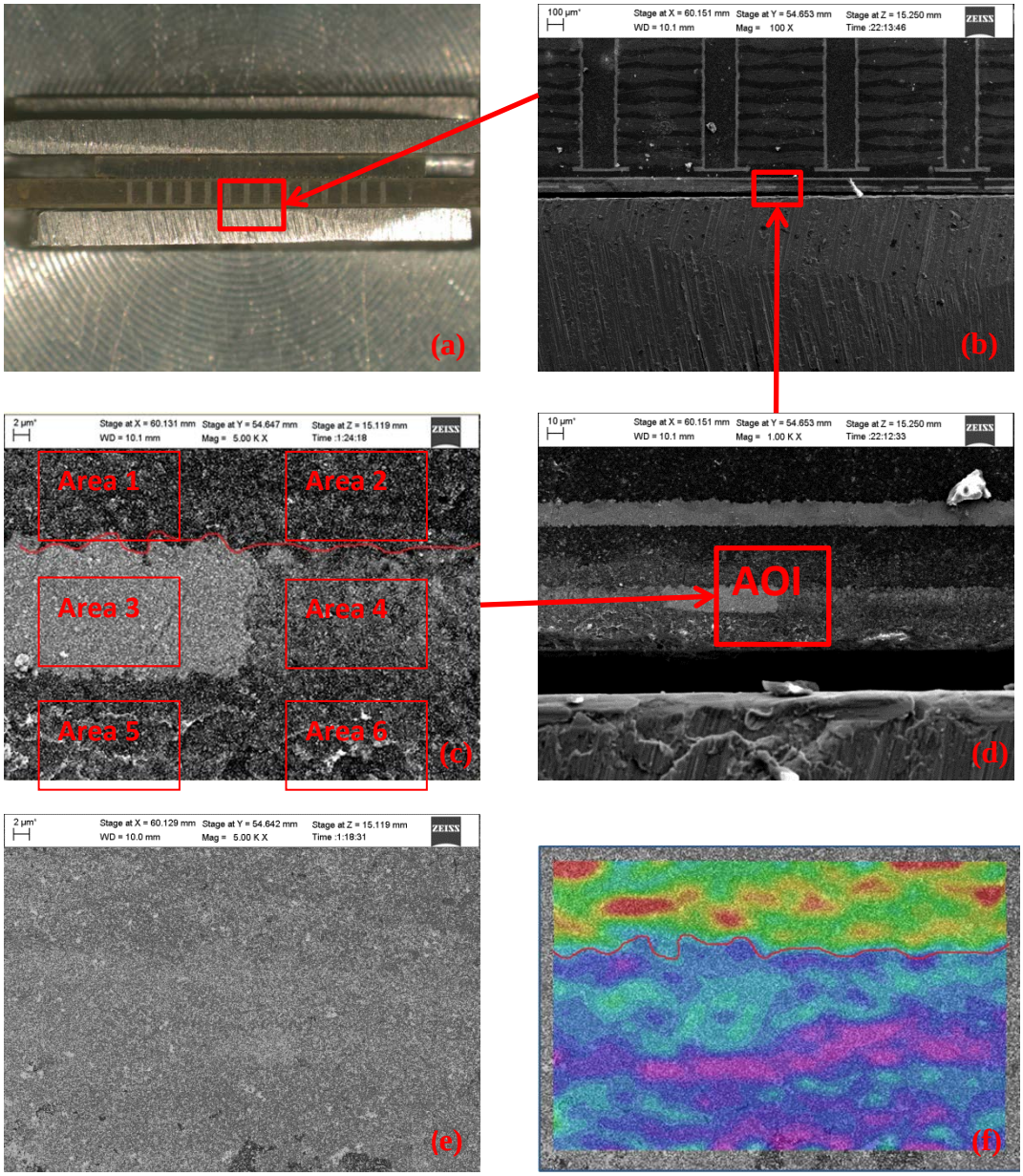

Figure 2.19: (a) Optical microscopy image: Specimen in the Aluminum holder; (b) 100X magnification SEM image using SE (secondary electron) detector; (c) AOI in the thermal test: 5000X magnification SEM image using SE detector; (d) same area of (c) at same magnification using BSE (back scattered electron) detector; (f) DIC strain field result using BSE image, the redline shows the strain field difference corresponding to the boundary of copper and polymer shown in (c)

In order to eliminate quantify the effect of scanning direction on the measurements, the specimen has been tested twice; once in 0^o degree arrangement and once when rotated by 90^o. Figure 2.20 shows the measured strain field at high temperature for 0^o and 90^o

scanning directions. Results clearly show that 1) the strain result is consistent regardless of the scanning direction, 2) the material is highly anisotropic, with the x and y directions having significantly different responses to thermal load and 3) the heterogeneous material component leads to strain variations due to different elastic moduli and different thermal expansion coefficients.

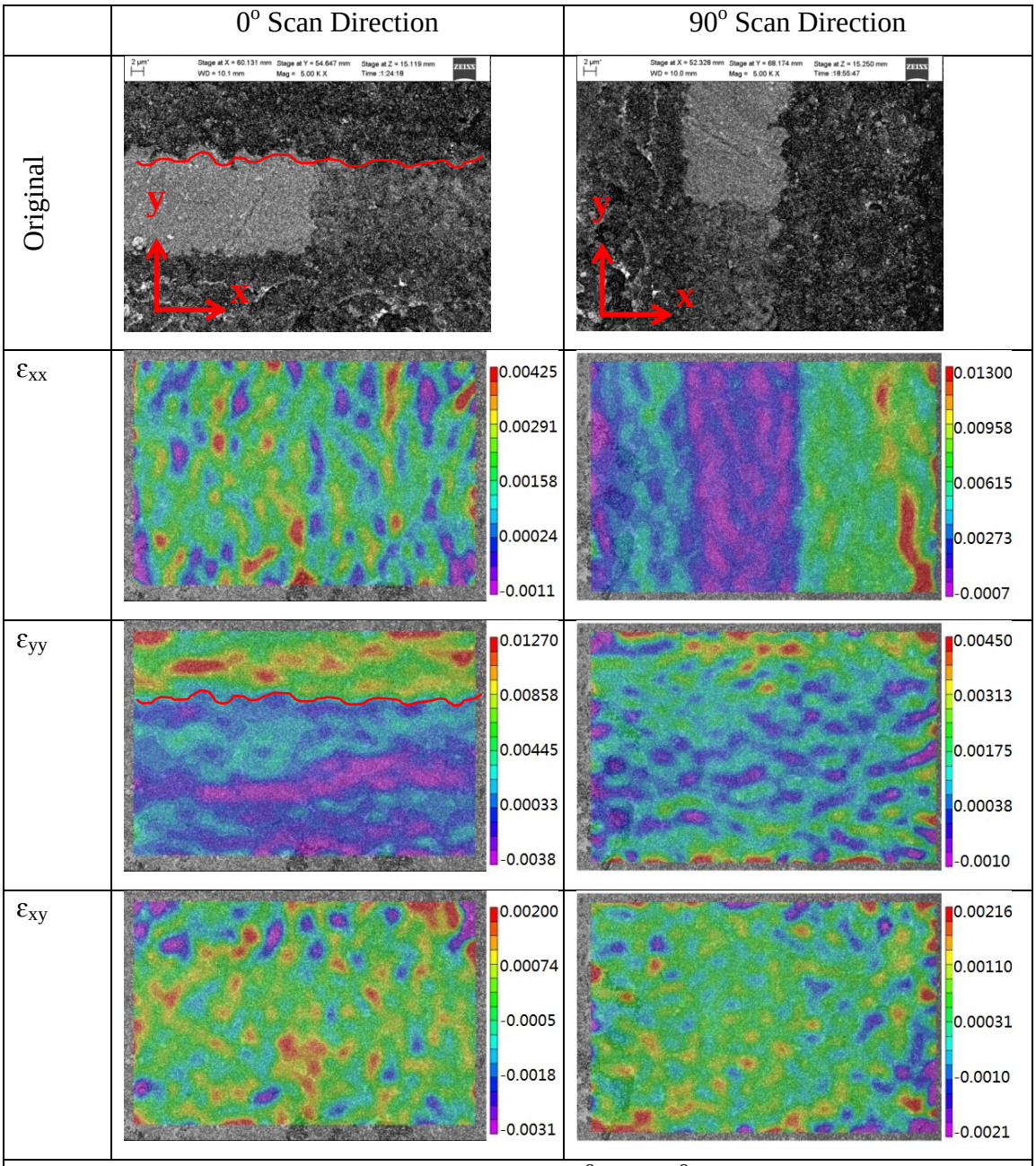

Figure 2.20: Strain field at high temperature for 0^o and 90^o scan directions

0^o Scan Direction

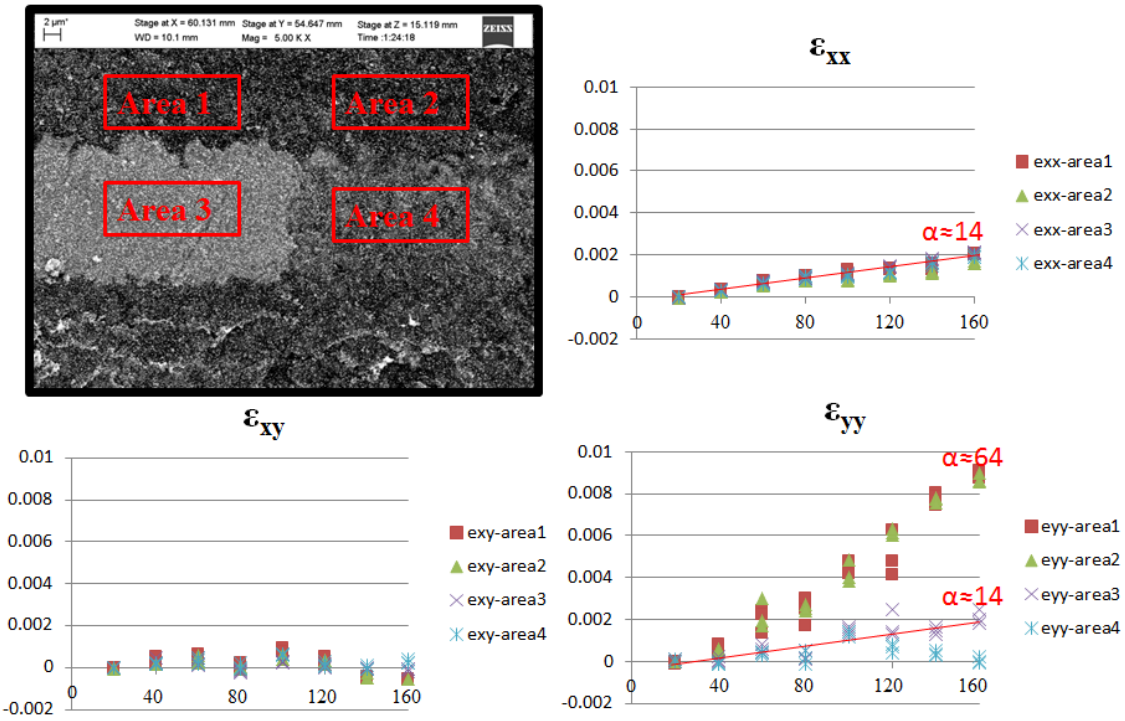

Figure 2.21: Strain vs temperature (°C) in each area for 0^o scan direction

90^o Scan Direction

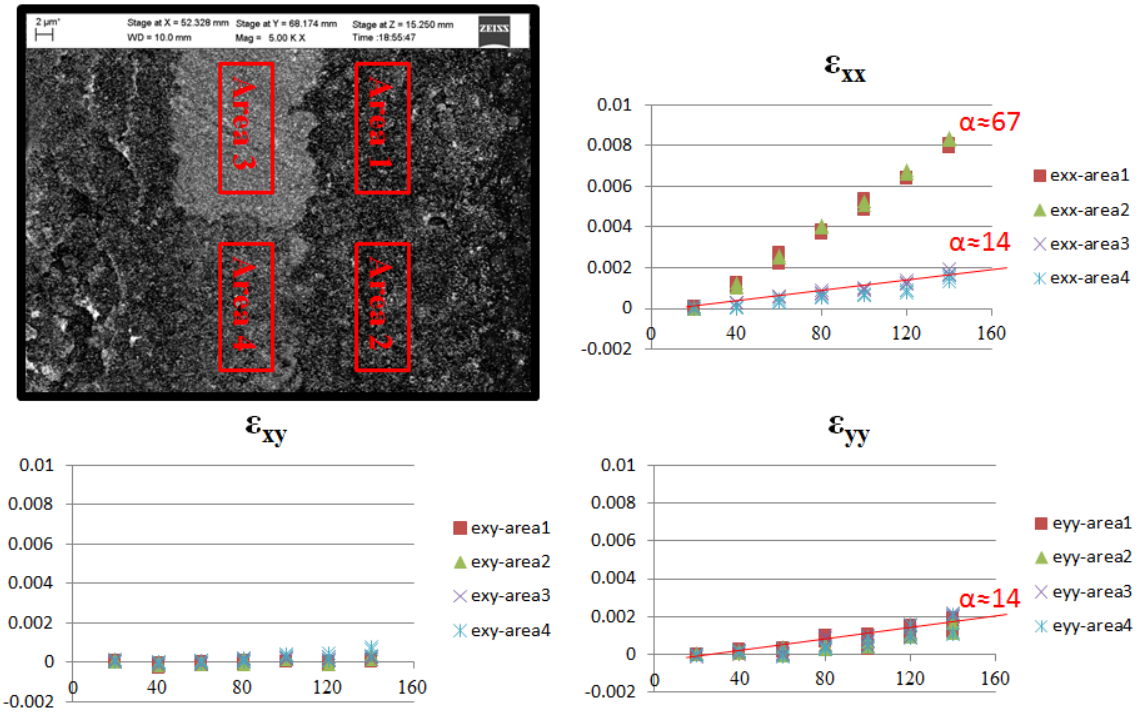

Figure 2.22: Strain vs temperature (°C) in each area for 90^o scan direction

Additional data is shown in Figure 2.21 and 2.22. Fig 2.21 shows the strain versus temperature from 25°C to 160°C for 0^o scan direction. Vic 2D with distortion correction methodology has been used to calculate the strain fields ε_{xx}, ε_{yy} and ε_{xy}. The subset size in the analysis is 21x21 pixels, and the step size is 5 pixels. The temperature has been measured by thermal couple on the top surface of the specimen. The plots show that the thermal response of this specimen is heterogeneous and non-uniform.

1) The average ε_{xx} in each selected area is almost same, with thermal expansion coefficient about $14x10^{-6}$m/m K, regardless of the material or structure differences.

2) The vertical strain, ε_{yy}, exhibits a different response when compared to ε_{xx}. The copper regions, areas 3 and 4, have similar thermal expansion rates as measured in the x-direction. The thermal expansion coefficient is still about $14x10^{-6}$m/m K, which is close to the value of pure copper, which is $16x10^{-6}$m/m K.

3) Areas 1 and 2 which are mainly polymer materials have much greater thermal expansion in the y-direction. The calculated thermal expansion coefficient is $64x10^{-6}$m/m K in the y-direction which is close to the literature value of epoxy, castings resins & compounds and underfill.

4) The value of ε_{xy} is always very small, indicating that the shear deformation is negligible in the regions being imaged.

5) We can detect the boundary of the change in specimen structure using the strain field difference. The red line shows the boundary of copper and polymer

Fig 2.22 shows the thermal test results in the same region after rotating the specimen 90^o. The results are almost the same as the 0^o configuration, which gives additional confidence in the experiment results.

2.9 High Magnification Imaging Results

A smaller particle size, ranging from 12nm down to 3nm, is needed for magnifications from 25,000x to 100,000x. Nano-sized colloidal Au nanoparticles have been used to pattern the specimen in our work. Using Au3+ and corresponding reductants, in principle the current self-assembly patterning method can give us particle sizes down to 2.6 nm gold particles. Figure 2.23(a) shows the 50,000x magnification image of Si wafer specimen which is patterned by 10nm Au particles. The uniform random distribution pattern is good for correlation analysis. A 5nm Alkanethiol Stabilized Gold Nanoparticles patterning result is shown in Figure 2.23(b). The image quality is not as good as for the10 nm result (one possible reason is 5nm size is out of the resolution limit of the Zeiss SEM we used), but the particle size is clearly quite small, suggesting that the method can be used to make quantitative measurements using DIC methods for extremely small regions. It is noted that the blurred particle edges allowed for accurate interpolation of the imaging pattern, which could improve the accuracy of the measured displacement and/or strain fields.

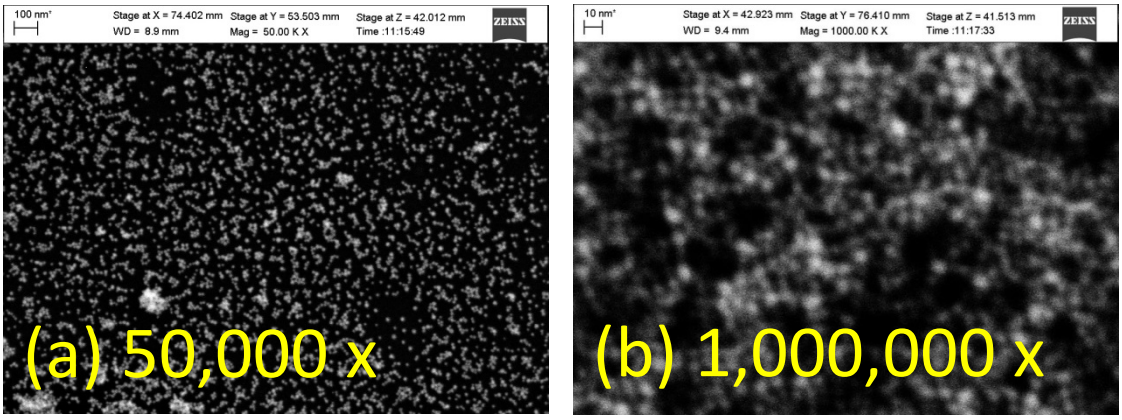

Figure 2.23: (a) 10nm particles at 50,000x; (b) 5nm particles at 1,000,000x

One issue we found at extremely high magnification is that images gradually blurred, even when there is no change in the SEM operational parameters. Figure 2.24 shows this phenomenon. Comparing images 2.24a and 2.24b, the working distance and Z-stage position are the same. However, the image is blurred after 12 minutes. Images 2.24c and 2.24d show similar results. It is believed the observed distortions are caused by "charging effects" for the nominally non-conducting sample [135]. In general, "charging effects" are image distortions due to accumulation/build-up of static electric charge on the specimen surface. The increase in static charge influences the electron beam, alters the image formation process and distorts the resulting image. Previous work [135] has shown

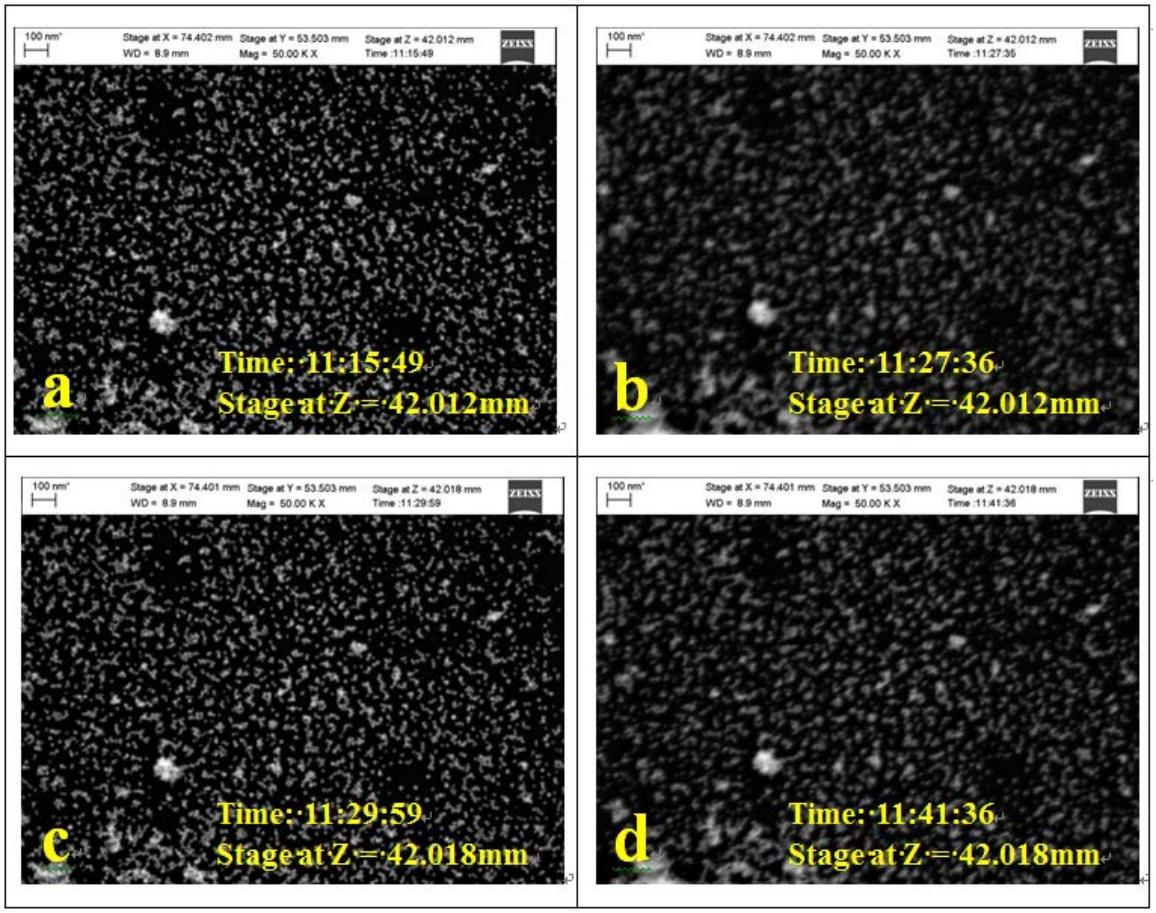

Figure 2.24: Gradual blurring of images caused by "charging effects"

that charging can cause a range of unusual effects, such as anomalous, heterogeneous contrast, which make it impossible to capture a uniform image of the specimen. In our work, the blurred image demonstrates that “charging” defocuses the image by changing the focus distance. Figure 2.25 shows this process graphically. In order to solve the issue, Z-stage position adjustment has been used to compensate the change. By translating the Z-stage a vertical distance of 8 microns (Figure 2.25c), we can recover a clear, well-focused, high contrast image of the specimen (Figure 2.24c) which is similar to the original image (Figure 2.24a).

From a quantitative standpoint, the measured strains also reflect this phenomenon. As shown in Figure 2.26, the strain values for both ε_{xx} and ε_{yy} gradually decrease with time from 0 min to 11 min. The decrease in strain values is caused by the change in the FOV size due to the effects of charging. Figure 2.25 graphically shows this effect. As shown in Fig. 2.25, defocusing of the specimen corresponds with an increase on FOV. This results in a reduction in the pixel size of same AOI, so that the image appears compressed with a negative strain value. After translation of the Z-stage, the image is re-focused without changing any SEM operational parameters (e.g., working distance, magnification); the AOI pixel size returns to approximately the same size as before. The measured strain value calculated using VIC-2D [52] also returns to its original, upstretched value and approaches zero. (point c in Fig. 2.26, which represents the refocused position.) The strain value gradually decreases again with time, from 14min to 25min.

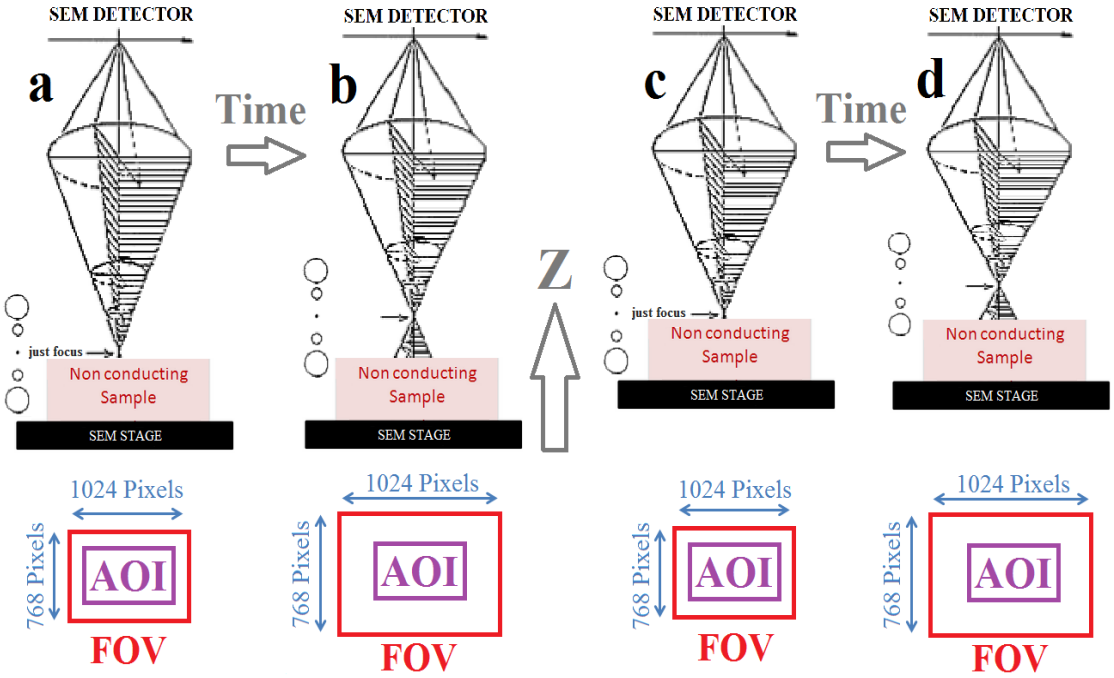

Figure 2.25: Image blurring mechanism and compensation method

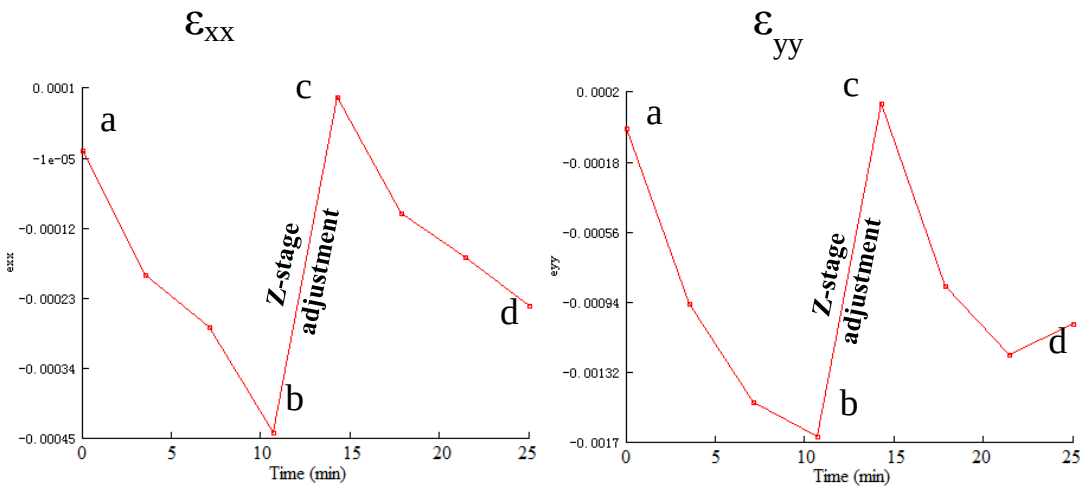

Figure 2.26: Strain change vs time due to charging effects and corrective Z-stage adjustment.

2.10 Conclusion

In summary, a simple and efficient approach is developed to study the heterogeneous nature of IC specimens at the micro-scale by measuring the non-uniform strain fields across the complex material constituents at temperatures from RT to ≈ 200°C using

images obtained with a Zeiss Ultraplus Thermal Field Emission SEM. For the first time, the authors present an experimental methodology using novel self-assembly techniques to randomly pattern the entire heterogeneous region on an IC package with a high contrast speckle pattern suitable for SEM imaging and digital image correlation. The minimum particle sizes in the experiments could reach 5nm, which give the ability to analysis the reduced length scale features being developed for the next generation IC packages. The experiments performed on baseline materials for temperatures in the range of 25°C to 200°C demonstrate that the complete process is effective for quantifying the thermal coefficient of expansion for different materials. The experiments on IC cross-sections clearly show the heterogeneous nature of the specimen and the associated non-uniform strain fields that are measured across the complex material constituents. The results confirm that the experimental methods for thermally loading the specimen and compensating for out-of-plane motions are effective for quantifying the thermal expansion of all material components for temperatures in the range of 25°C to 200°C. Since this methodology has no inherent material or structure requirements, it can be used for a broad range of micro- and nano-scale studies which can benefit from advanced full-field measurement capability for studies that include Microelectromechanical Systems (MEMS), Nanoelectromechanical (NEMS) devices, as well as other specialized nano-mechanical systems that incorporate various nano-structures and even some biological materials that are not appreciably damaged by the SEM image process.

REFERENCES

[1] Hahn, H. T. and S. W. Tsai "Nonlinear Elastic Behavior of Unidirectional Composite Laminae," J. Composite Materials, 7:102-118 (1973)

[2] Sun, C. T., W. H. Feng and S. L. Koh, "A theory for Physically Nonlinear Elastic Fiber-Reinforced Composite," Int. J. Engng. Sci., 12:919-935 (1974)

[3] Dvorak, G. J. & Bahei-El-Din, Y. A., Plasticity analysis of fibrous composites. .I. Appl. Mech., 49 (1982) 327-35.

[4] Adams, D. F. & Crane, D. A., Combined loading micromechanical analysis of a unidirectional composite. Composites, 15 (1984) 181-92.

[5] Griffin, Jr, 0. H., Kamat, M. P. & Herakovich, C. T., Three-dimensional inelastic finite element analysis of laminated composites. J. Comp. Muter., 5 (1981) 543-60.

[6] Surrel, Y. & Vautrin, A., On a modeling of the plastic response of FRP under monotonic loading. J. Camp. Mater., 23 (1989) 232-50.

[7] Sun, C. T. & Chen, J. L., A simple flow rule for characterizing nonlinear behavior of fiber composite. J. Camp. Mater., 23 (1989) 1009-20.

[8] Vaziri, R., Olson, M. D. & Anderson, D. L., A plasticity-based constitutive model for fiber-reinforced composite laminates. J. Comp. Muter., 25 (1991) 512-35.

[9] Hansen, A. C., Blackketter, D. M. & Walrath, D. E., An invariant-based flow rule for anisotropic plasticity applied to composite materials. J. Appl. Mech., 58 (1991) 881-8.

[10] Schmidt, R. J., Wang, D. Q. & Hansen, A. C., Plasticity model for transversely isotropic materials. J. Eng. Mech., 119 (1993) 748-66.

[11] Sun, C. T. & Chen, J. L., A micromechanical model for plastic behavior of fibrous composites. Comp. Sci. Technol., 40 (1991) 115-29.

[12] C. T. Sun and K. J. Yoon (1992), 'Elastic–Plastic Analysis of AS4/PEEK Composite Laminate using a One-Parameter Plasticity Model', Journal of Composite Materials 26, 293–308.

[13] D. Kenaga, J. F. Doyle and C. T. Sun (1987), 'The Characterization of Boron/Aluminum Composite in the Nonlinear Range as an Orthotropic Elastic–Plastic Material', Journal of Composite Materials 21, 516–531.

[14] J. L. Chen and C. T. Sun (1993), 'A Plastic Potential Function Suitable for Anisotropic Fiber Composites', Journal of Composite Materials 27, 1379–1390.

[15] V. Tamužs, J. Andersons (2002), E. Sparnins and J. Varn, 'Response of Cross-Ply Composite to Off-Axis Loading', Journal of Composite Materials 36, 125–2134.

[16] V. Tamužs, J. Andersons (1998), K. Aniskevic, J. Jansons and J. Korsgaar, 'Creep and Damage Accumulation in Orthotropic Composites under Cyclic Loading', Mechanics of Composite Materials 34, 1998, 321–330.

[17] Vaziri, R., Olson,M. D., and Anderson, D. L., 'A Plasticity-based ConstitutiveModel for Fiberreinforced Composite Laminates', Journal of Composite Materials 25, 1991, 512–535.

[18] G. Odegard, K. Searles, and M. Kumosa (2000), 'Nonlinear Analysis of Woven Fabric-reinforced Graphite/PMR-15 Composites under Shear-dominated Biaxial Loads', Mechanics of Composite Materials and Structures 7, 129–152.

[19] S. Ogihara & K. Reifsnider (2002), 'Characterization of nonlinear behavior in woven composite laminates', Applied Composite Materials, 9(4), 249-263.

[20] V. Tamuzes; K. Dzelzitis & K. Reifsnider (2004), 'Fatigue of woven composite laminates in off-axis loading I. The mastercurves', Applied Composite Materials 11(5), 259-279.

[21] L. Xing; K. Reifsnider & X. Huang (2009), 'Progressive damage modeling for large deformation loading of composite structures', Composites Science And Technology 69(6), 780-784.

[22] P. Pollock, L-Y Yu, M. A. Sutton, S-M Guo, P. Majumdar and M. Gresil, “Full-Field Measurements for Determining Orthotropic Elastic Parameters of Woven Glass-Epoxy Composites Using Off-Axis Tensile Specimens, Experimental Techniques (in press). Article first published online: 12 JUN 2012 DOI: 10.1111/j.1747-1567.2012.00824.x

[23] Wisnom. M. R. “On the high compressive strains achieved in bending tests on unidirectional carbon-fiber/epoxy” Composites Science and Technology, Volume 43, Issue 3, 1992, Pages 229–235

[24] Wisnom. M. R., “Limitations of linear elastic bending theory applied to four point bending of unidirectional carbon fiber/epoxy”, Proc. AIAA Structures, Structural Dynamics& Materials Conf., Long Beach, April 1990, pp 740-747

[25] Whitney, J. M., Danial, I.M. & Pipes, R. B., “Experimental mechanics of fiber reinforce composite materials”. Society for Experimental Mechanics Monograph No. 4, revised edition 1984, p. 167

[26] Yang, B; Kozey, V; Adanur, S; Kumar, S (2000) "Bending, compression, and shear behavior of woven glass fiber-epoxy composites", Composites Part B, 31(8) 715-721.

[27] Van Paepegem, W; Degrieck, J (2001) "Experimental set-up for and numerical modelling of bending fatigue experiments on plain woven glass/epoxy composites", Composite Structures 51(1) 1-8.

[28] W.Van Paepegem, J.Degrieck. (2001), 'Experimental set-up for and numerical modeling of bending fatigue experiments on plain woven glass/epoxy composites', Journal of Composite Structures, 51, 1-8.

[29] S. C. Quek, A. M. Waas, K. W. Shahwan, V. Agaram. (2006), 'Failure mechanics of triaxially braided carbon composites under combined bending-compression loading', Journal of Composites Science and Technology 66, 2548–2556.

[30] M. R. Wisnom and J. W. Atkinson. (1997), 'Constrained buckling tests show increasing compressive strain to failure with increasing strain gradient', Journal of Composites Part A 28A, 959-964.

[31] MA Sutton, WJ Wolters, WH Peters, WF Ranson, SR McNeill. (1983), 'Determination of displacements using an improved digital correlation method', Image and Vision Computing, 1(3): 133-9.

[32] WH Peters III, WF Ranson, MA Sutton, TC Chu, J Anderson, (1983), "Application of Digital Correlation Methods to Rigid Body Mechanics", Optical Engineering, 22 (6) 738-743.

[33] HA Bruck, SR McNeill, MA Sutton, and WH Peters, III, (1989), "Determination of Deformations Using Digital Correlation with the Newton-Raphson Method for Partial Differential Corrections", Experimental Mechanics, 29 (3) 261-267.

[34] PF Luo, YJ Chao and MA Sutton, (1994), "Application of Stereo Vision to 3-D Deformation Analysis in Fracture Mechanics", Optical Engineering, 33 (3), 981-990.

[35] PF Luo, YJ Chao and MA Sutton and W.H.Peters, III, (1993), "Accurate Measurement of Three-Dimensional Deformations in Deformable and Rigid Bodies Using Computer Vision", Experimental Mechanics, 33 (2) 123-133.

[36] JD Helm, SR McNeill and MA Sutton, (1996),"Improved 3-D Image Correlation for Surface Displacement Measurement", Optical Engineering, , 35 (7) 1911-1920.

[37] JD Helm, MA Sutton and SR McNeill, (2003), "Deformations in wide, center-notched, thin panels: Part I: Three dimensional shape and deformation measurements by computer vision", Optical Engineering, 42 (5) 1293-1305.

[38] JD Helm, MA Sutton and SR McNeill, (2003), "Deformations in wide, center-notched, thin panels: Part II: Finite element analysis and comparison to experimental measurements", Optical Engineering, 42 (5) 1306-1320.

[39] MA Sutton, JJ Orteu and HW Schreier, (March 27, 2009), Image Correlation for Shape, Motion and Deformation Measurements, ISBN 978-0-387-78746-6 Springer, Springer Science + Business Media, LLC, 233 Spring Street, New York, NY 10013, USA

[40] A.Willems, S.V. Lomov, I.Verpoest, D.Vandepitte, (2008), 'Optical Strain field in shear and tensile testing of textile reinforcements', Journal of Composites science and technology 68, 2008, 807-819

[41] S.Giancane, F.W.Panella, R.Nobile, V.Dattoma, (2010), 'Fatigue damage evolution of fiber reinforced composites with digital image correlation analysis', Journal of Procedia Engineering, 2, 2010, 1307-1315

[42] M.A. Sutton, J.H. Yan, V. Tiwari, H.W. Schreier and J.J. Orteu, (2008),"The Effect of Out-of-Plane Motion on 2D and 3D Digital Image Correlation Measurements", Optics and Lasers in Engineering, 46 746– 757.

[43] Gruttmann, F; Wagner, W; Meyer, L; Wriggers, P (1993) "A nonlinear composite shell element with continuous interlaminar shear stresses", Computational Mechanics, 13(3) 175-188 doi: 10.1007/bf00370134

[44] Lomov SV; Ivanov DS; Verpoest I; Zako M, Kurashiki T, Nakai H, Molinard J and Vautrin A (2007) “Full-field strain measurements for validation of meso-FE analysisof textile composites’, Composites: Part A 39 1218–1231.

[45] Omidvar, B; Ghorbanpoor, A (1996) "Nonlinear FE Solution for Thin-Walled Open-Section Composite Beams", Journal of Structural Engineering, 122(11), 1369-1378.

[46] Krawczyk, P; Frey, F; Zielinski, A P (2007) "Large deflections of laminated beams with interlayer slips: Part 1: model development", Engineering Computations: Int J for Computer-Aided Engineering, 24(1), 17-32.

[47] Jun, L; Hongxing, H (2009) "Dynamic stiffness analysis of laminated composite beams using trigonometric shear deformation theory", Composite Structures, 89(3) 433-442.

[48] Reddy, J N, An introduction to nonlinear finite element analysis: Oxfrd University Press.

[49] Hahn, H T; Tsai, S W (1973) "Nonlinear Elastic Behavior of Unidirectional Composite Laminae", Journal of Composite Materials, 7(1) 102-118 doi: 10.1177/002199837300700108

[50] Hu, Hsuan-Teh (1993) "Influence of in-plane shear nonlinearity on buckling and postbuckling responses of composite plates and shells", Journal of Composite Materials (ISSN 0021-9983), 27 (2) 138-151.

[51] Bisshopp, K E; Drucker, D C (1945) "Large Deflection of Cantiveler Beams", Quarterly of applied Math, 3(3), 272-275.

[52] Correlated Solutions, Incorporated, www.correlatedsolutions.com, 2009~2013

[53] MA Sutton, J Yan, X Deng, C-S Cheng and P Zavattieri, (2007), “3D Digital Image Correlation to Quantify Deformation and COD in Ductile Aluminum Under Mixed-mode I/III Loading”, Optical Engineering 46(5) 051003-1 to 051003-17.

[54] E-F 5 and I Chirica, 2011, Buckling and Post-buckling Analysis of Composite Plates In "Advances in Composite Materials - Ecodesign and Analysis", Intech Publisher.

[55] C.T. Sun and J.L. Tsai, " Comparison Of Microbuckling Model And. Kink Band Model In Predicting Compressive Strengths Of Composites", ID 1445, 13th International Conference on Composite Materials (2001)

[56] S. Pansart, M. Sinapius, U. Gabbert, "A comprehensive explanation of compression strength differences between various CFRP materials: Micro-meso model, predictions, parameter studies", Composites: Part A 40 (2009) 376–387

[57] ABAQUS, (2008) "Analysis User's Manual," 6-9.2 ed.

[58] Zhigang Wei, Xiaomin Deng, Michael A. Sutton, Junhui Yan, C.-S. Cheng Pablo Zavattieri, “Modeling of mixed-mode crack growth in ductile thin sheets under combined in-plane and out-of-plane loading”, Engineering Fracture Mechanics, 78 (17), 3082-3101 (2011).

[59] Jahnke Emde, (1938) Functionentafeln, 52-90.

[60] M.A. Sutton, Recent developments and trends in measurements from the macro-scale to reduced length scales, Y. Berthaud (Ed.) et al., Proc. Photomécanique, Albi, France, Ecole des Mines d'Albi (2004), pp. 1–8

[61] Rastogi P K 2000 Photomechanics (Topics in Applied Physics) (Berlin: Springer)

[62] M. Kujawinska Modern optical measurement station for micro-materials and micro-elements studies Sens Actuators A Phys, 99 (2002), pp. 144–153

[63] Hariharan, P. (2007). Basics of Interferometry. Elsevier Inc. ISBN 0-12-373589-0.

[64] Sirkis J S and Lim T J 1991 Displacement and strain-measurement with automated grid methods Exp. Mech. 31 382–8

[65] Goldrein H T, Palmer S J P and Huntley J M 1995 Automated fine grid technique for measurement of large-strain deformation maps Opt. Lasers Eng. 23 305–18

[66] MA Sutton, WJ Wolters, WH Peters, WF Ranson, SR McNeill. (1983), ‘Determination of displacements using an improved digital correlation method’, Image and Vision Computing, 1(3): 133-9.

[67] WH Peters III, WF Ranson, MA Sutton, TC Chu, J Anderson, (1983), "Application of Digital Correlation Methods to Rigid Body Mechanics", Optical Engineering, 22 (6) 738-743.

[68] HA Bruck, SR McNeill, MA Sutton, and WH Peters, III, (1989), "Determination of Deformations Using Digital Correlation with the Newton-Raphson Method for Partial Differential Corrections", Experimental Mechanics, 29 (3) 261-267.

[69] PF Luo, YJ Chao and MA Sutton, (1994), "Application of Stereo Vision to 3-D Deformation Analysis in Fracture Mechanics", Optical Engineering, 33 (3), 981-990.

[70] PF Luo, YJ Chao and MA Sutton and W.H.Peters, III, (1993), "Accurate Measurement of Three-Dimensional Deformations in Deformable and Rigid Bodies Using Computer Vision", Experimental Mechanics, 33 (2) 123-133.

[71] JD Helm, SR McNeill and MA Sutton, (1996),"Improved 3-D Image Correlation for Surface Displacement Measurement", Optical Engineering, , 35 (7) 1911-1920.

[72] JD Helm, MA Sutton and SR McNeill, (2003), "Deformations in wide, center-notched, thin panels: Part I: Three dimensional shape and deformation measurements by computer vision", Optical Engineering, 42 (5) 1293-1305.

[73] JD Helm, MA Sutton and SR McNeill, (2003), "Deformations in wide, center-notched, thin panels: Part II: Finite element analysis and comparison to experimental measurements", Optical Engineering, 42 (5) 1306-1320.

[74] MA Sutton, JJ Orteu and HW Schreier, (March 27, 2009), Image Correlation for Shape, Motion and Deformation Measurements, ISBN 978-0-387-78746-6 Springer, Springer Science + Business Media, LLC, 233 Spring Street, New York, NY 10013, USA

[75] Yoneyama S, Kitagawa A, Iwata S, Tani K and Kikuta H 2007 Bridge deflection measurement using digital image correlation Exp. Tech. 31 34–40

[76] Kang J, Ososkov Y, Embury J D and Wilkinson D S 2007 Digital image correlation studies for microscopic strain distribution and damage in dual phase steels Scr. Mater. 56 999–1002

[77] Jonnalagadda K N, Chasiotis I, Yagnamurthy S, Lambros J, Pulskamp J, Polcawich R and Dubey M 2010 Experimental investigation of strain rate dependence of nanocrystalline Pt films Exp. Mech. 50 25–35

[78] Tatschl A and Kolednik O 2003 A new tool for the experimental characterization of micro-plasticity Mater. Sci. Eng. A 339 265–80

[79] Tanaka Y, Naito K, Kishimoto S and Kagawa Y 2011 Development of a pattern to measure multiscale deformation and strain distribution via in situ FE-SEM observations Nanotechnology 22 115704

[80] Sun Z L, Lyons J S and McNeill S R 1997 Measuring microscopic deformations with digital image correlation Opt. Lasers Eng. 27 409–28

[81] Pitter M C et al 2002 Focus errors and their correction in microscopic deformation analysis using correlation Opt. Eng. 23 1361–7

[82] Zhang D S, Luo M and Arola D D 2006 Displacement/strain measurements using an optical microscope and digital image correlation Opt. Eng. 45 033605

[83] Berfield T A, Patel H K, Shimmin R G, Braun P V, Lambros J and Sottos N R 2006 Fluorescent image correlation for nanoscale deformation measurements Small 2 631–5

[84] Franck C et al 2007 Three-dimensional full-field measurements of large deformations in soft materials using confocal microscopy and digital volume correlation Exp. Mech. 47 427–38

[85] Sabate N et al 2006 Measurement of residual stresses in micromachined structures in a microregion Appl. Phys. Lett. 88 071910

[86] Keller J et al 2006 FibDAC—residual stress determination by combination of focused ion beam technique and digital image correlation Mater. Sci. Forum 524–525 121–6

[87] Sabate N et al 2006 Digital image correlation of nanoscale deformation fields for local stress measurement in thin films Nanotechnology 17 5264–70

[88] Sabate N et al 2007 Residual stress measurement on a MEMS structure with high-spatial resolution J. Microelectromech. Syst. 16 365–72

[89] Kang J et al 2005 Microscopic strain mapping using scanning electron microscopy topography image correlation at large strain J. Strain Anal. Eng. Des. 40 559–70

[90] Wang H et al 2006 Error analysis of digital speckle correlation method under scanning electron microscope Exp. Tech. 30 42–5

[91] Lagattu F et al 2006 In-plane strain measurements on a microscopic scale by coupling digital image correlation and an in situ SEM technique Mater. Charact. 56 10–8

[92] Sutton MA, Li N, Garcia D, Cornille N, Orteu JJ, McNeill SR, Schreier HW, Li X, Metrology in a scanning electron microscope: theoretical developments and experimental validation, Measurement Science and Technology 17 pp. 2613-2622, (2006).

[93] Sutton MA, Li N, Joy DC, Reynolds AP, Li X, Scanning electron microscopy for quantitative small and large deformation measurements part I: SEM imaging at magnifications from 200 to 10,000. Experimental Mechanics 47, pp 775–787, 10.1007/s11340-007- 9042-z, (2007).

[94] Sutton MA, Li N, Garcia D, Cornille N, Orteu JJ, McNeill SR, Schreier HW, Li X, Reynolds AP, Scanning electron microscopy for quantitative small and large deformation measurements part II: Experimental validation for magnifications from 200 to 10,000. Experimental Mechanics 47, pp 789–804, 10.1007/s11340-007-9041-0, (2007).

[95] Chasiotis I and Knauss W G 2002 A new microtensile tester for the study of MEMS materials with the aid of atomic force microscopy Exp. Mech. 42 51–7

[96] Knauss W G, Chasiotis I and Huang Y 2003 Mechanical measurements at the micron and nanometer scales Mech. Mater. 35 217–31

[97] Cho S W et al 2005 Young's modulus, Poisson's ratio and failure properties of tetrahedral amorphous diamond-like carbon for MEMS devices J. Micromech. Microeng. 15 728–35

[98] Chasiotis I and Knauss W G 2002 Size effects determined from tensile tests of perforated MEMS scale specimens Proc. MRS 687 (Boston, MA) pp 241–6

[99] Cho S W, Cardenas-Garcia J F and Chasiotis I 2005 Measurement of nanodisplacements and elastic properties of MEMS via the microscopic hole method Sensors Actuators A 120 163–71

[100] Chasiotis I 2004 Mechanics IEEE Trans. Device Mater. Reliab. 4 176–88

[101] Chang S et al 2005 Nanoscale in-plane displacement evaluation by AFM scanning and digital image correlation processing Nanotechnology 16 344–9

[102] Sun Y F and Pang J H L 2006 AFM image reconstruction for deformation measurements by digital image correlation Nanotechnology 17 933–9

[103] Li X D et al 2007 In situ nanoscale in-plane deformation studies of ultrathin polymeric films during tensile deformation using atomic force microscopy and digital image correlation techniques IEEE Trans. Nanotechnology 6 4–12

[104] Li X D et al 2006 Nanoscale deformation and cracking studies of advanced metal evaporated magnetic tapes using atomic force microscopy and digital image correlation techniques Meas. Sci. Technol. 22 835–44

[105] Sun Y F, Pang J H L and Fan W 2007 Nanoscale deformation measurement of microscale interconnection assemblies by a digital image correlation technique Nanotechnology 18 395504

[106] Vendroux G and Knauss WG 1998 Submicron deformation field measurements: Part 1. Developing a digital scanning tunneling microscope Exp. Mech. 38 18–23

[107] Vendroux G and Knauss W G 1998 Submicron deformation field measurements: Part 2. Improved digital image correlation Exp. Mech. 38 86–92

[108] Vendroux G, Schmidt N and Knauss W G 1998 Submicron deformation field measurements: Part 3. Demonstration of deformation determinations Exp. Mech. 38 154–60

[109] Sutton M A, McNeill S R, Helm J D and Chao Y J 2000 Advances in two-dimensional and three-dimensional computer vision photomechanics Top. Appl. Phys. 77 323–72

[110] Berfield TA, Patel JK, Shimmin RG, Braun PV, Lambros J, Sottos NR (2006) Fluorescent image correlation for nanoscale deformation measurements. Small 2:631–635

[111] Berfield TA, Patel JK, Shimmin RG, Braun PV, Lambros J, Sottos NR (2007) Micro- and nanoscale deformation measurement of surface and internal planes via digital image correlation. Exp Mech 47:51–62. doi:10.1007/s11340-006-0531-2

[112] Scrivens W A, Luo Y, Sutton M A, Collete S A, Myrick M L, Miney P, Colavira P E, Reynolds A P and Li X 2007 Development of patterns for digital image correlation measurements at reduced length scales Exp. Mech. 47 63–77

[113] Collette S A et al 2004 Development of patterns for nanoscale strain measurements: I. fabrication of imprinted Au webs for polymeric materials Nanotechnology 15 1812–7

[114] Tschopp M A, Bartha B B, Porter W J, Murray P T and Fairchild S B 2009 Microstructure-dependent local strain behavior in polycrystals through in situ scanning electron microscope tensile experiments Metall. Mater. Trans A 40 2363–8

[115] Li N, Guo S and Sutton M A 2011 Recent progress in e-beam lithography for SEM patterning, MEMS and Nano., Volume 2, Conf. Proc. Soc. for Exp. Mech. Ser. 2, ed T Proulx (New York: Springer) pp 163–6

[116] Walley JL, Wheeler R, Uchic MD, Mills MJ (2012) In-situ mechanical testing for characterizing strain localization during deformation at elevated temperatures. Exp Mech 52:405–416. doi:10.1007/s11340-011-9499-7

[117] Kammers AD, Daly S (2011) Small-scale patterning methods for digital image correlation under scanning electron microscopy. Meas Sci Technol 22:125501

[118] Kammers, AD and Daly S, Self-assembled nanoparticle surface patterning for improved digital image correlation in a scanning electron microscope, Experimental Mechanics (in press).

[119] Grella EL, Luciani L, Gentili M, Baciocchi M, Figliomeni M, Mastrogiacomo L, Maggiora R, Leonard Q, Cerrina F, Molino M, Powderly D (1993) Metrology of high-resolution resist structures on insulating substrates. J Vac Sci Technol, B, Microelectron Nanometer Struct 11(6):2456–2462.

[120] Berger JR, Drexler ES, Read DT (1998) Error analysis and thermal expansion measurement with electron-beam moiré. Exp Mech 38(3):167–171.

[121] MeX software. Alicona imaging. http://www.alicona.com.

[122] SAMx. 3D TOPx package. http://www.samx.com.

[123] Lacey AJ, Thacker NA, Yates RB (1996) Surface approximation from industrial SEM images. British Machine Vision Conference (BMVC'96), 725–734.

[124] Agrawal M, Harwood D, Duraiswami R, Davis L, Luther P (2000) Three-dimensional ultrastructure from transmission electron microscope tilt series, 2nd Indian Conference on Vision, Graphics and Image Processing (ICVGIP 2000). Bangalore, India.

[125] Vignon F, Le Besnerais G, Boivin D, Pouchou JL,Quan L (2001) 3D reconstruction from scanning electron microscopy using stereovision and self-calibration. Physics in signal and image processing, Marseille, France, June.

[126] Sinram O, Ritter M, Kleindiek S, Schertel A, Hohenberg H, Albertz J (2002) Calibration of an SEM, using a nano positioning tilting table and a microscopic calibration pyramid. ISPRS Commission V Symposium, Corfu, Greece, pp 210–215.

[127] Doumalin P (2000) Microextensométrie locale par correlation d'images numériques. PhD thesis, Ecole Polytechnique.

[128] Hemmleb M, Albertz J (2000) Microphotography—the photogrammetric determination of friction surfaces. IAPRS XXXIII, Amsterdam, The Netherlands.

[129] Lee HS, Shin GH, Park HD (2003) Digital surface modeling for assessment of weathering rate of weathered rock in stone monuments. The International Archives of the Photogrammetry, Remote Sensing and Spatial Information Sciences, Ancona, Italy, July.

[130] Bi H, Hartsough C, Han B (2006) Nano-pattern recognition and correlation technique for deformation measurement of nanostructures. 7th International Symposium on MEMS and Nanotechnology (7th-ISMAN), St. Louis, MO, USA, pp 148–149 June.

[131] Schreier HW, Garcia D, Sutton MA (2004) Advances in light microscope stereo vision. Exp Mech 443:278–288

[132] Li N, Sutton MA, Li X, Schreier H.W., Full-field Thermal Deformation Measurements in a Scanning Electron Microscope by 2D Digital Image Correlation, Experimental Mechanics 48, pp 635–646, 10.1007/s11340-007-9107-z, (2007).

[133] Instec, Inc. http://www.instec.com/

[134] ASM International, Metals Handbook, Volume 2 10th Edition, p 128

[135] Ki Hyun Kim1, Zentaro Akase1, Toshiaki Suzuki and Daisuke Shindo, Charging Effects on SEM/SIM Contrast of Metal/Insulator System in Various Metallic Coating Conditions, Materials Transactions, Vol. 51, No. 6 (2010) pp. 1080 to 1083

APPENDIX A

Full-field results for axial strain, ε_{xx}, transverse strain, ε_{yy}, and shear strain, ε_{xy}, for 0/90 and 45/45 specimens

	Compression Side	Tension Side
ε_{xx}	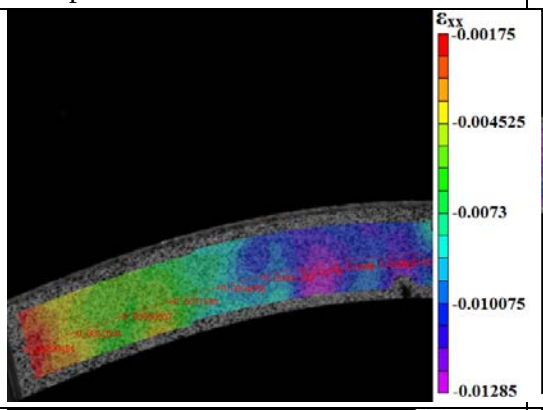	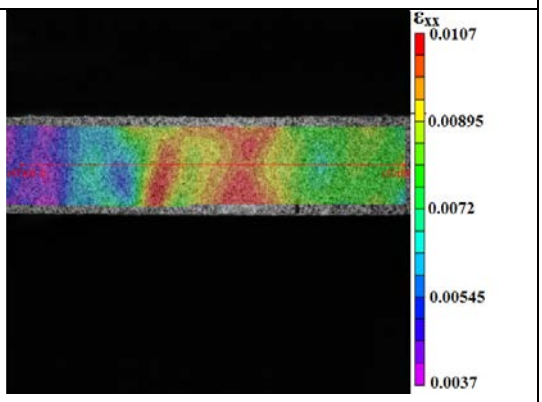
ε_{yy}	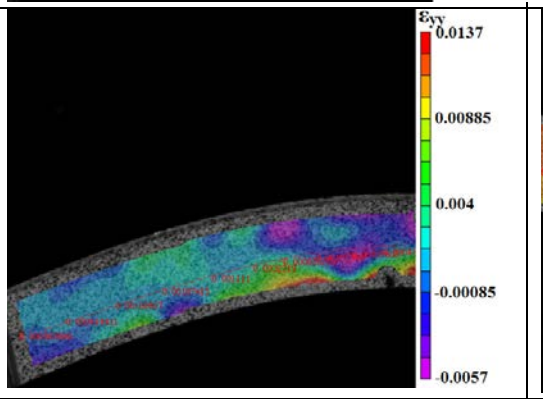	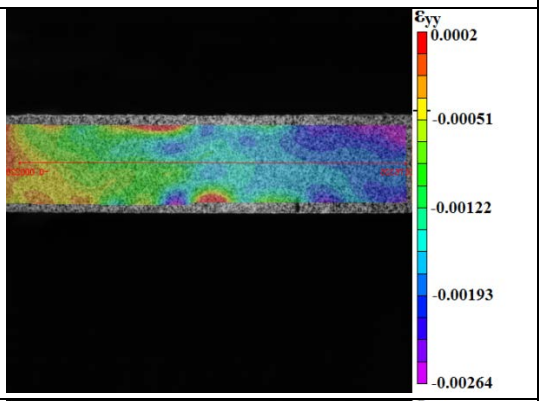
ε_{xy}	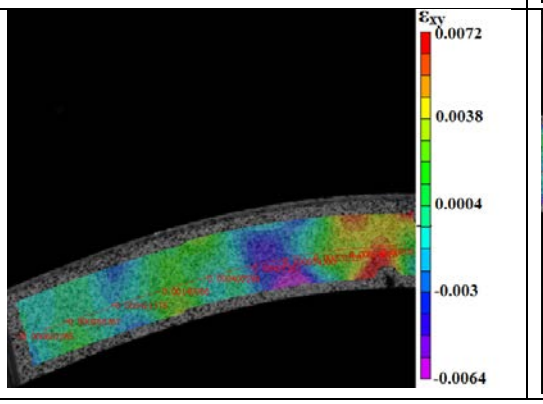	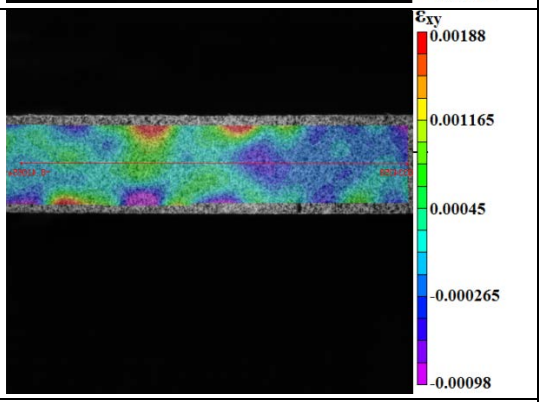

Figure A.1: Strain fields ε_{xx}, ε_{yy}, ε_{xy} for 0/90 specimen, when end displacement Δ is 10.08 mm and corresponding deflection w of specimen center is 19.16 mm

	Compression Side	Tension Side
ε_{xx}	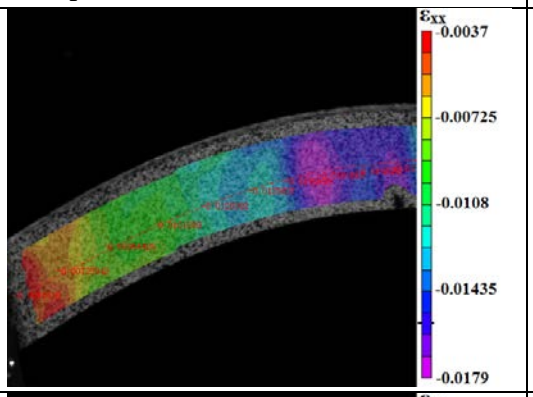	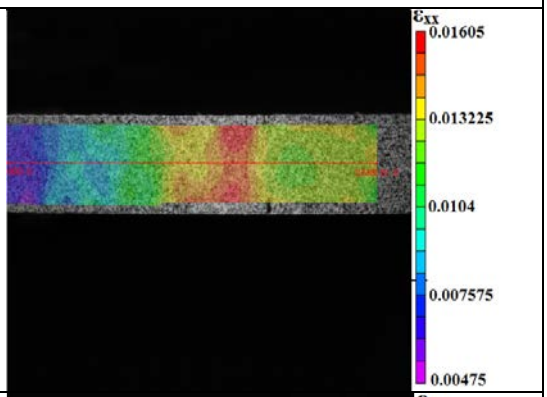
ε_{yy}	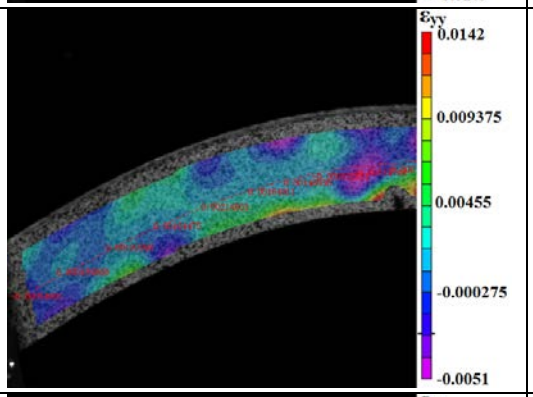	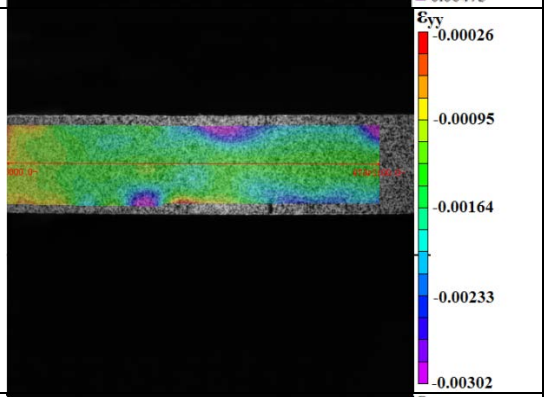
ε_{xy}	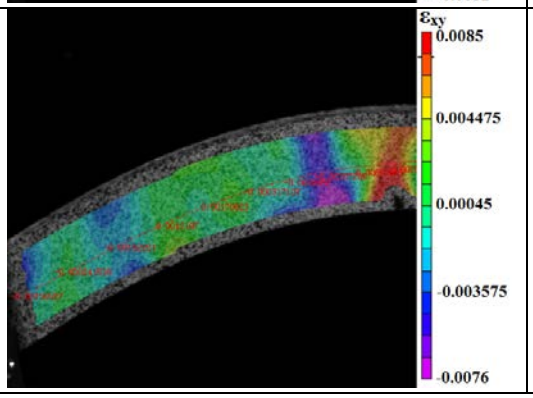	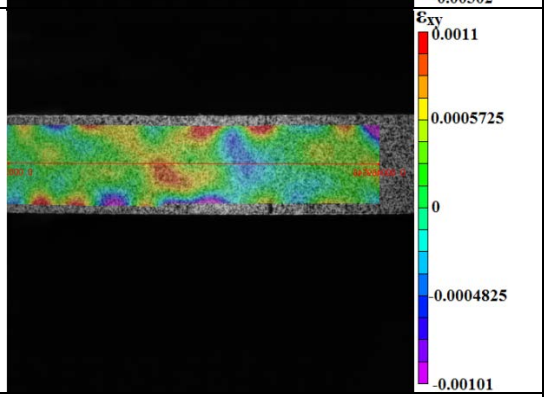

Figure A.2: Strain fields ε_{xx}, ε_{yy}, ε_{xy} for 0/90 when end displacement Δ is 19.97 mm and corresponding deflection w of specimen center is 26.35mm

	Compression Side	Tension Side
ε_{xx}	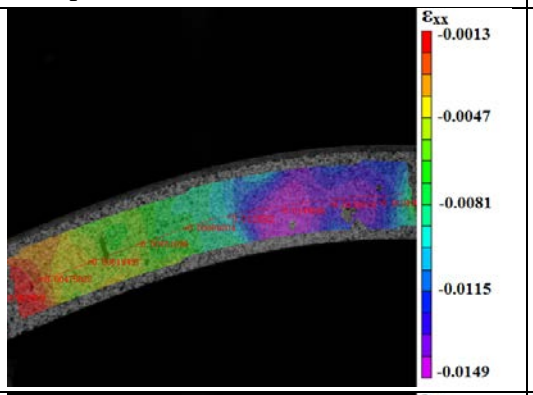	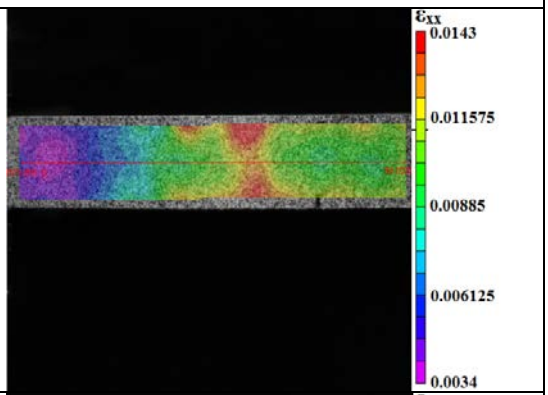
ε_{yy}	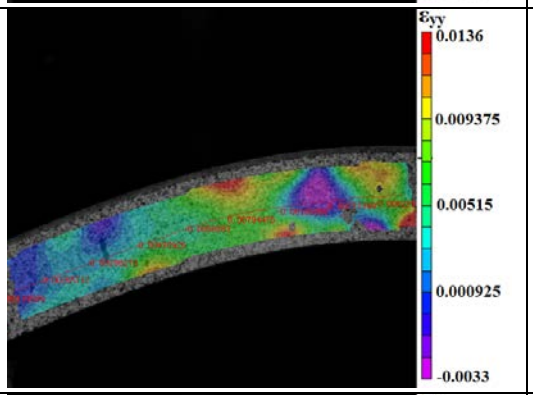	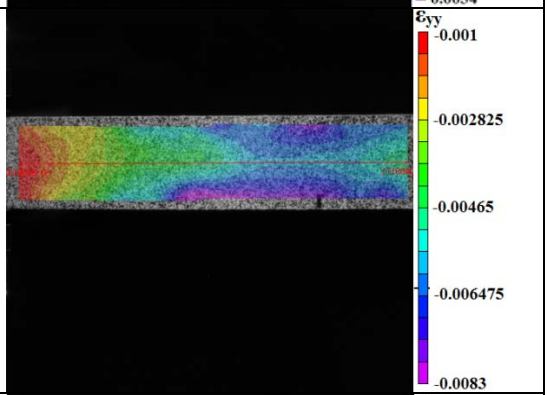
ε_{xy}	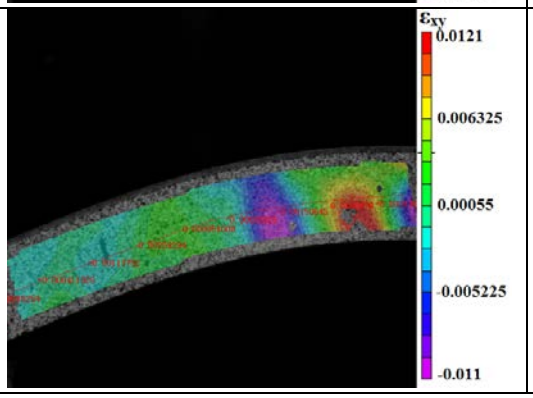	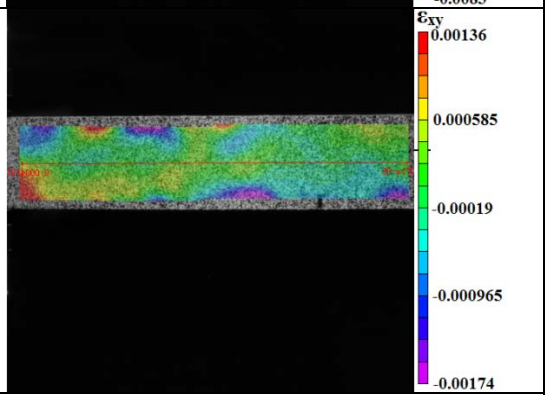

Figure A.3: Strain fields ε_{xx}, ε_{yy}, ε_{xy} for 45/45 specimens when end displacement Δ is 9.96 mm and corresponding deflection w of specimen center is 19.24 mm

	Compression Side	Tension Side
ε_{xx}	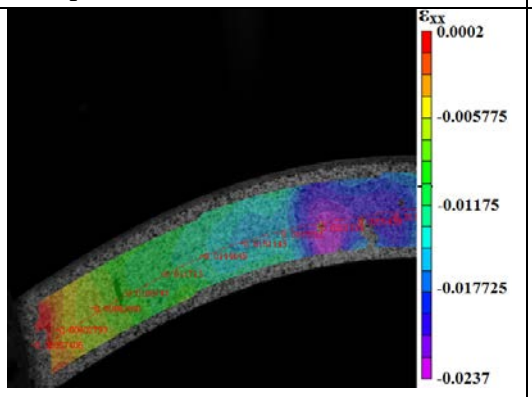	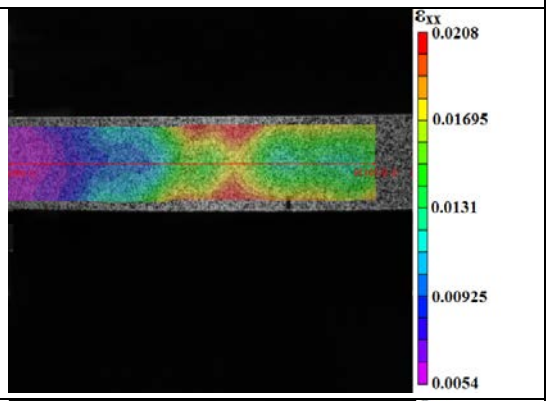
ε_{yy}	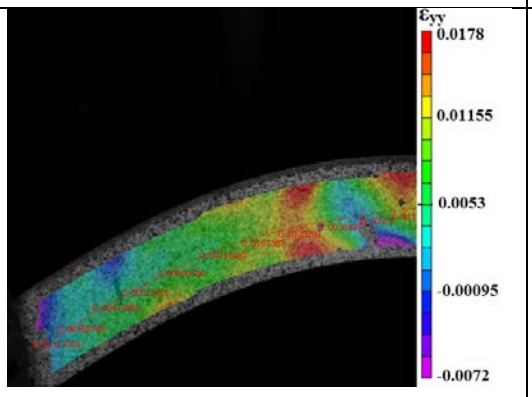	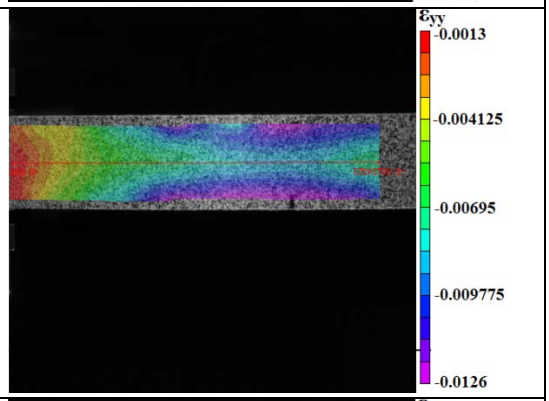
ε_{xy}	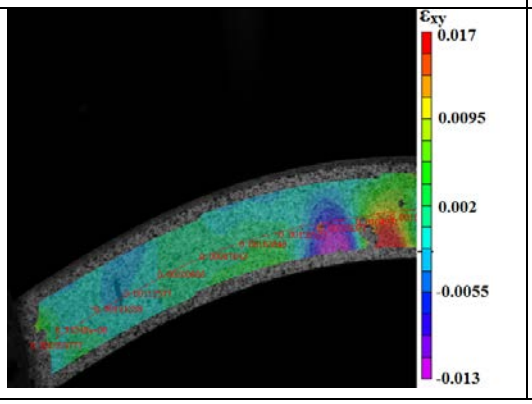	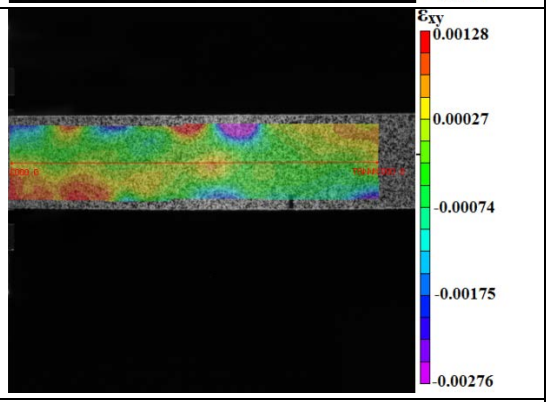

Figure A.4: Strain fields ε_{xx}, ε_{yy}, ε_{xy} for 45/45 specimen, when end displacement Δ is 20.17 mm and corresponding deflection w of specimen center is 26.67 mm

APPENDIX B

Derivation of Small Deformation and Large Deformation Equations for Combined Bending-Compression Loading of Thin Beams

B-1: Small Deformation Analysis

Assuming small deformations, including both displacement and strain, the relationship between the beam's deflection and the applied moment can be written:

$$EI\, w''(x) = M(x) \tag{B-1}$$

According to the experiment setup, the total moment M(x) can be divided into two parts. One is the moment cause by load placed with an offset distance e. The other is the moment caused by the bending deflection.

$$M(x) = M_0 + Pw(x) = P\{e + w(x)\} \tag{B-2}$$

Then we can have the new equation,

$$EIw''(x) + Pw(x) = -M_o \tag{B-3}$$

which is a second order nonhomogeneous ordinary differential equation. The particular solution and general solution of w(x) can be expressed as:

$$w_p(x) = -\frac{M_0}{P} \tag{B-4}$$

$$w_g(x) = A\cos\lambda x + B\sin\lambda x \tag{B-5}$$

where

$$\lambda = \sqrt{\frac{P}{EI}} \tag{B-6}$$

The total deflection w(x) is

$$w(x) = -\frac{M_0}{P} + A\cos\lambda x + B\sin\lambda x \tag{B-7}$$

At position x=0 and x=L, the w(x) equals to zero. Then we can solve the equation above to get coefficient A and B:

$$A = \frac{M_0}{P}, B = \frac{M_0}{P}\left(\frac{1-\cos\lambda L}{\sin\lambda L}\right) \tag{B-8}$$

So the final expression of w(x) is

$$w(x) = e\times(-1+\cos\lambda x + \frac{1-\cos\lambda L}{\sin\lambda L}\sin\lambda x) \tag{B-9}$$

B-2: Large Deformation Analysis

Taking the derivative of θ(s) defined in Fig. 5, we can get

$$\frac{d^2\theta}{ds^2} = -\frac{P}{EI}\times\frac{dw}{ds} = -\frac{P}{EI}\times\sin\theta \tag{B-10}$$

where

$$\frac{1}{2}(\frac{d\theta}{ds})^2 = \frac{P}{EI}\times\cos\theta + C \tag{B-11}$$

The constant C can be evaluated by the boundary condition at the loaded end s=0.

$$w(0)=0, \theta(0)=\theta_0, \left.\frac{d\theta}{ds}\right|_{s=0} = -\frac{P}{EI}\times\cos\theta - \frac{M_0}{EI} = -\frac{Pe}{EI} \tag{B-12}$$

So that

$$C = \frac{1}{2}(\frac{Pe}{EI})^2 - \frac{P}{EI}\times\cos\theta_0 \tag{B-13}$$

$$\frac{1}{2}\left(\frac{d\theta}{ds}\right)^2 = \frac{P}{EI}\times\cos\theta + \frac{1}{2}(\frac{Pe}{EI})^2 - \frac{P}{EI}\times\cos\theta_0 \tag{B-14}$$

In this paper, the e^2 term is infinitesimal when the end displacement is over 0.1 mm, 0.2% of total distance, and hence is neglected throughout the analysis process. According to the establishment of the coordinate system, $d\theta/ds$ should be negative value from $s = 0$ to $s = L$. Thus

$$\frac{d\theta}{ds} = -\sqrt{\frac{2P}{EI}} \times \sqrt{\cos\theta - \cos\theta_0} \tag{B-15}$$

The value of θ_0 cannot be found directly from this equation. However, if we assume that the neutral surface of beam is inextensible, then

$$\sqrt{\frac{2P}{EI}} \int_0^L ds = -\int \frac{1}{\sqrt{\cos\theta - \cos\theta_0}} d\theta = \sqrt{\frac{2PL^2}{EI}} \tag{B-16}$$

The equation could be transformed using an elliptical integral to give;

$$1 - \cos\theta = 2k^2 \sin^2\beta = \left(1 - \cos\theta_0\right) \times \sin^2\beta \tag{B-17}$$

then

$$\frac{1}{\sqrt{\cos\theta - \cos\theta_0}} = \frac{1}{\sqrt{\left(1 - 2k^2\sin^2\beta\right) - \left(1 - 2k^2\right)}} = \frac{1}{\sqrt{2}k\cos\beta} \tag{B-18}$$

and

$$d(\cos\theta) = d\left(1 - 2k^2\sin^2\beta\right) = -4k^2 \sin\beta\cos\beta d\beta \tag{B-19}$$

$$\sin\theta = \sqrt{1 - \cos^2\theta} = \sqrt{-4k^4\sin^4\beta + 4k^2\sin^2\beta} \tag{B-20}$$

then

$$d\theta = -\frac{d(\cos\theta)}{\sin\theta} = \frac{2k\cos\beta d\beta}{\sqrt{1 - k^2\sin^2\beta}} \tag{B-21}$$

And since we have $\frac{1}{\sqrt{\cos\theta - \cos\theta_0}}$ from previous equation,

$$\sqrt{\frac{2P}{EI}}\int_0^l ds = -\int_{\theta_0}^{\theta}\frac{1}{\sqrt{\cos\theta-\cos\theta_0}}d\theta = -\int_{\beta_1}^{\beta_2}\frac{\sqrt{2}}{\sqrt{1-k^2\sin^2\beta}}d\beta \tag{B-22}$$

The lower limit of integral β_1 can be evaluated by the condition at the loaded end s=0.

$$\beta_1 = \sin^{-1}\sqrt{\frac{1-\cos\theta_0}{1-\cos\theta_0}} = \frac{\pi}{2} \tag{B-23}$$

The upper limit of integral β_2 can be evaluated by the condition at the loaded end s=l.

$$\beta_2 = \sin^{-1}\sqrt{\frac{1-\cos\theta}{1-\cos\theta_0}} \tag{B-24}$$

Particularly, at position l=L/2, the w(s) reaches the maximum value, and $\theta=0$, $\beta_2=0$.

$$\sqrt{\frac{2P}{EI}}\int_0^{L/2} ds = -\int_{\frac{\pi}{2}}^{0}\frac{\sqrt{2}}{\sqrt{1-k^2\sin^2\beta}}d\beta \tag{B-25}$$

The right part is a complete elliptic integral of the first kind. In the notation of Jahnke and Emde [59],

$$\sqrt{\frac{P}{EI}}\int_0^{L/2} ds = F(k) \tag{B-26}$$

The load P can be represent in terms of F(k)

$$P = \frac{4\left[F(k)\right]^2 EI}{L^2} \tag{B-27}$$

The next step is to represent the deflection w in terms of θ and an elliptic integral. Since

$$\frac{dw}{d\theta}\frac{d\theta}{ds} = \frac{dw}{ds} = \sin\theta \tag{B-28}$$

And since we have dθ/ds from previous equation

$$\frac{dw}{d\theta}\times\left(-\sqrt{\frac{2P}{EI}}\times\sqrt{\cos\theta-\cos\theta_0}\right)=\sin\theta \tag{B-29}$$

so that

$$w=-\sqrt{\frac{EI}{2P}}\int_{\theta_0}^{\theta}\frac{1}{\sqrt{\cos\theta-\cos\theta_0}}\sin\theta d\theta=\sqrt{\frac{2EI}{P}}\times\sqrt{\cos\theta-\cos\theta_0} \tag{B-30}$$

Particularly, at position l=L/2, the w reaches the maximum value, and θ=0

$$w_{max}=\sqrt{\frac{2EI}{P}}\times\sqrt{1-\cos\theta_0}=\frac{L}{\sqrt{2}\times F(k)}\times\sqrt{1-\cos\theta_0} \tag{B-31}$$

B-3. Beam Shape for Large Deformation

The shape of the beam can be defined by knowing how the axial displacement, Δ, is related to the spatial position of points on the beam, including their arc length location and their lateral displacement, w. Since we have an expression for dw in Eq (B-30), it can be rewritten here as follows;

$$d\omega=-\sqrt{\frac{EI}{2P}}\frac{1}{\sqrt{\cos\theta-\cos\theta_0}}\sin\theta d\theta \tag{B-32}$$

with

$$\frac{dx}{ds}=\cos\theta \qquad \frac{d\omega}{ds}=\sin\theta \tag{B-33}$$

Then, dx and ds can be rewritten in terms of θ

$$ds=-\sqrt{\frac{EI}{2P}}\frac{1}{\sqrt{\cos\theta-\cos\theta_0}}d\theta \tag{B-34}$$

$$dx=-\sqrt{\frac{EI}{2P}}\frac{1}{\sqrt{\cos\theta-\cos\theta_0}}\cos\theta d\theta \tag{B-35}$$

The axial displacement Δ expression can be written as follows;

$$\frac{L-\Delta}{2}=\int dx=-\sqrt{\frac{EI}{2P}}\int_{\theta_0}^{0}\frac{1}{\sqrt{\cos\theta-\cos\theta_0}}\cos\theta d\theta$$
$$=-\sqrt{\frac{EI}{2P}}\int_{\theta_0}^{0}\frac{\cos\theta_0}{\sqrt{\cos\theta-\cos\theta_0}}d\theta-\sqrt{\frac{EI}{2P}}\int_{\theta_0}^{0}\sqrt{\cos\theta-\cos\theta_0}d\theta \qquad \text{(B-36)}$$
$$=\frac{L}{2}\cos\theta_0-\left\{\sqrt{\frac{EI}{2P}}\left(1+\cos\theta_0\right)\times F\left(k\right)-2\times\sqrt{\frac{EI}{P}}\times H\left(k\right)\right\}$$

where H(k) is a complete elliptic integral of the second kind and is written as follows;

$$H(k)=\int_0^{\frac{\pi}{2}}\sqrt{1-k^2\sin^2\beta}d\beta \qquad \text{(B-37)}$$

Then

$$\Delta=L-L\times\cos\theta_0-4\times\sqrt{\frac{EI}{P}}\times H\left(k\right)+2\times\sqrt{\frac{EI}{P}}\left(1+\cos\theta_0\right)\times F\left(k\right)$$
$$=L-L\times\cos\theta_0-2L\times\frac{H\left(k\right)}{F(k)}+L\times\left(1+\cos\theta_0\right) \qquad \text{(B-38)}$$

where P is given by Eq (B-27).

APPENDIX C

Strain Estimates and Variability Using 3D-DIC Measurements

Estimates for strain errors are a direct function of errors in the experimental displacement data and the method used to extract the strain estimates. Assuming a local planar fit to the initial specimen surface, in this work a two-dimensional quadratic function with six independent constants is used locally to fit each component of the measured displacement field. Then, least square minimization is performed;

$$E = {}_i\sum_j [u(x_i,y_j) - (a + bx_i + cy_j + dx_iy_j + ex_i^2 + f\, y_i^2)\,]^2$$

Typically, the summation is over NxN points where experimental data was obtained, where N is an odd number. Once the optimal parameters are obtained, the function is differentiated at the central point in the array to define the local strain using a standard strain metric.

Since we have estimates for the variability in the measured displacement, and the optimization process results in a linear function for the coefficients, then it is straight-forward to determine the variability in the coefficients of the function, variability in the derivatives of the function and hence variability in the strain. Results in our case indicate that the maximum variability in strain (near edges of image) is on the order of +/-500 microstrain.

Confirmation of the theoretical predictions described in the previous paragraph is given in Figure C.1. To obtain this data, a total of 10 image pairs were acquired of the unloaded specimen after completing the 3D system calibration process; a typical contour plot for the axial strain field is shown on the left side of Figure C.1. By analyzing the data for all ten sets of images using Vic-3D software, results indicate that the maximum and minimum strains are +/-500 microstrain, with a standard deviation in each strain component that is less than 150 microstrain.

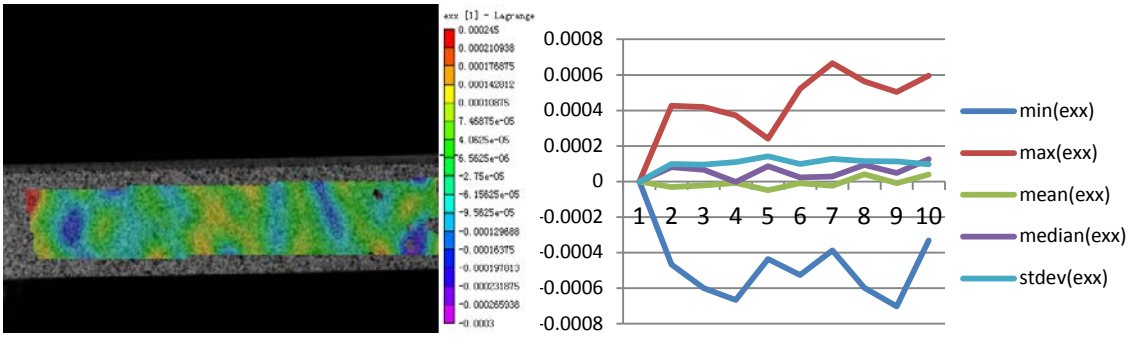

Figure C.1: Measured axial strain field with strain variability metrics across entire field of view